NOTE TO USERS

This reproduction is the best copy available.

UMI®

Synthesis of Electrostatically Actuated Optical Micromirrors

Avinash Kuppar Bhaskar

A Thesis
in
The Department
of
Mechanical and Industrial Engineering

Presented in Partial Fulfillment of the Requirements for the
Degree of Master of Applied Science
at
Concordia University
Montreal, Quebec, Canada, H3G1M8

October 2004

Library and Archives Canada

Published Heritage Branch

395 Wellington Street
Ottawa ON K1A 0N4
Canada

Bibliothèque et Archives Canada

Direction du Patrimoine de l'édition

395, rue Wellington
Ottawa ON K1A 0N4
Canada

Your file Votre référence
ISBN: 0-494-04414-4
Our file Notre référence
ISBN: 0-494-04414-4

NOTICE:
The author has granted a non-exclusive license allowing Library and Archives Canada to reproduce, publish, archive, preserve, conserve, communicate to the public by telecommunication or on the Internet, loan, distribute and sell theses worldwide, for commercial or non-commercial purposes, in microform, paper, electronic and/or any other formats.

The author retains copyright ownership and moral rights in this thesis. Neither the thesis nor substantial extracts from it may be printed or otherwise reproduced without the author's permission.

AVIS:
L'auteur a accordé une licence non exclusive permettant à la Bibliothèque et Archives Canada de reproduire, publier, archiver, sauvegarder, conserver, transmettre au public par télécommunication ou par l'Internet, prêter, distribuer et vendre des thèses partout dans le monde, à des fins commerciales ou autres, sur support microforme, papier, électronique et/ou autres formats.

L'auteur conserve la propriété du droit d'auteur et des droits moraux qui protège cette thèse. Ni la thèse ni des extraits substantiels de celle-ci ne doivent être imprimés ou autrement reproduits sans son autorisation.

In compliance with the Canadian Privacy Act some supporting forms may have been removed from this thesis.

While these forms may be included in the document page count, their removal does not represent any loss of content from the thesis.

Conformément à la loi canadienne sur la protection de la vie privée, quelques formulaires secondaires ont été enlevés de cette thèse.

Bien que ces formulaires aient inclus dans la pagination, il n'y aura aucun contenu manquant.

Abstract

Synthesis of Electrostatically Actuated Optical Micromirrors

Avinash Kuppar Bhaskar

Micro Electro Mechanical Systems (MEMS) or Micro System Technology (MST) has gained a lot of focus in recent years from technologists, as it has evolved as a promising technology having applications in diverse fields such as telecommunications and medicine. Synthesis of one of the micro devices namely, the torsional micromirror that falls under the sub-category of Micro Opto Electro Mechanical Systems (MOEMS) is studied in this thesis. Synthesis involves the comprehensive design, fabrication of micromirrors validated with testing in the present work. The synthesis is carried out in the presence of electrostatic effects on micromirrors.

In the present work the effect of main and counter electrostatic fields on 90° and one dimensional scanning micromirrors are analyzed. In the case of 90° mirror, a stopper is introduced whose electrostatic field improves the tilting angle by increasing the net electrostatic force acting on the micromirror.

The limitations of the surface micromachining MUMPS process over the bulk micromachining using Silicon On Insulator process is amply exhibited for the one dimensional scanning micromirrors. A parametric study is carried out on one dimensional scanning micromirrors with the above mentioned fabrication procedures and

the resulting static angles, pull-in voltage and natural frequency are also presented in this work.

The micromirrors are affected by variations in structural geometry, process parameters and operational environment. It has been earlier proposed that boundary conditioning of microdevices presents a quantifiable approach for the synthesis of the above mentioned variations. In this thesis, boundary conditioning of micromirrors using artificial springs has been extended to external electrostatic field influence and is solved for static deflection and eigenvalues using boundary characteristic orthogonal polynomials in the Rayleigh-Ritz method.

Microfabrication is pivotal in any microsystem synthesis. In the present work, three different microfabrication procedures have been explored to fabricate different types of micromirrors. The first two types of microfabrication procedures, the Multi User MEMS process (MUMPS) and MicraGEM Silicon On Insulator (SOI) process are industry defined microfabrication processes. In the third process, the SOI wafers are patterned and bulk micromachining process is carried out with Xenon difluoride (XeF_2) dry etchant using the facility at CONCAVE.

The testing of dynamic behavior of MEMS devices is carried out to validate the synthesis approach used in this thesis. The released micromirrors are tested for dynamic behavior and tilting angle.

Dedicated to Kuppar,

the Genesis of Aspirations

Acknowledgements

The author is deeply privileged to work under thesis supervisors Dr. R. B. Bhat and Dr. Muthukumaran Packirisamy. It was Dr. R. B. Bhat's invaluable advice to look at the atomic level which helped the author to mould his thoughts on a technical plane. The author is deeply indebted to him for providing an opportunity to work under him.

The author would also like to express his sincere gratitude to the co- supervisor Dr. Muthukumaran Packirisamy. Dr. Packirisamy's vision and ideas on MEMS provided the pillars for this thesis to be built on. The author would like to express his sincere thanks to Dr. Muthukumaran Packirisamy for instilling passion in his work.

The author would like to express his thanks to Dr. Ion Stiharu for valuable guidance during various stages of this thesis.

It is the author's pleasure to acknowledge the help offered by Mr. John Elliott, Technical Officer (retired) and Mr. Danius Juras, Technical Officer, Concave during the experimental stages of this work.

The author wishes to express his thanks to Mr. Eric Duchesne, of Ecole Polytechnic for valuable assistance during the taking of Scanning Electron Microscope (SEM) pictures.

The author would like to thank Canadian Microelectronic Corporation (CMC) for providing the microfabrication facilities and Canadian Space Agency (CSA) for providing monitory assistance during the course of this work.

It is the author's pleasure to work with colleagues Mr. Gino Rinaldi, Mr. Arvind Chandrasekaran, Mr. Rakesh Kalyanaraman, who provided valuable help during the various stages of this work.

The author would like to express his gratitude to his uncle Mr. Shankar Udupa and the author's parents without whose help the dream would have been only a dream. Also last but not the least, the author would like to thank Ranjani Udupa, Shivaprasad Udupa, Veena Udupa and his cousins Ranganath Udupa, Gurudath Subbanna and Sharmila Udupa for being there always.

TABLE OF CONTENTS

i. List of Figures ix

ii. List of Tables xv

iii. Nomenclature xvi

Chapter 1 Introduction 1

1.1 Evolution of MEMS 1

1.1.1 Micro Electro Mechanical Systems (MEMS) 1

1.1.2 Growth of MEMS 2

1.1.3 Micro Opto Electro Mechanical Systems (MOEMS) 2

1.1.3.1 Introduction to micromirrors 3

1.2 Actuation of MOEMS devices 8

1.3 Silicon for fabrication of MEMS devices 10

1.4 Methods of MEMS fabrication 13

1.4.1 Etching methods 14

1.4.2 Bulk micromachining 16

1.4.3 Surface micromachining 17

1.5 Manufacturing of MEMS devices 18

1.6 Vibration characteristics and boundary conditioning of MEMS devices 20

1.7 Testing of MEMS devices 22

1.8 Objectives and scope of the present research work 23

1.8.1 Objectives 23

1.8.2 The scope of thesis 24

Chapter 2 Effects of electrostatic field on the dynamics of torsional micromirrors 25

2.1 Introduction to electrostatic actuation 25

2.2 Modeling of switching response of 90° torsional micromirrors 29

2.2.1 Results and discussion 35

2.3 Conceptual design of one dimensional scanning micromirror based on MUMPS and SOI bulk micro machining procedures 43

2.3.1 Design based on MUMPS microfabrication technique 45

2.3.2 Design using SOI based bulk micromachining process 47

2.3.3 Results and discussion 48

2.3.3.1 Results obtained for MUMPS designs 48

2.3.3.2 Results obtained for SOI bulk micromachining process 49

2.4 Conclusions 56

Chapter 3 Boundary conditioning of electrostatically operated devices 58

3.1 Introduction 58

3.1.1 Introduction to boundary conditioning 59

3.1.2 Boundary characteristic orthogonal polynomials 60

3.2 Modeling of micromirrors using artificial springs 62

3.2.1 Static behavior 65

3.2.2 Dynamic behavior 71

3.2.3 Results and discussion 73

Chapter 4 Micromachining methods 87

4.1 Introduction 87

4.2 Multi User MEMS Process (MUMPS) 88

4.2.1 Process overview 88

4.2.2 Design layout 90

4.3 MicraGEM SOI micromachining process 94

4.3.1 Process overview 94

4.3.2 Design layout 95

4.4 Feasibility study of bulk micromachining of SOI wafers using XeF_2 dry isotropic etchant 98

4.4.1 Introduction 98

4.4.2 Process flow 100

4.4.2.1 Mask preparation 100

4.4.2.2 Photolithography 102

4.4.2.3 Dry etching using isotropic XeF_2 etchant 105

4.4.2.3.1 Etching method 105

4.4.2.3.2 Microfabrication results and discussion 107

Chapter 5 Testing - 118

5.1 Introduction 118

5.2 Static testing 119

5.2.1 Static angle results and discussion 122

5.3 Dynamic testing 126

5.3.1 Results 127

Chapter 6 Conclusions 130

6.1 Conclusions 130

6.2 Recommendations for future work 133

References 135

LIST OF FIGURES

Fig. 1.1	DMD pixel schematic	5
Fig. 1.2	DMD pixel	5
Fig. 1.3	SEM of DMD array	5
Fig. 1.4	Top view of the 1 x 4 switch scheme	6
Fig. 1.5	SEM image of a SOI tilting mirror for optical cross-connect switches	7
Fig. 1.6	SEM of electrostatic comb-drive actuated micromirror	10
Fig. 1.7	Silicon wafers	11
Fig. 1.8	Wafer flats for a typical silicon wafer	12
Fig. 2.1	SEM picture of the top view of a double sided micromirror	26
Fig. 2.2	Schematic view of the mirror	27
Fig. 2.3	Schematic of the torsional micromirror	30
Fig. 2.4	Schematic representation of electrostatic fields	31
Fig. 2.5	Typical variation of electrostatic torque at different voltages and mechanical torque with respect to the tilting angle	33
Fig. 2.6	Variation of electrostatic torque for Case (A)	39

Fig. 2.7	Variation of electrostatic torque for Case (B)	39
Fig. 2.8	Variation of electrostatic torque for Case (C) for $H_s = 20\mu m$	40
Fig. 2.9	Variation of individual electrostatic torque for V = 150 volts	40
Fig. 2.10	Variation of equilibrium angles	41
Fig. 2.11	Influence of voltages on scan angles for different cases	41
Fig. 2.12	Influence of voltages on natural frequency of the micromirror for different cases	42
Fig. 2.13	Response of the micromirror for the three cases at V = 150 volts	42
Fig. 2.14	Schematic of one dimensional scanning micromirror	44
Fig. 2.15	Side view of the schematic of the micromirror	44
Fig. 2.16(a)	Tilting or scan angles for $L = 100\mu m$ and $W = 100\mu m$ of mirror dimensions (Case 1) of MUMPS for different bias voltages	51
Fig. 2.16 (b)	Variation of frequency with bias voltage for different hinge lengths for Case 1 of MUMPS	51
Fig. 2.16 (c)	Equilibrium angles determining the pull-in voltage for different hinge lengths for Case 1 of MUMPS	52
Fig. 2.17(a)	Tilting or scan angles for $L = 200\mu m$ and $W = 200\mu m$ of mirror dimensions (Case 2) of MUMPS for different bias voltages	52

Fig. 2.17 (b) Variation of frequency with bias voltage for different hinge lengths for Case 2 of MUMPS 53

Fig. 2.17 (c) Equilibrium angles determining the pull-in voltage for different hinge lengths for Case 2 of MUMPS 53

Fig. 2.18 (a) Tilting or scan angles for L = 500μm and W = 500μm of mirror dimensions (Case 1) of SOI based bulk micromachining for different bias voltages 54

Fig. 2.18 (b) Tilting or scan angles for Case 1 of SOI based bulk Micromachining process for different bias voltages 54

Fig. 2.19 (a) Tilting or scan angles for L = 1000μm and W = 1000μm of mirror dimensions (Case 2) of SOI based bulk micromachining for different bias voltages 55

Fig. 2.19 (b) Tilting or scan angles for Case 2 of SOI based bulk Micromachining process for different bias voltages 55

Fig. 2.19 (c) Equilibrium angles determining the pull-in voltage for different hinge lengths for Case 2 of SOI based bulk micromachining 56

Fig. 3.1 Structural scheme of boundary conditioning 62

Fig. 3.2 Lumped model of an elastic system with boundary conditioning 63

Fig. 3.3 Electrostatic field modeled as springs 64

Fig. 3.4 Static deflection in μm of mirror as a square plate for CCCC condition at V = 100 volts 69

Fig. 3.4a Static deflection in μm of micromirror at y = 0.5 for CCCC

at different voltages 69

Fig. 3.5 Static deflection in μm of mirror as a square plate for MMMM condition at V = 100 volts 69

Fig. 3.5a Static deflection in μm of micromirror at y = 0.5 for MMMM at different voltages 69

Fig. 3.6 Static deflection in μm of mirror as a square plate for SSSS condition at V = 100 volts 70

Fig. 3.6a Static deflection in μm of micromirror at y = 0.5 for SSSS at different voltages 70

Fig. 3.7 A plot of voltage and frequency parameter for the three end conditions 74

Fig. 3.8 First modeshape for CCCC condition of micromirror 78

Fig. 3.8a Plot of 1st mode for CCCC condition at y = 0.5 78

Fig. 3.9 Second modeshape for CCCC condition of micromirror 79

Fig. 3.9a Plot of 2nd mode for CCCC condition at y = 0.5 79

Fig. 3.10 Third modeshape for CCCC condition of micromirror 79

Fig. 3.10a Plot of 3rd mode for CCCC condition at y = 0.5 79

Fig. 3.11 First modeshape for MMMM condition of micromirror 80

Fig. 3.11a Plot of 1st mode for MMMM condition at y = 0.5 80

Fig. 3.12 Second modeshape for MMMM condition of micromirror 81

Fig. 3.12a Plot of 2nd mode for MMMM condition at y = 0.5 81

Fig. 3.13 Third modeshape for MMMM condition of micromirror 81

Fig. 3.13a	Plot of 3rd mode for MMMM condition at y = 0.5	81
Fig. 3.14	First modeshape for SSSS condition of micromirror	82
Fig. 3.14a	Plot of 1st mode for SSSS condition at y = 0.5	82
Fig. 3.15	Second modeshape for SSSS condition of micromirror	83
Fig. 3.15a	Plot of 2nd mode for SSSS condition at y = 0.5	83
Fig. 3.16	Third modeshape for SSSS condition of micromirror	83
Fig. 3.16a	Plot of 3rd mode for SSSS condition at y = 0.5	83
Fig. 3.17	Modal deviation parameter of the first modes for the three end support conditions	84
Fig. 4.1	Scheme indicating the sequence material and grouping of layers in MUMPS	88
Fig. 4.2	Layout of design using L-Edit	91
Fig. 4.3	3D view of a micromirror present in Figure 4.2	91
Fig. 4.4	SEM pictures of MUMPS fabricated device	93
Fig. 4.5	Steps involved in MicraGEM SOI process	94
Fig. 4.6	Design Layout	95
Fig. 4.7	SEM pictures of the devices fabricated through MicraGEM SOI process	97
Fig. 4.8	Sample masks of micromirrors	102
Fig. 4.9	Photolithography setup showing the mask aligner and the spin processor	104
Fig. 4.10	SEM picture of the patterned micromirror on the SOI wafer	104

Fig. 4.11	Schematic of the XeF_2 setup	107
Fig. 4.12	Photograph of the XeF_2 pulse etching setup in fume hood during operation	108
Fig. 4.13	Process flow adopted for XeF_2 bulk micromachining	109
Fig. 4.14(a)	A particular pulse showing the maximum initial pressure of XeF_2 in the chamber as 2 torr	111
Fig. 4.14(b)	A particular pulse showing the maximum initial pressure of XeF_2 in the chamber as 1.6 torr	111
Fig. 4.14(a)	A particular pulse showing the maximum initial pressure of XeF_2 in the chamber as 2 torr	112
Fig. 4.15	Optical Microscope pictures of an etched specimen for etchrate measurement	112
Fig. 4.16	SEM pictures of micromirrors on the device side of the SOI wafer	113
Fig. 4.17	SEM pictures of etched handle side or backside of SOI wafer	114
Fig. 5.1	Testing setup to measure static angle	120
Fig. 5.2	Microscopic view of laser spot on a micromirror	121
Fig. 5.3	SEM view close-up of micromirror and the torsion beam	123
Fig. 5.4	Comparison of experimental and theoretical static angles for different voltages	124
Fig. 5.5	SEM pictures of snapped micromirror fabricated through MicraGEM SOI process	125

Fig. 5.6 Schematic of LDV setup for dynamic testing 127
Fig. 5.7 Theoretical variation of natural frequency at different bias voltage 128
Fig. 5.8 Theoretical variation of natural frequency at different bias voltage 129

LIST OF TABLES

Table 2.1	Design parameters of torsional micromirrors	33
Table 2.2	Thickness of layers used in MUMPS	46
Table 2.3	Mirror design parameters for MUMPS	46
Table 2.4	Mirror design parameters for SOI based bulk micromachining	47
Table 3.1	Voltages for different ‘σ’ values	76
Table 3.2	‘λ’ values for first four modes obtained for different bias voltages	77
Table 5.1	Tabulation of static or scan angles	124
Table 5.2	Tabulation of natural frequencies	127

NOMENCLATURE

CMC	Canadian Microelectronics Corporation
CCCC	Clamped on all edges
DMDTM	Digital Micromirror Device
DLPTM	Digital Light Processor
DRIE	Deep Reactive Ion Etching
DWDM	Dense Wavelength Division Multiplexing
LIGA	German for Lithography, Galvanoformung, Abformung which stands for lithography, electroplating, and molding
MEMS	Micro Electro Mechanical Systems
MOEMS	Micro Opto Electro Mechanical Systems
MMMM	Microfabricated support condition
MST	Micro Systems Technology
RIE	Reactive Ion Etching
SOI	Silicon On Insulator
SEM	Scanning Electron Microscope
SSSS	Simply supported edge boundary condition
A	Surface area
a	dimension of the plate in x direction
A^{s}_{mn}	Static deflection coefficient
b	dimension of the plate in y direction
C	Damping coefficient
D	flexural rigidity of the plate

d	Spacing between the electrodes
D_{mn}	Dynamic deflection coefficient
E	Electrostatic Field
F	Electrostatic force
G	Modulus of rigidity
H_s	Height of the stopper
h	thickness of the plate
J	Polar mass moment of inertia
K_e	Stiffness reduction due to the electrostatic field
K_m	Mechanical stiffness
K_{eq}	Equivalent stiffness
$K^*_{R,i}$	normalized rotational stiffness $= \frac{K_{R,i} a}{D}$
$K^*_{T,i}$	normalized translational stiffness $= \frac{K_{T,i} a^3}{D}$
L	Length of the micromirror
l_b	Length of the beam
l_s	length of the sth side
t	Thickness of the micromirror
T_e	Net torque due to the electrostatic force on the micromirror
T_m	Torque due to the mechanical resisting force of the torsion beams
T_{max}	Kinetic energy of the mirror as a rectangular plate
T_{eC}	Electrostatic torque due to the counter electric field

T_{eM}	Electrostatic torque due to the main electric field
T_{eS}	Electrostatic field due to the stopper electrode
U_e	Electrostatic strain energy
$U_{max,p}$	strain energy of the plate due to bending
$U_{R,s}$	potential energy of sth side rotational spring
$U_{T,s}$	potential energy of sth side translational spring
U_{net}	Total strain energy at the static equilibrium
U_{el}	Electrostatic potential energy considering electrostatic stiffness
V	Bias voltage between the micromirror and the substrate
W	Width of the micromirror
w	Width of the beam
W_d	Transverse deflection
W_s	Static deflection
x	normalized coordinate $=\frac{\xi}{a}$
y	normalized coordinate $=\frac{\eta}{b}$
β	Modal deviation parameter
ε	Dielectric constant of vacuum
ε_r	Relative permittivity
η	coordinate the plate
λ	Eigenvalue $=\frac{\rho\ h\ a^4\omega^2}{D}$

θ	Tilting angle
ρ	mass density of the plate
σ	Normalized voltage parameter
ω	Natural frequency
ξ	coordinates the plate
$\phi_m(x)$	Boundary characteristic orthogonal polynomial in x direction
$\varphi_n(y)$	Boundary characteristic orthogonal polynomial in y direction
$(\ )'$	differentiation with respect to x
$(\dot{})$	differentiation with respect to y

Chapter – 1
Introduction

1.1 Evolution of micro systems

1.1.1 Micro Electro Mechanical Systems (MEMS)

Micro Electro Mechanical Systems (MEMS) are mechanical devices having moving components of size in the order of micrometers with a possibility of integrating electronic circuitry for signal conditioning and analysis in the same chip. In recent times, because of the rapid growth, MEMS are considered as systems having microfabricated elements. Using Micro Electro Mechanical Systems (MEMS) it is possible to accomplish miniaturization of conventional sensors and actuators to micro level. The field of MEMS as it is known in North America, is also known as Micro System Technology (MST) in Europe and as Micromachines in Japan [1]. This technology has found applications in areas as diverse as telecommunication and medicine [2, 3].

The applications of this technology can be found in devices such as laser heads in CD and DVD units for entertainment, as read-write heads in magnetic hard disks, as optical switches for communications. Also in the field of health where the technology is referred to as BioMEMS they are used as heart pacemakers and hearing aids. In the field of automobile, a modern car uses more than thirty MEMS devices to cover ergonomics, safety and performance [4, 5]. Pharmaceutical and biotechnology industries use microtechnology by using miniaturized devices for high throughput screening [6].

1.1.2 Growth of MEMS

MEMS technology can be adapted to a variety of new products in diverse fields. It is estimated that by 2006 the revenue through MEMS technology would climb to in excess of US $ 34 billion. The unit consumption of MEMS/MST devices is expected to rise from the present 3.5 billion to over 10 billion in this period [7].

The major challenge currently in MEMS industries arising due to rapid development is commercialization which includes manufacturing obstacles like packaging and process control; there are also challenges in research and development which include process expertise and material control.

1.1.3 Micro Opto Electro Mechanical Systems (MOEMS)

The vast area of MEMS has been divided into many sub-branches and the devices are classified accordingly. One of the important and developed branches is the Micro Opto Electro Mechanical Systems (MOEMS). This technology allows electrical, mechanical and optical functions to be combined in a stable assembly [8].

Fujita [9] has outlined the impact of MEMS technology to optics. He asserted that the features of MEMS such as arrayed micro structures and integration of multiple function devices can be used in optics for 2D arrays of moving parts, optical systems on a chip and fast control of large scale array device. Examples for this include near field

optical devices and devices for optical fiber networks. The ability in MEMS such as, miniaturizing the moving parts can be used to obtain a machining precision in the order of 10nm which will help in the fabrication of MOEMS devices such as silicon optical bench. As the MOEMS devices can perform the basic optical functions (refraction, diffraction, reflection, deflection and dispersion) [10] they find applications such as in micromirrors used as optical switches for optical fiber networking. These micromirrors are usually operated in two dimensional arrays and they have a highly reflective surface. Other than optical switching they find applications in barcode readers [11], laser printers and display [12, 13]. For these applications, a pop-up mirror driven by a comb actuator has been proposed [11], in which the mirror plate is attached to the substrate through micro hinges [14] so as to produce a large scanning angle.

1.1.3.1 Introduction to Micromirrors

The present thesis deals with micromirrors discussed earlier. These micromirrors are used in electronic projection displays and telecommunication industry as optical switches for Dense Wavelength Division Multiplexing (DWDM). The mirrors are usually arranged in arrays and can be repositioned rapidly to reflect or not to reflect light. One of the earliest micromirrors was the DMD™ or the Digital Micromirror Device developed by Texas Instruments which is now used in their Digital Light Processing (DLP™) for electronic projection displays [Digital Micromirror Device, DMD and DLP are trademarks of Texas Instruments Incorporated, Dallas, Texas, USA].

As the cathode ray tube (CRT) technology used for electronic projection evolved over the years, the goals narrowed down to producing brighter, higher fidelity images with displays having lower weight and cost. This led to the improvement of CRT's, introduction of scanned laser beams, the liquid crystal display (LCD) and the latest being DLP™ based on DMD™ [15]. In 1977, Hornbeck [16] of Texas Instruments built a CCD-addressed membrane based spatial light modulator for optical processing applications which was called the Deformable Mirror Device. This device was analog based and required a high-voltage addressing. In 1979, a chip containing 256 mirrors was demonstrated laying the foundation for arrays of mirrors. By 1980, this had progressed to a chip of 128 x 128 arrays of micromirrors [15]. However it was later realized that the analog aspect was less efficient and would not be suitable for the commercial market. Hence in 1987, Hornbeck's [16] attempt to replace analog approach with digital approach was materialized with the birth of DMD™. A typical DLP™ is made up of arrays of DMD™ with number of mirrors varying depending on desired resolution.

DMD™ consists of a 2 dimensional array of optical switching elements or pixels on silicon substrate. Figure 1.1 shows a break up of a single pixel of the device. A central post supports reflective micromirrors as shown in the figure.

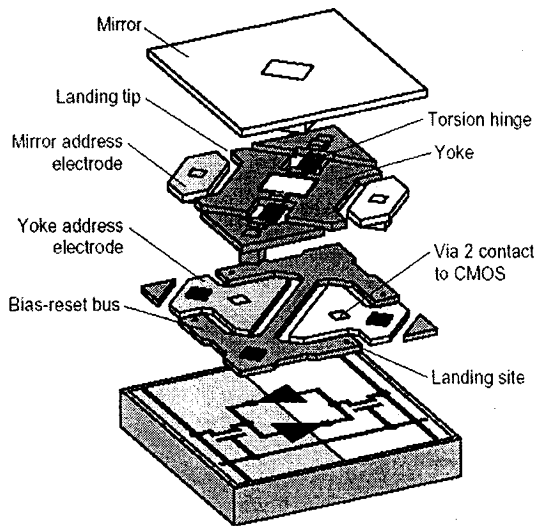

Fig. 1.1 DMD pixel schematic [17]

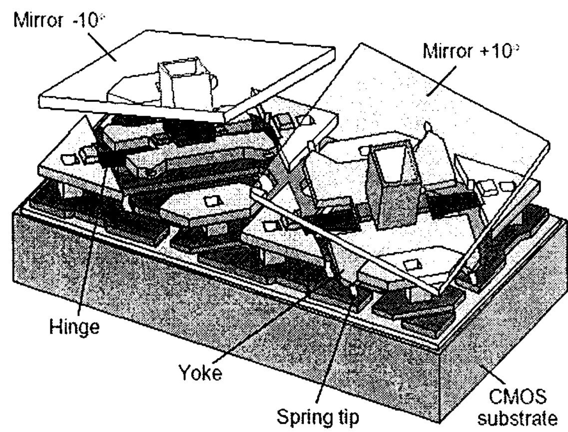

Fig. 1.2 DMD pixel (mirror rotated) [17]

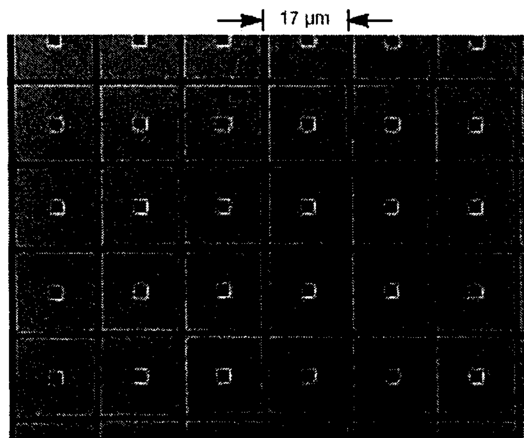

Fig. 1.3 SEM of DMD array [16]

The central post is mounted on a metal platform or the yoke which is supported by torsional hinges. The electrodes are provided underneath the yoke which provide electrostatic actuation using a 24 volts bias voltage. A circuit was developed to rotate the

mirrors +/-10° in a classical on/off binary action of the digital system. Figure 1.2 shows the assembled DMD™ and Figure 1.3 shows the SEM picture of the DMD™ array [16].

In order to demonstrate the use of a micromirror in an optical switch, Wang et al. [18] developed a 1 x 4 optical switch using deep reactive ion etching technology (DRIE). The scheme (Figure 1.4) of the fabricated device technology shows three vertical silicon (M_1-M_3) mirrors and five tapered/lensed fibers (F_1-F_5). When a working voltage is applied to any one of the comb actuators, the associated mirror M_1, M_2 or M_3 will be driven linearly into the optical path due to the electrostatic force, and consequently the input light will be reflected by the mirror to fiber F_4, F_2 or F_5, respectively. When no voltage is applied to the comb structure, the light is reflected to the fiber F_3 because of the mirror being pulled back by an attached spring. When the mirror M_3 is tilted with an

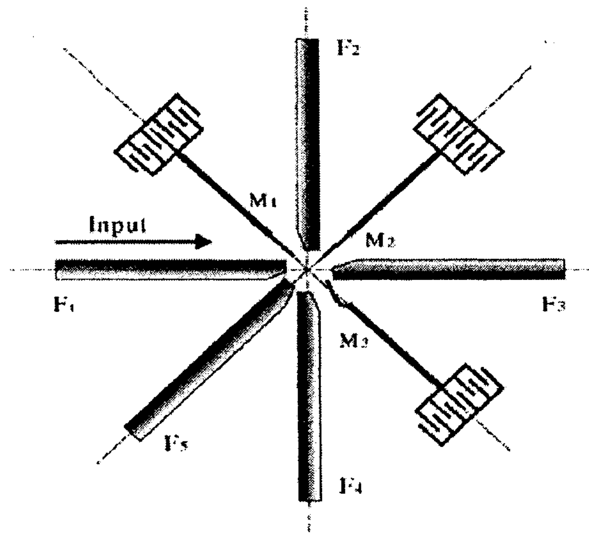

Fig. 1.4 Top view of the 1 x 4 switch scheme [18]

angle of 22.5^{o} the light is reflected to fiber F_5 shown in Figure 1.4. Many researchers have come up with various other types of micromirrors for various applications. Rosenberg et al. [19] have described the development of active mirrors employing both surface and bulk micromachined techniques for use as Fabry-Perot interferometers in a three-axis fiber optic strain sensor. Kiang et al. [12] have developed scanning micromirrors driven by electrostatic comb actuators which have resonant frequencies in kHz range and used for optical scanning applications such as in bar code reading, optical data storage, and laser surgery.

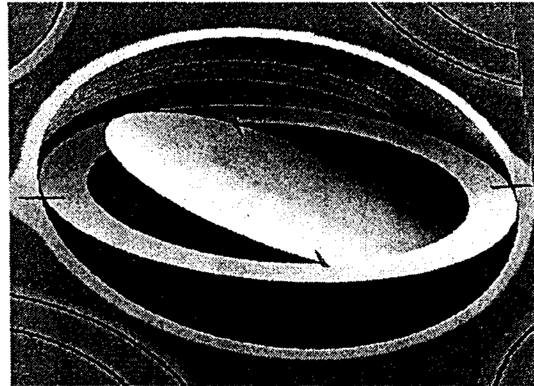

Fig. 1.5 SEM image of a SOI tilting mirror for optical cross connect switches [20]

Schenk et al. [21] describe a resonantly excited 2D micro scanning mirror developed on a Silicon On Insulator (SOI) wafer. Figure 1.5 shows one such type of SOI micromirror. The actuation is through electrostatic principle. Liew et al. [22] present MEMS mirror fabricated using a standard Complimentary Metal Oxide Semiconductor process [CMOS] actuated using a thermal multi-morph actuator which is based on the bi-morph beam theory.

Graffe et al. [23] developed an electrostatically actuated 2 axial mirror which is used for fine-pointing or fine-steering mechanisms to point and stabilize a laser beam to a specific direction and to compensate for mechanical vibrations and movement of the satellite for inter-satellite laser communication systems.

1.2 Actuation of MOEMS devices

Successful operation of MOEMS devices such as micromirrors depends on efficient actuation. There are many types of actuation principles which are being currently used. Yi et al. [24] used magnetic actuation for rotating hinged flaps. A piece of electroplated Permalloy material is attached to a hinged flap to provide the means of actuation. On application of external magnetic field the Permalloy develops magnetization which interacts with the external field to produce a torque. The induced torque causes the flap to rotate out of plane about its base. Another work by Zou et al. [25] used the same principle to actuate a 3 dimensional microstructure assembly.

Thermal microactuators are also used for actuation purpose as they are compact and can provide high output force [26]. Most of the thermal actuators rely on bi-morphs which are two or more layers of materials with differing co-efficient of linear thermal expansion [27]. When they are heated by an electrical current, they bend like a bimetal and produce motion which is most suitable for positioning stages, mechanical scanning units and other applications. An out of plane displacement for a novel large vertical displacement (LVD) micromirror was provided by a pair of electrothermal actuators [28].

In this, the mirror plate is attached to a rigid silicon frame by a set of aluminum/ silicon dioxide bimorph beams. The heater for the thermal bimorph actuator is provided by a polysilicon resistor which is embedded within the silicon dioxide layer. These beams when heated undergo expansion and help in actuating the micromirror and hence are aptly referred as mirror actuators.

The most easy to use actuation principle is the electrostatic principle. When a bias voltage is applied between two electrodes, one fixed and the other movable, electrostatic force is developed between the electrodes, which will actuate the movable electrode. Many researchers have fabricated devices based on electrostatic principle. Hsieh et al. [29] developed a microelectromechanical torsional actuator (META) which is actuated electrostatically and it consists of suspensions, mirror plates and silicon substrate. The voltage is applied between one of the electrodes and the mirror. The electrostatic force hence developed pulls the mirror to the bottom substrate. Electrostatic combdrives is a popular method of using electrostatic actuation principle. Kiang et al. [12] describe an electrostatic combdrive actuated micromirror used for laser beam scanning and positioning. Figure 1.6 shows the micromirror with the combdrive. They conclude that these are used as actuators for their low-power consumption and high resonant frequencies. The combdrive consists of moving fingers and stationary fingers. The mirror is attached to the moving fingers. The voltage is applied between the moving and the stationary fingers which will cause the actuation of micromirrors.

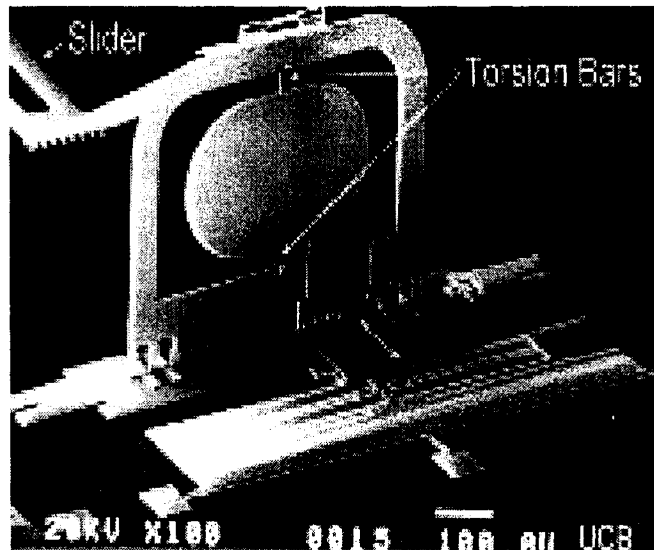

Fig. 1.6 SEM of the electrostatic comb-drive actuated micromirror [13]

Electrostatic actuation has also been used to slide micro liquid metal droplets for bi-stable switching [30].

In the present work the electrostatic actuation has been used to actuate the fabricated devices and the effects of electrostatic fields have been analyzed.

1.3 Silicon for fabrication of MEMS devices

Most of the MEMS devices fabricated today use silicon as the base material as it is well characterized and readily available, and many types of mature processing techniques can be directly applied for silicon. The crystal plane anisotropy of silicon is suitable for different types of micromachining and silicon enables direct integration with active circuits. Even though, silicon is a brittle material, its proof strength (7Gpa) is higher than the yield strength of steel (2GPa) and hence it has more ductile range than steel. Silicon is grown using the Czochralski method of crystal growing. It involves

melting of silicon, pulling the liquid silicon to form an ingot using a seed crystal by combination of liquid surface tension and capillary action. The diameter of the solidifying crystal can be precisely controlled. The solidified ingot is called a boule. This boule is eventually sliced into wafers of desired thickness as shown in Figure 1.7.

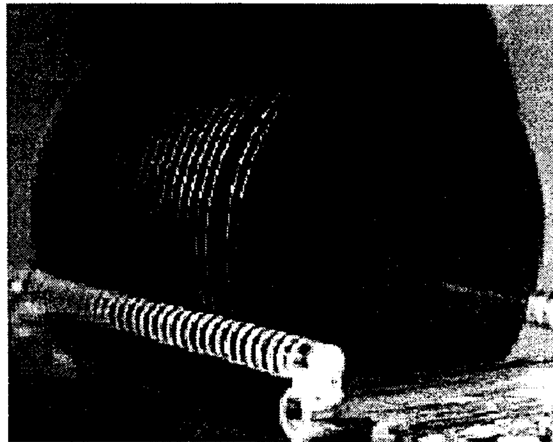

Fig. 1.7 Silicon wafers

The single crystal silicon has diamond cubic structure. The orientation of the wafer is indicated by having a flat which is denoted by Miller indices which are a set of three integers that designate crystallographic plane as determined from reciprocals of fractional axial intercepts [31]. Miller indices are often used to indicate the crystal orientations, crystal planes etc. Figure 1.8 shows the different representation of flats and their Miller indices. (i j k) indicates a specific plane, and notation [i j k] indicates a specific direction. Similarly, {i j k} indicates family of equivalent planes and <i j k> indicates family of equivalent directions. Most of the silicon wafers being used as the substrate are 100mm or in some cases 150mm wafers. The typical 100mm wafers are 500μm thick, but wafers of different thicknesses can be obtained [10].

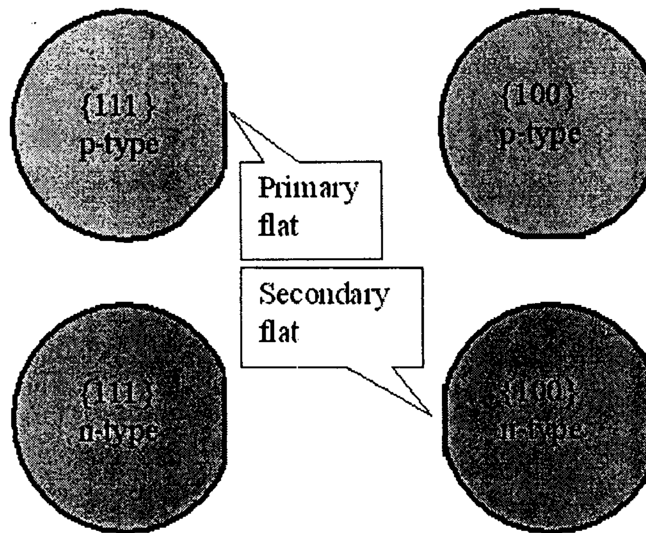

Fig. 1.8 Wafer flats of typical silicon wafers

There are many types of silicon wafers available. In the present thesis the work has been carried out mostly using Silicon On Insulator (SOI) wafers. According to Cellar et al. [32] these are precisely engineered multilayer semiconductors/ dielectric structures that provide new functionality for advanced Si devices. These wafers consist of single crystalline silicon separated by a layer of SiO_2 from the handle or the bulk substrate [33-35]. The top layer of single crystal silicon is called the device layer.

Different fabrication methods have been suggested for the SOI wafers. In one of the processes called SIMOX [33] which stands for separation by implantation of oxygen, buried oxide layer is synthesized *in situ* from implanted oxygen. Two wafers are bonded with an oxide layer in between and one of the wafers is thinned by grinding and etch back method [34]. In another process called the SmartCut™ process, a layer of silicon is oxidized to desired thickness. This is called the Buried Oxide (BOX) process. This is

then transferred to a "handle" wafer using wafer bonding. This layer transfer is facilitated by ion-implantation [35].

There are many advantages of using SOI wafers. Yi et al. [36] states that electrically functional components can be formed in mechanical structures, for example, it can be used as n-p-n junction in order to electrically isolate two mechanically connected beams. The other advantages of using SOI wafers are they are optically very flat [37] and hence are ideal for MOEMS devices such as micromirrors. The residual stress in the SOI wafers is minimal as compared to other wafers, which avoids bending of microfabricated structures. In the present work SOI wafers are used in two of the three fabrication procedures.

1.4 Methods of MEMS fabrication

Micromachining can be broadly divided into two categories: Surface micromachining and bulk micromachining. Surface micromachining is an additive process in which the processing is done above the substrate by way of deposition and selective removal of materials such as dielectrics, metals etc. Bulk micromachining is a subtractive process in which the processing removes "bulk" of the substrate creating large pits, holes, etc. The processing will normally involve etching, laser machining, mechanical milling, etc [10].

1.4.1 Etching methods

Etching is an important process in microfabrication, which involves pattern transfer by chemical/physical removal of a material from a substrate. A protective mask layer such as an oxide or a photoresist is used for patterning using photolithography. Etching can be classified into two types: dry etching and wet etching. In dry etching the solid surface is etched in the gas or vapor phase, physically by ion bombardment, chemically by chemical reaction through a reactive species at the surface or by combined physical and chemical mechanisms. Wet chemical etching or wet bulk micromachining are used to etch out bulk of materials such as silicon, quartz, SiC, GaAs, and Ge by orientation independent (isotropic) or orientation-dependent (anisotropic) wet etchants.

Isotropic etchants etch in all directions at nearly or exactly the same rate. The etch stops for these etchants have to be defined explicitly. Xenon difluoride (XeF_2) is a dry isotropic etchant which etches silicon but is highly selective to materials such as aluminum and photoresist. Another isotropic etchant is HNA, a wet etchant which is a mixture of hydrofluoric acid (HF), nitric acid (HNO_3) and acetic acid (CH_3COOH). Anisotropic etchants etch faster in one direction than in others. For example, the etch rate slows down at <1 1 1> plane of silicon for most of the anisotropic etchants relative to etch rates at other planes. Anisotropic etchants such as potassium hydroxide (KOH) and Tetra Methyl Ammonium Hydroxide (TMAH) etch very slowly on <1 1 1> planes of silicon thereby forming an angle of 54.74° with the <1 0 0> plane.

Whenever an etchant has to be selected for etching, it is important to know the etch rate of the particular etchant. The etch rate is the amount of material removed by the

etchant per minute. The etch rate of most of the etchants that target specific materials is known. Williams [38] has tabulated the etch rates of various etchants. He claims that etch rate of silicon with KOH is listed to be around 14000 Å /min. A combination of Bromine and Fluorine (BrF_3) will be an isotropic etchant which has been used in the fabrication of microlenses [39]. The study concludes that when the etch rate is high, the roughness of the etched surfaces is small. The study further claims that by adding Xenon to this mixture, the roughness can be reduced to a minimum.

Isotropic silicon dry etching process using XeF_2 has been used to release PZT cantilevers (lead zirconate titanate (PZT, $Pb(Zr,Ti)O_3$)) [40]. Wet anisotropic etching of silicon has been successfully used to fabricate 45° mirrors with well defined V-grooves [41]. EDP and KOH have been used in this paper to get well defined grooves. Earlier [42], the excellent properties of anisotropically etched V-grooves were used in optical fiber splicing. Cristea [43] fabricated a top mirror of the Fabry-Perot cavity by anisotropic etching of <1 1 1> oriented silicon wafers. Hybrid etching has also been tried [44] which combines both isotropic and anisotropic etch step. Using this technique, MEMS structures with sizes ranging from 0.05 to 1mm in width were fabricated using CMOS technology. In the above mentioned work, gas phase XeF_2 is used for isotropic etching and Ethylenediamine-pyrocatechol (EDP) or TMAH has been used for anisotropic etching.

1.4.2 Bulk Micromachining

There are many etching methods employed for bulk micromachining. One of them is Plasma/Reactive Ion etching (RIE) in which plasma is formed by applied rf potentials. Gaseous species from the plasma react with the surface atoms forming compounds or molecules. These species then leave the surface as a result of ion bombardment thereby carrying out the etching process.

Li et al. [45] fabricated bi-convex quartz crystal microbalance (QCM) using RIE. They conclude that this technology can etch the quartz crystal independent of the crystal orientation and the accuracy of etching is high and the surface roughness is controllable. Another method called the Deep Reactive Ion Etching (DRIE) is a high aspect ratio silicon etching method, which depends on high density plasma source and an alternating process of etching and protective polymer deposition to achieve aspect ratios of up to 30% [11]. Microfabrication of three dimensional silicon MEMS structures has been carried out by Waits et al. [46] using DRIE. In this paper, the etch selectivity for precise fabrication using DRIE process has been investigated. Ayon et al. [47] has stated that DRIE can be applied in the micro manufacturing of low thrust propulsion systems which will be used in the future generations of micro and nanosatellites as this technology permits the fabrication of high aspect ratio silicon structures. Another popular method called LIGA, which is German acronym for lithography, electroforming, and molding is a micromachining technology that produces high aspect ratio microstructures [48]. In this deep etch process, X-ray lithography is used to transfer a pattern from a mask to thick resist layer on an electrically conductive substrate. This three dimensional structure

generated by means of deep lithography is transferred into a complementary metallic structure by means of electroforming starting from the electrically conductive substrate. In some cases this may be the final product. In general, this is sometimes used for processes like embossing, injection molding etc. In the present work, XeF_2 pulse etching method, which is a vapor phase dry etching method, is employed for the releasing of micromirrors in one of the fabrication procedures outlined in Chapter 4.

1.4.3 Surface Micromachining

Surface micromachining is widely used for making planar structures by selective addition and removal of layers. In surface machining, Muralt et al. [49] has used sputter deposition of the PZT films to fabricate a PZT thin film for micromotors. Lift-off process, another surface micromachining process follows the old-fashioned method to pattern metallic films, wherein it simply allows metal to adhere to the substrate only in regions where it is ultimately desired. A negative mask is used for the metal, exposing only underlying regions where metal is wanted. The edges of the mask are undercut allowing discontinuous metal regions on the substrate and on the mask to be formed. The sacrificial mask is then dissolved away lifting off the unwanted metal. The structuring of anodically bonded evaporated glass used for hermetic sealing is done by lift-off process by Sassen et al. [50]. One of the stated advantages of the lift-off process is their good selectivity to various substrates (in contrast to wet etching) and it does not require dry etching equipment.

1.5 Manufacturing of MEMS devices

Packaging of MEMS devices for specific applications is always a challenge. The success of MEMS will depend upon higher level of functional capability, higher level of integrated electronics and greater number of micromechanical components. The full advantage of MEMS fabrication can be realized by moving them from discrete manufacturing of MEMS devices to integrated MEMS devices. Many fabrication techniques have been proposed to successfully fabricate MEMS devices.

Apart from the available CMOS technology which can be used for fabrication of MEMS devices, there are other industry defined fabrication processes which are specifically meant for MEMS devices.

Multi User MEMS Process (MUMPS) is a highly popular surface micromachining process developed by MCNC [51], in which devices are fabricated using 3 Polysilicon layers, 2 oxide layers and a metal layer. The oxide layers are used as sacrificial layers. Once fabricated, these can be appropriately connected to the electronic circuitry.

A newly developed technology by Micralyne [52], made available to universities in Canada through Canadian Microelectronics Corporation (CMC) [53] uses SOI wafer and bulk micromachining procedures to fabricate MEMS devices. The fabrication procedure called the MicraGEM SOI technology will be very useful to fabricate MOEMS devices based on SOI wafer.

One more industrial CMOS process called Mitel 1.5μm [54] has been effectively used to fabricate MEMS devices. This is a double polysilicon double metal CMOS process which yields the minimum feature size of 1.5μm. This process offers nine layers for MEMS fabrication. Two polycrystalline silicon layers, two metal layers, four insulating layers and a passivation layer which is a combination of silicon nitride and silicon dioxide.

Single Crystal Reactive Etching and Metallization (SCREAM) is a bulk micromachining process patented by McDonald's research group at Cornell University [55] which can be used to release beams with high aspect ratios greater than 50 to 1. This has been effectively used to fabricate micro-channels in both suspended beams and channels embedded into single crystal silicon substrate [56].

Micralyne [52] has introduced a process called Protolyne™ made available to universities in Canada through CMC which is a glass chip technology enabling users to develop a network of bulk micromachined channels and features with eight reservoirs in glass substrate for microfluidic applications.

Sandia National Laboratories [57] created a technology called Sandia-Ultra planar Multi level technology, a five level polysilicon/silicon dioxide surface micromachining technology. Four mechanical levels of polysilicon are fabricated above a thin poly 0 electrical interconnect layer. Two microns of sacrificial oxide is typically sandwiched

between each polysilicon level, which are later etched. This provides a base for designing sophisticated mechanical systems on a chip [58].

MUMPS and MicraGEM processes have been used in the present work to fabricate various types of micromirrors. The detailed process overview and the designs have been discussed in Chapter 4.

1.6 Vibration characteristics and boundary conditioning of MEMS devices

A good performance of an elastic system is dependent on its dynamic behavior which is governed by its natural frequencies and mode shapes, which are in turn dependent on the mass and stiffness properties of the system and boundary conditions . Any structural modification such as stiffening, notching, etc. affects the dynamic behavior of the micro and macro systems. This concept of modification of elastic property of the system through structural modification, support conditions, manufacturing process and other environmental influences is termed as boundary conditioning [59].

The fabrication procedures employed for microsystems lead to different end support conditions that are non-classical in nature and are intermediate between pinned and clamped conditions. Muthukumaran et al. [59-62] used the concept of boundary conditioning using artificial springs on all edges of plate type microsystems in modeling the system to study its dynamic performance.

Boundary conditioning was also done by structural variations as suggested by Rosengren et al. [63] wherein he improved the performance of the condenser microphone with the addition of stiffners and notches in order to modify the system elastic property.

Apart from structural and geometrical variations, there are other factors that can affect the dynamic behavior of the microsystem. One of them is the squeeze film effect. This effect is due to the flow of air in the narrow gaps between electrodes. The viscous damping due to the friction between air or a dielectric medium and the surface of the structure is highly dependent on the ambient pressure, size and geometry of the opening in the structure for the movement of the ambient fluid. The dynamics are strongly affected if the ambient pressure is not zero in close proximity to other surfaces. The squeeze film effect can also create additional spring forces due to fluid compression and inertial forces of mass of the fluid adhering to the surface [64]. At very high oscillation frequencies, velocity of the fluid is very low due to high inertia resulting in low damping and high spring forces. This results in an addition to the stiffness of microsystems due to the movement of ambient fluid medium at very high oscillation frequencies. Another factor which can affect the dynamic characteristics is the Lorentz force, which arises when a conductor carrying a current is subjected to external magnetic field intensity. The frequency of this force can be varied by changing frequency of current. This force can be used to change the elasticity of the structure so as to result in different static and dynamic behavior of structures [59]. The third is the electrostatic force between the electrodes which can affect both the static and dynamic characteristics of the system. This has been dealt in Chapter-3 of the thesis.

In the present work, the natural frequencies and mode shapes of micromirrors are studied under the influence of external electrostatic field which is quantified in the form of elastic foundation stiffness through the concept of boundary conditioning. Also the micromirrors are boundary conditioned at the support using artificial translational and rotational springs.

1.7 Testing of MEMS devices

The successful operation of any device fabricated through microfabrication depends heavily on the performance testing of the device. Hence it is important to devise a test method that can test a device for all the required performance. The dynamic properties of MEMS devices such as natural frequencies and response to external excitation are essential. For example, a number of MEMS devices like gyroscopes and accelerometers use external electrostatic forces as a means of tuning the device natural frequency and thereby to actively control the sensitivity of the device to a broad band of excitation frequencies [65].

Ando et al. [66], describe the testing of a comb actuator. They analyze the motion of the traveling table and come up with a relation between the traveling table motion and the driving voltage. Li et al. [67], use Fizeau laser interferometer in order to measure the surface roughness of the optical flat. This interferometer is based on phase shifting interferometry. When measuring the optical flat, constant phase difference exists between any two points. Any change in surface roughness will result in a phase shift which is calibrated.

Micromirrors have been earlier tested by dynamical simulation [68]. In this, both the electrostatic and mechanical models were required to simulate the dynamic characteristics of micromirror system. Electrostatic coupled structural transient analysis was used to calculate the resulting deflection as a function of time and input voltage change. However, literature is scarce on the testing fixtures used to test the micromirrors to accurately measure the tilting angles and dynamic characteristics such as the natural frequency of the micromirror.

1.8 Objectives and scope of the present research work

The performance of electrostatically actuated devices is very much dependent on their static and dynamic behavior. But the dynamic behavior of microdevices is influenced by geometry, process limitation and electrostatic field. Hence, there is a necessity to develop design synthesis. This could involve all the above factors in a unified way. This thesis extends the application of boundary conditioning to include the influence of electrostatic field in a unified way through modeling, fabrication and testing.

1.8.1 Objectives

Synthesizing a functional MEMS device involves the following: a design of the device, unified modeling, choosing the correct microfabrication technique, implementing the micromirror device using the appropriate microfabrication procedure and experimental verification of the microfabricated device.

The main objectives of the present thesis are (i) to study of the effects of electrostatic field on static and dynamic behavior of mirrors of different configurations with stopper, main and counter electrodes suiting different microfabrication technologies,

(ii) modeling the influence of electrostatic field using artificial elastic foundation through boundary conditioning concept with Rayleigh-Ritz method, (iii) study of feasible micromachining methods in order to make these mirrors, (iv) experimental verification of the static and dynamic behavior of electrostatically actuated micromirrors.

1.8.2 The scope of thesis

The thesis is organized as follows:

1. Study on the effects of electrostatic forces on different types of torsional micromirrors and design of micromirrors based on different fabrication technologies are given in Chapter-2.
2. Development of a unified concept to synthesize the influence of the electrostatic field and the support conditions on the dynamic behavior of micromirrors. The modeling of boundary conditions due to the supports and external influence of electrostatic field are outlined in Chapter-3.
3. Fabrication of the mirror using two industrial fabrication methods and an in-house method using the gas phase XeF_2 are discussed in Chapter-4.
4. Experimental test results are presented in Chapter-5 in order to validate the design synthesis.
5. The Chapter-6 presents the conclusions and possible future extensions of the present work.

Chapter-2

Effects of electrostatic field on the dynamics of torsional micromirrors

2.1 Introduction to electrostatic actuation

Chapter 1 provided a brief explanation on the electrostatic actuation principle. In this chapter the principle of electrostatic actuation is applied to 90° torsional micromirrors and another type of torsional micromirrors referred to as one dimensional scanning micromirrors. For MEMS actuators, electrostatic actuation is preferred over other actuation principles due to its simplicity in approach and predictable performance as mentioned in Chapter 1.

The concept of electrostatic actuation can be explained with two parallel plate electrodes separated by a dielectric medium. When a bias voltage 'V' is applied between the two electrodes, an electrostatic field is established between them. The force due to the electrostatic field is given by

$$F = \frac{\varepsilon_o \varepsilon_r A V^2}{2d^2} \qquad 2.1$$

where,

F – Electrostatic force.

A – Surface area.

V- Applied bias voltage.

d - Gap between the electrodes.

ε_o - permittivity of free space, 8.85×10^{-12} F/m.

ε_r - relative permittivity of the dielectric medium.

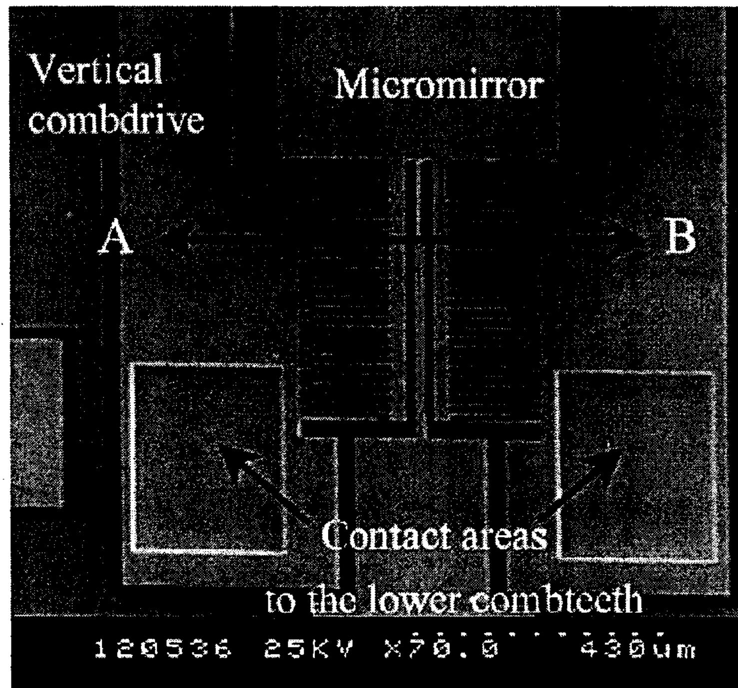

Fig. 2.1 SEM picture of the top-view of a double sided micromirror [69]

Lee [69] proposed a single-crystalline silicon micromirror actuated by self-aligned vertical electrostatic combdrives. These combdrives have multi-level electrical isolation that allows bi-directional and dual mode operation. The dual mode operation includes independent rotation and piston motion. In piston motion the movable electrode will move linearly with respect to the fixed electrode similar to the motion of a piston in a cylinder. Figure 2.1 shows the SEM of the mirror with combdrives. The combdrive has

fixed lower teeth and movable upper teeth. A driving voltage between either of the two adjacent lower fixed teeth can give a bidirectional rotation to the micromirror.

Hao et al. [70] has fabricated a two dimensional electrostatic torsion micromirror as shown in Figure 2.2. The mirror which is the top electrode is octagonal in shape as

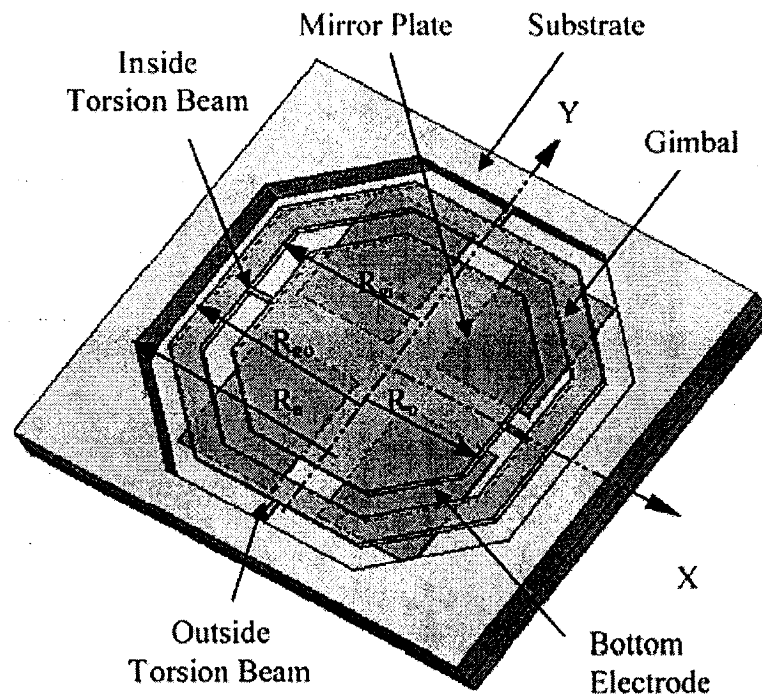

Fig. 2.2 Schematic view of the mirror [70]

shown in figure and gold is coated on top for higher reflectivity. The mirror is held by two torsion beams supported by a rigid gimbal. Four electrodes separated from each other are provided at the substrate. A bias voltage supplied between the mirror and the two bottom electrodes deflect the mirror. Further two types of torsion beams, a straight beam and a serpentine beam were used to study the different effects.

In this chapter electrostatic actuation of a typical torsional micromirror is analyzed for its rotation angle and its natural frequency for different voltages. The bias voltage applied should not exceed the pull-in voltage which is defined as the voltage beyond which the electrostatic torque exceeds the mechanical resisting torque rendering the micromirror unstable. If the bias voltage exceeds the pull-in-voltage the mirror snaps due to excessive attraction towards the substrate.

Degani et al. [71] undertook the study of pull-in phenomena in electrostatic microactuators. In his paper, the electrostatic torsional microactuator is used as micromirror. Initially modeling of electrostatic torque was carried out. When the electrostatic torque exceeds the mechanical torque due to the beams supporting the proof mass, the plates touch each other. Using this condition they derived a polynomial algebraic equation for the pull-in voltage and pull-in angle for a torsion microactuator.

The present chapter has results on pull-in voltage and pull-in angles which are also referred to as snap voltage and snap angles, respectively. Further, the settling time for different conditions of 90° micromirrors for an applied bias voltage has also been presented. The two dimensional micromirrors are analyzed considering the two types of fabrication processes which are MUMPS and bulk micromachining using Silicon On Insulator (SOI) wafers.

2. 2 Modeling of switching response of 90° torsional micromirrors

A schematic representation of the 90° torsional micromirror considered in this thesis is given in Figure 2.3. The micromirror is sustained by torsional beams clamped at the ends as shown. The substrate acts as a fixed electrode while the micromirror is the moving electrode.

Tilting of the micromirror is accomplished by applying a bias voltage 'V' between the substrate and the micromirror, which creates an electrostatic field between the mirror and the substrate pulling the micromirror towards the substrate. 'T_e' is the torque due to the electrostatic force on the micromirror. The tilting will also give rise to a counter mechanical resisting torque 'T_m' from the torsional beams supporting the micromirror as shown in Figure 2.3. Also from Figure 2.3, 'd' is the initial gap between the mirror and the substrate, 'θ' is the angle in radians, 'L' is the length of the micromirror and 'W' is the width of the micromirror. A stopper of height 'H_s' on the substrate increases the force due to its electrostatic field helping the micromirror to attain a 90° tilt angle. In its tilted state, the mirror can effectively reflect the light in the desired direction. The mirrors can be tilted to any desired angle through application of required voltages.

The earlier model [72] of torsional micromirror considered only the electrostatic field effect due to the main electrode and neglected the counter electric field as shown in Figure 2.4 (a). In the present study, the effect of the counter electric field and the field

due to an additional stopper electrode are considered in analyzing the dynamic behavior of the micromirror as shown in Figure 2.4 (b).

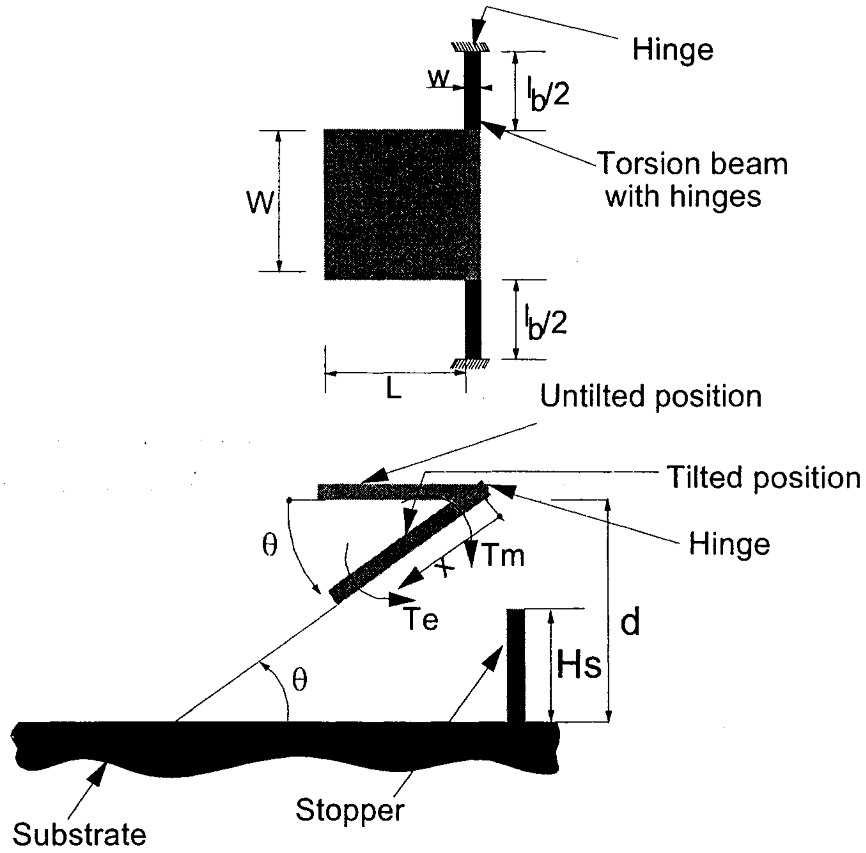

Fig. 2.3 Scheme of a 90° torsional micromirror

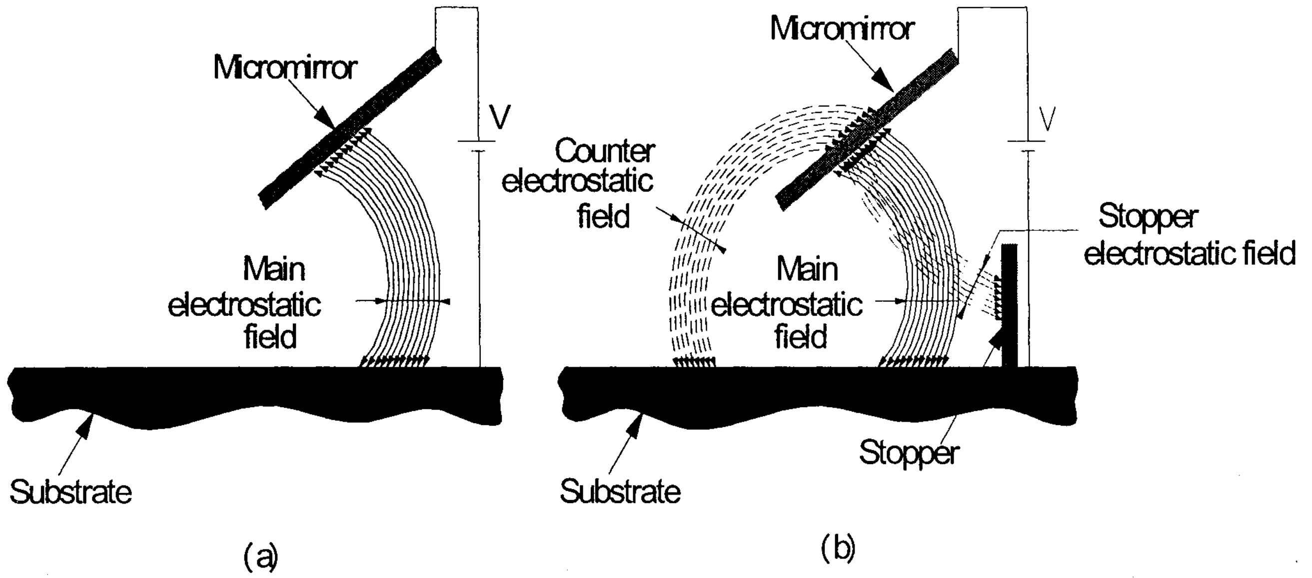

Fig. 2.4 Schematic representation of electrostatic fields. Electrostatic field is present throughout the length of the mirror and stopper electrodes.

Thus, the net electrostatic torque on the micromirror can be obtained as

$$T_e = T_{eM} + T_{eC} + T_{eS} \qquad 2.2$$

where 'T_e' is the net electrostatic torque, 'T_{eM}' is the electrostatic torque due to the main electric field, 'T_{eC}' is the electrostatic torque due to the counter electric field and 'T_{eS}' is the electrostatic field due to the stopper electrode. The main electrostatic torque can be obtained as [72],

$$T_{eM} = \left(\frac{\varepsilon_r \varepsilon_o V^2 W}{2}\right) \int_0^L \frac{x}{(((d/\sin\theta) - x)\theta)^2} dx \qquad 2.3$$

The electrostatic torque due to the counter electrostatic field is

$$T_{eC} = -\left(\frac{\varepsilon_r \varepsilon_o V^2 W}{2}\right)\int_0^L \frac{x}{(((d/\sin(\pi-\theta)-x)(\pi-\theta))^2}dx \qquad 2.4$$

and that due to the stopper electrostatic field is

$$T_{eS} = \left(\frac{\varepsilon_r \varepsilon_o V^2 W}{2}\right)\int_{L1}^{L} \frac{x}{\left(x(\frac{\pi}{2}-\theta)\right)^2}dx \qquad 2.5$$

where, 'W' is the width of the micromirror, 'L' is the length of the micromirror, 'ε_r' is the relative permittivity of air, 'ε_o' is the dielectric constant of vacuum, 'd' is the initial spacing between the electrodes, 'H_s' is the stopper height, L_1 = (d-H_s), 'θ' is the tilt angle.

The resisting mechanical torque 'T_m' is given by [72]

$$T_m = 2\left(\frac{Gwt^3}{3l_b}\right)\theta\left[1-\left(\left(\frac{192}{\pi^5}\right)\left(\frac{t}{w}\right)\left(\tanh\left(\frac{\pi w}{2t}\right)\right)\right)\right] \qquad 2.6$$

where, 'w' is the width of the beam, 'l_b' is the length of the beam, 'G' is the modulus of rigidity and 't' is the thickness of the micromirror. The design parameters used for the analysis are given in Table 2.1.

A typical variation of mechanical resisting torque (T_m) and the net electrostatic torque (T_e) at different bias voltages are given in Figure 2.5. It can be seen that as the voltage is increased the electrostatic torque increases non-linearly while the mechanical torque

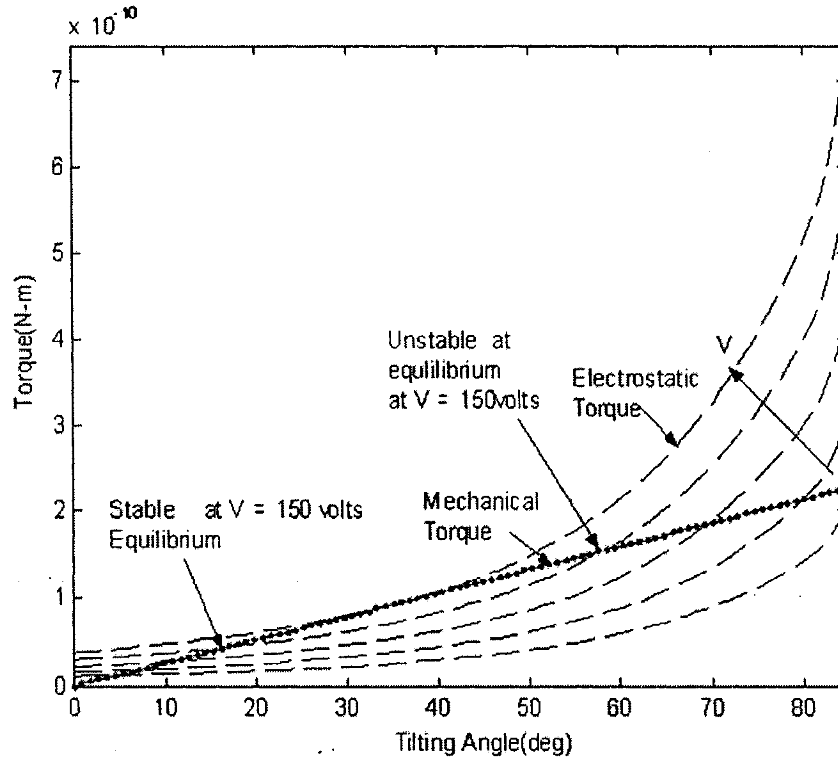

Fig. 2.5: Typical variation of electrostatic torque at different voltages and mechanical torque with respect to the tilting angle

W	L	w	l_b	ε_r	ε_o	d	G	t
600 μm	300μm	16μm	320μm	1	8.85 x 10^{-12}F/m	305μm	73 GPa	0.4μm

Table 2.1 Design parameters of a 90° torsional micromirror

varies linearly with tilt angle. For a given voltage, there exists an initial static equilibrium position where electrostatic torque is equal to the mechanical torque. This first equilibrium position determines the static or the optical scan angle of the micromirror. It is thus possible to estimate the static angle or the optical scan angle of the

micromirror by equating Equations 2.2 and 2.6. If the tilt angle is increased above the first equilibrium position, until the second equilibrium position, electrostatic torque is always lower than the mechanical resisting torque ensuring stable operation. Whenever the mirror is tilted beyond the second equilibrium position, the electrostatic torque exceeds the mechanical resisting torque resulting in snap or pull-in. Hence, the second equilibrium position is called "Snap Angle" for a given voltage. As the voltage is increased, the scan angle increases and the snap angle decreases in such a way that there exists no scan angle beyond a certain voltage called pull-in voltage. The second unstable equilibrium position determines the snap point or the pull-in point of the micromirror.

The equation of motion for the micromirror is given as

$$J\ddot{\theta} + C\dot{\theta} + K_{eq}\theta = 0 \qquad 2.7$$

where, 'J' is the polar mass moment of inertia about the hinge axis, 'C' is the damping coefficient and 'K_{eq}' is the equivalent stiffness given by

$$K_{eq} = K_m - K_e \qquad 2.8$$

where, '$K_e = \frac{dT_e}{d\theta}$' is the stiffness weakening due to the electrostatic field and '$K_m = \frac{dT_m}{d\theta}$' is the mechanical stiffness.

Electrostatic stiffness and mechanical torsional beam stiffnesses are obtained at the static equilibrium position and the natural frequency of the micromirror is hence obtained for the various bias voltages by estimating the equivalent stiffness of the

micromirror at the scan angle position. Hence, the undamped natural frequency is estimated as

$$\omega = \sqrt{\frac{K_{eq}}{J}} \text{rad/sec} \qquad 2.9$$

The results are obtained for voltage range of 0- 150 volts. As an example, the analysis is carried out for a voltage value of 150V. In order to demonstrate the improvement due to the proposed method, the different configurations of electrostatic fields on micromirror are considered as follows:

A) The electrostatic torque due to the main electrostatic field only.

B) The net electrostatic torque due to the main and the counter electrostatic fields.

C) The net electrostatic torque due to the main, counter and stopper electric fields.

In the third case, three values of stopper heights 20μm, 40μm and 60μm are considered. The natural frequency of the micromirrors for the above mentioned three cases are obtained for the respective bias voltages and stopper configurations. The study compares the results obtained for the above three cases. The response of the micromirror under these conditions was also obtained for the specified voltage with the damping coefficient of $C = 8.75 \times 10^{-12}$ Nm sec/rad which corresponds to a published damping ratio of 0.164 [73] for a micromirror device.

2.2.1 Results and discussion

The electrostatic torque and mechanical resisting torque obtained for Case (A) for tilt angles 0 to 90°, are illustrated in Figure 2.6. This figure shows that in the presence of only the main electrostatic field, the electrostatic torque increases after the unstable snap equilibrium. This indicates that the mirror will never be able to attain 90° position. However a micromirror under electrostatic actuation is not only subjected to the direct electrostatic field but also the counter electrostatic field as shown in Figure 2.4 (b). If counter electrostatic field is considered, it decreases the net electrostatic torque after the unstable equilibrium and consequently the micromirror attains a third equilibrium position as shown in Figure 2.7. As a result, the micromirror is unable to attain the full desired 90° tilt for optical switching applications. When a stopper electrode of sufficient height is added as shown in Figure 2.4(b), it introduces an electrostatic field in support of the main electrostatic field resulting in the electrostatic torque as shown in Figure 2.8 that resembles the behavior as shown in Figure 2.6. This figure demonstrates the significant effect of counter electrostatic field and the field due to the stopper electrode on the rotation of the torsional micromirror. The individual variation of electrostatic torques with the rotation of the micromirror is given in Figure 2.9 for the stopper height of 20μm. It can be noticed that the counter electrostatic field works in the opposite direction of main and stopper electrostatic fields and also becomes significant after around 60° of tilt angle. The presence of counter electrostatic field thus limits the maximum angle that can be obtained with only the main electrode. It can also be seen that the torque due to stopper electrode becomes significant after around 85°. Hence the presence of stopper electrode becomes essential in order to obtain the required 90° tilt angle.

The predicted tilting angles of the micromirror at the three equilibrium positions mentioned earlier, at different bias voltages, are shown in Figure 2.10. It can be observed that the static or the optical scan angle increases with increase in voltage. The maximum scan angle is limited to around 30°. The pull-in-voltage occurs at approximately 170 volts, which is indicated in Figure 2.10.

As stated earlier, for Case (C), stopper electrodes of 3 different heights were considered in this study. In order to demonstrate the influence of stopper electrode, the scan angles were predicted for different voltages as shown in Figure 2.11. It can be noted that as the stopper height is increased, the scan angle of the micromirror significantly increases until it snaps. The maximum scan angle is obtained for the stopper height of 60μm. It can also be inferred from Figure 2.11 that increase in stopper height reduces the pull-in voltage.

The natural frequency of the torsional micromirror is estimated using Equation 2.9 for different cases as shown in Figure 2.12. It can be seen that the counter electrostatic field has a stiffening effect which increases the natural frequency while that due to the main electrodes reduces the natural frequency. The electrostatic field due to the stopper electrode helps the action of the main electrode and brings down the natural frequency.

The transient response and settling time of the micromirrors are very important for optical switching applications. The transient response is obtained from the non homogeneous equation,

$$J\ddot{\theta} + C\dot{\theta} + K_m\theta = T_e(V,\theta) \qquad 2.10$$

where, T_e corresponds to a step input of 150 volts.

The resulting step response for different cases shown in Figure 2.13 is in agreement with the corresponding predicted scan angles and natural frequencies. It can be seen that the 2% settling time (which is the time required to reach $\pm 2\%$ of the steady state value) of the micromirror is around 6 milli seconds which makes the device useful for many applications. The results indicate that the presence of counter and stopper electrostatic fields have significant influence on static and dynamic response of torsional micromirrors. From the analysis presented above it can be concluded that a stopper of sufficient height is quite effective in increasing the tilting capability of the micromirror. It was also demonstrated that the counter electrostatic fields and that due to stopper electrode influence the equilibrium scan angle and natural frequency significantly.

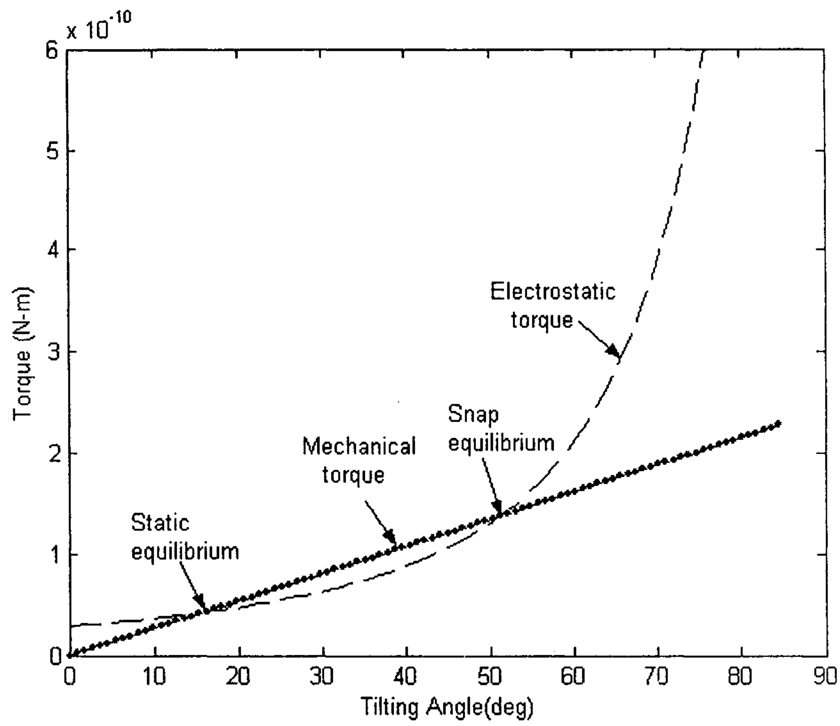

Fig. 2.6 Variation of electrostatic torque for Case (A).

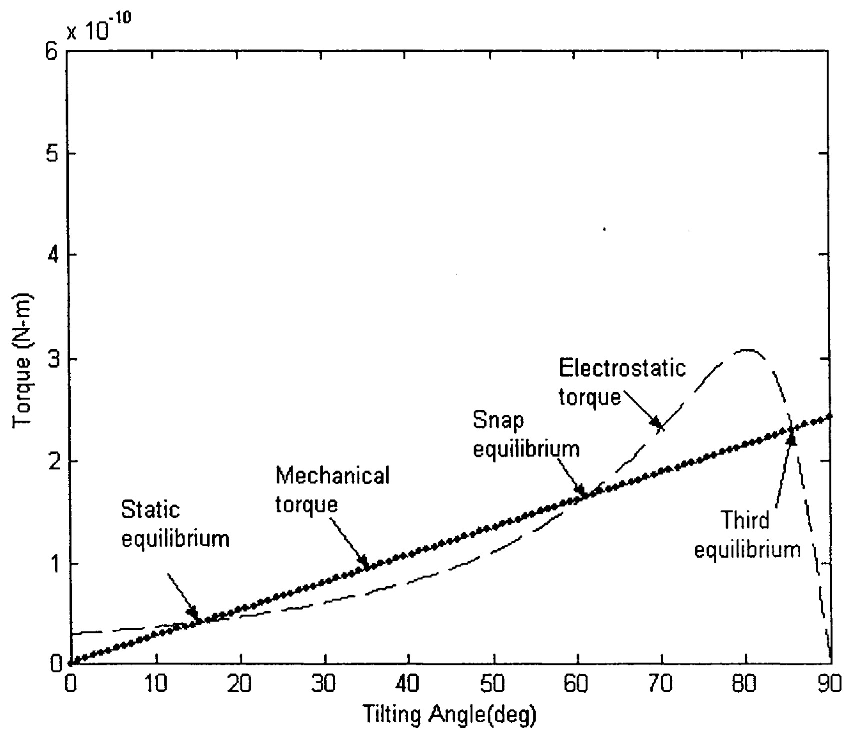

Fig. 2.7 Variation of electrostatic torque for Case (B).

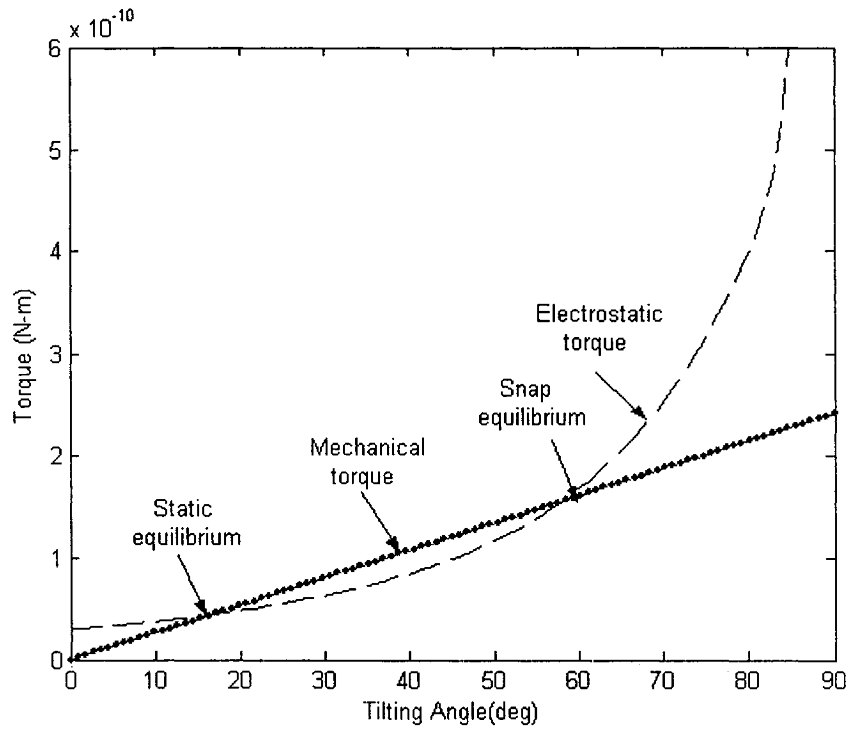

Fig. 2.8 Variation of electrostatic torque for Case (C) for Hs = 20μm

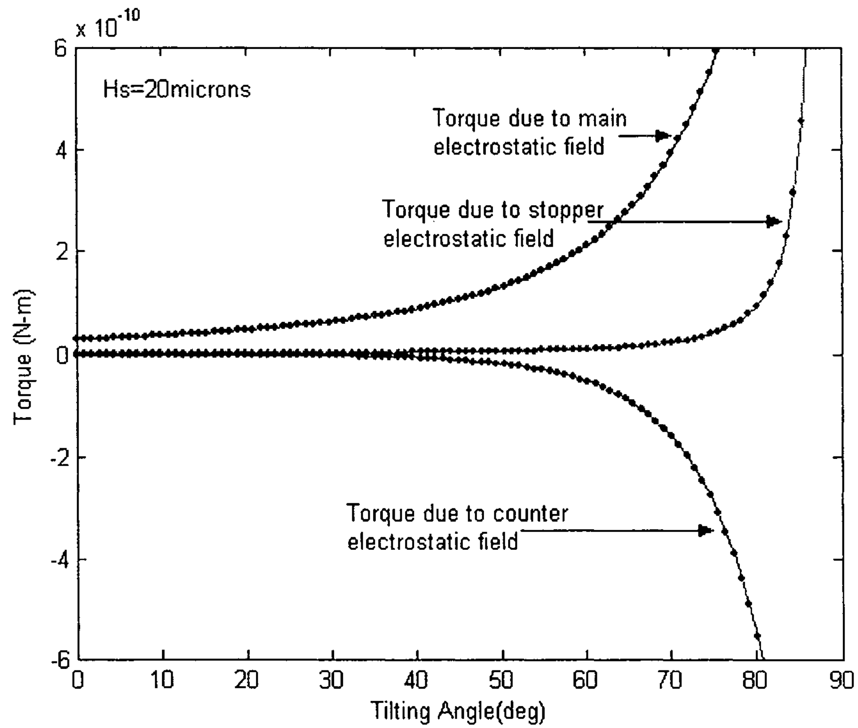

Fig. 2.9 Variation of individual electrostatic torques for V=150 volts

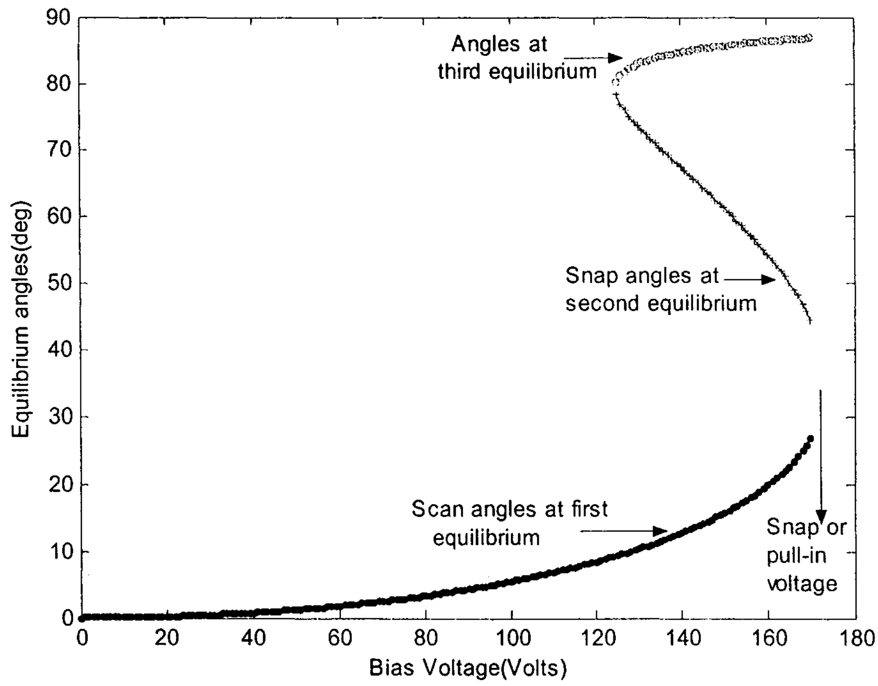

Fig. 2.10 Variation of equilibrium angles.

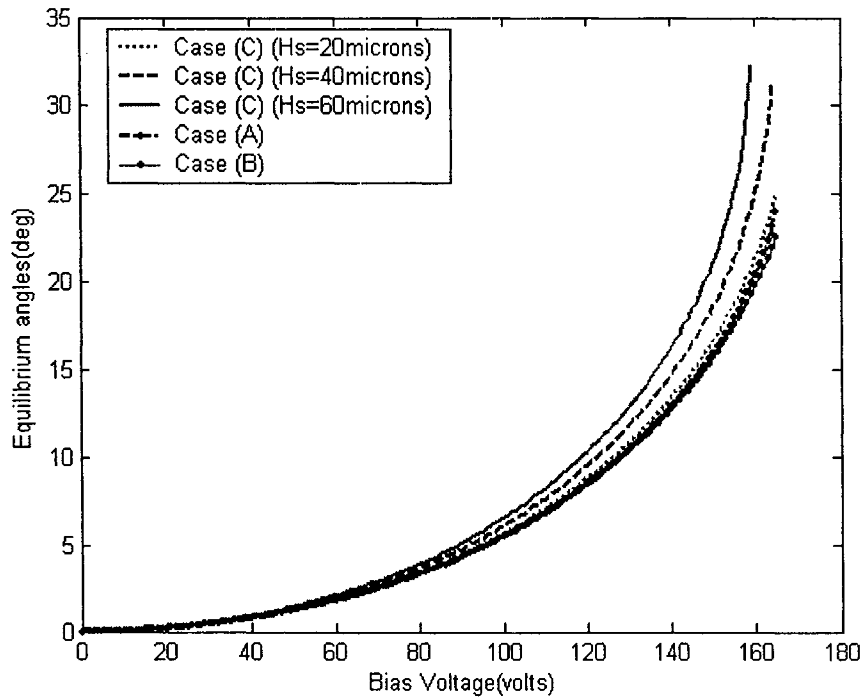

Fig. 2.11 Influence of voltages on scan angles for different cases

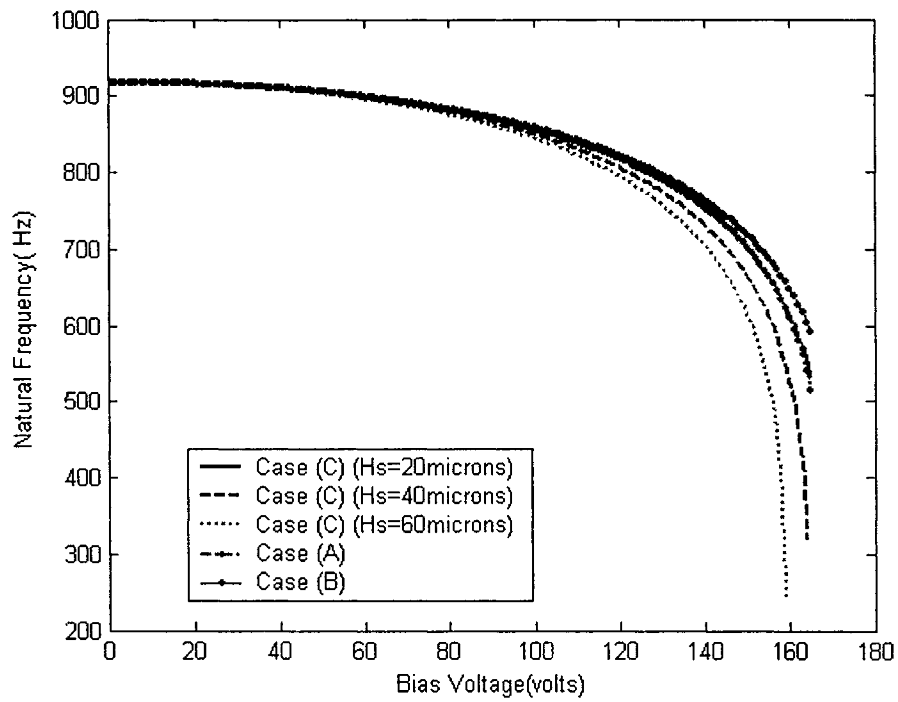

Fig. 2.12 Influence of voltages on natural frequency of the micromirror for different cases

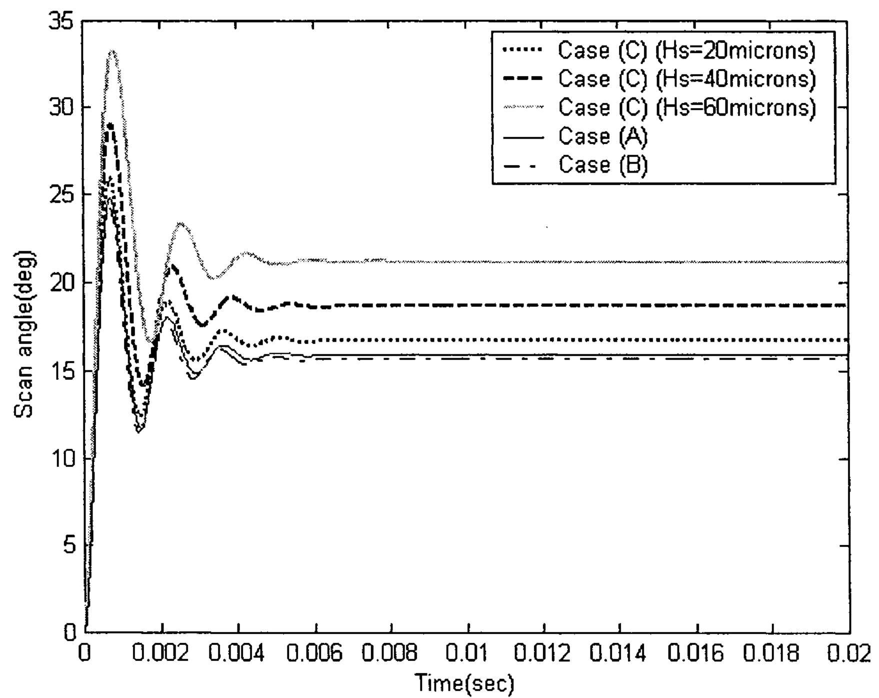

Fig. 2.13 Response of the micromirror for the three cases at 150 volts.

2.3 Conceptual design of a one dimensional scanning micromirror based on MUMPS and SOI bulk micromachining fabrication procedures

The schematic of the one dimensional scanning micromirror considered for design is shown in Figure 2.14. The micromirror shown has two electrodes both based on the substrate. The micromirror is supported by the torsion beam which is hinged at the anchors as shown in the figure. The tilt of the micromirror is by electrostatic actuation. A bias voltage (V) is applied between the mirror and electrode 1 while applying no voltage between the mirror and electrode 2, as shown in Figure 2.15, will tilt the mirror in the direction of electrode 1. The maximum tilt (θ) that the scanning micromirror can attain is limited by the length of the micromirror (L) and gap (d) between the micromirror at zero deflection and the substrate.

In this design, the effect of counter electrostatic field is not considered since the electrode dimensions do not exceed the mirror dimensions and hence the top surface of the mirror is not subjected to any electrostatic field. Hence the net electrostatic torque is only due to the main electrode which is given by modified Equation 2.3 as

$$T_e = \left(\frac{\varepsilon_r \varepsilon_0 V^2 W}{2}\right) \int_{L_1}^{L_2} \frac{x}{\left(\left((d/\sin\theta) - x\right)\theta\right)^2} dx \qquad 2.11$$

where, $(L_2 - L_1)$ gives the width of the electrode as shown in Figure 2.15

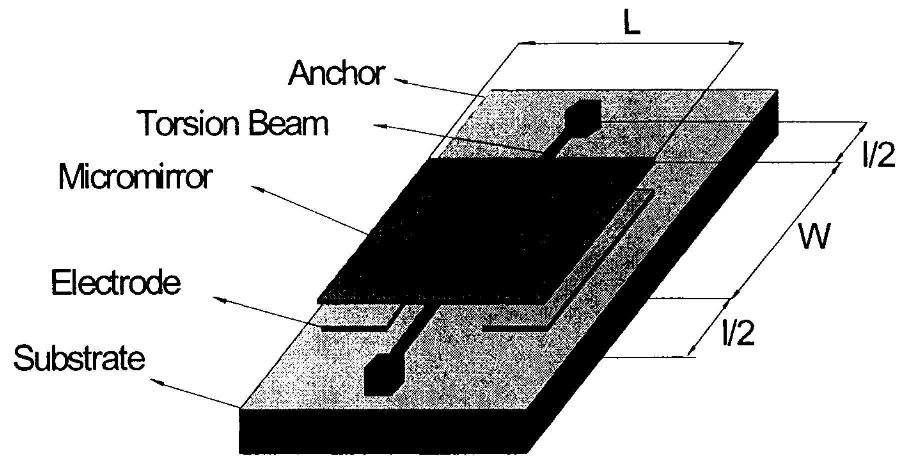

Fig. 2.14 Schematic of one dimensional scanning mirror

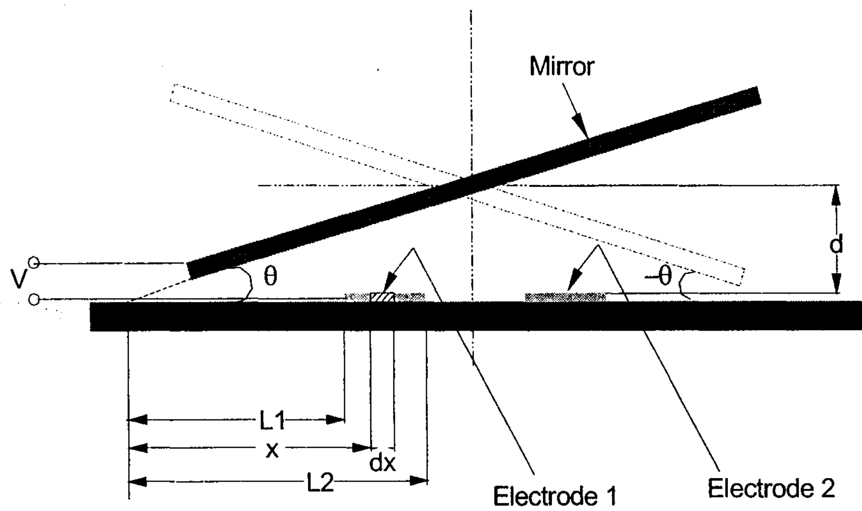

Fig. 2.15 Side view of the schematic of the micromirror

The mechanical restoring torque due to the torsional beams is given by Equation 2.6 where 'l_b' is the length of hinge which is equal to 'l/2' as shown in Figure 2.14.

Chapter 1 presented a brief description of bulk micromachining process and also an example of surface micromachining process called the Multi User MEMS Process (MUMPS). MUMPS is an industrial microfabrication technology which allows only a fixed electrode gap of 2.75μ as the layers used for fabrication has predefined thicknesses. However with bulk micromachining process variable electrode gaps can be obtained depending on the type of wafer used. In the present work a Silicon On Insulator (SOI) wafer is used. As this type of wafer is made of three layers as explained in Chapter 1, the back side etching of the wafer can be done. Depending on the thickness of the bottom or the handle layer of the SOI wafer, different electrode gaps can be obtained. Hence there is a possibility of obtaining higher tilting angles with increase in voltage. The other advantages of using SOI wafers for micromirror devices are higher optical reflectivity and minimal residual stress.

2.3.1 Designs based on MUMPS microfabrication technique

In MUMPS the thickness of different layers used are fixed by the design rule. The Table 2.2 below gives a description of the thickness of different layers used in MUMPS [74]. In order to attain the maximum gap the Poly2 layer is used to fabricate the micromirror and Poly0 layer will act as the electrodes. The combined thickness of the First Oxide and Second Oxide which are the sacrificial layers will constitute the electrode gap. Hence the total gap is 2.75μ as given in Table 2.2.

Material Layer	**Thickness (μm)**
Silicon Nitride	0.6
Poly0	0.5
First Oxide	2.0
Poly1	2.0
Second Oxide	0.75
Poly2	1.5
Metal	0.5

Table 2.2 Thickness of layers used in MUMPS

It is necessary for the design to carry out the parametric studies on length (L), width (W) hinge length (l) and the mirror geometry for the fixed gap (d) of 2.75μm between the micromirror and the bottom electrode. The following Table 2.3 gives the two cases of dimensions of the scanning micromirror designed considering MUMPS.

Mirror	Case 1	Case 2
Width(W), μm	100	200
Length(L), μm	100	200

Table 2.3 Mirror design parameters for MUMPS.

The hinge lengths (l) considered for each of the above listed dimensions are 50μm, 70μm, 90μm, 120μm. The width of the torsional beam was considered to be 4μm.

2.3.2 Designs using SOI based bulk micromachining process

The following is the numerical exercise based on SOI technology in order to study the improvements over MUMPS technology. Bulk micromachining gives a lot of flexibility when compared to MUMPS due to the various design possibilities as discussed earlier. The gap between the micromirror and the substrate can be larger than in the MUMPS process. The dimensions of the micromirror can be larger than the assumed dimensions of the MUMPS designed micromirrors. However with increase in electrode gap a higher bias voltage will be required to tilt the micromirror. With increase in electrode gap, the tilting of the micromirror also increases.

Mirror	Case 1	Case 2
Width(W),μm	500	1000
Length(L),μm	500	1000

Table 2.4 Mirror design parameters for SOI based bulk micromachining.

Table 2.4 gives the dimensions considered for the design for the bulk micromachining process. The hinge lengths (l) assumed for the above cases were 600μm, 680μm, 760μm and 840μm. The width of the hinge was assumed to be 16μm. The gap between the mirror and the substrate (d) is 250μm.

2.3.3 Results and discussion

The results obtained outline the performance of the one dimensional scanning micromirrors with the dimensions suited for MUMPS and SOI based bulk micromachining processes. The results present the static angles at each bias voltage, natural frequency and pull-in voltage for the cases considered for the respective microfabrication conditions. The natural frequencies in both the cases decrease with increase in voltage. The maximum angle that a mirror of particular dimension can tilt is given by

$$\theta_{max} = \tan^{-1}\left(\frac{2d}{L}\right) \qquad 2.12$$

The maximum stress noted in any of the designs discussed so far is less than 700MPa, which poses no problem for mechanical integrity.

2.3.3.1 Results obtained for MUMPS designs

The Figures 2.16 (a), (b) and (c) and Figures 2.17(a), (b), and (c) give the results obtained for MUMPS designs for the two cases, respectively. Figure 2.16 (a) gives the result on the static angles for different bias voltage for Case 1 of MUMPS. From this figure it can be observed that for a shorter hinge length the static angle is lower than that for a longer hinge length for a given voltage. Also the snap voltage or the pull-in voltage is higher for a shorter torsion beam compared to the longer torsion beam. Also if the dimension of the hinge is increased, the static angle is increased as observed in Figure 2.17 (a) for a given voltage. However, the natural frequencies of mirrors are higher for shorter beams

because the stiffness associated with the beams of shorter hinge lengths leads to higher stiffness values as observed in Figure 2.16 (b) and 2.17(b). From Figure 2.16 (c) and 2.17 (c) the pull-in voltages for case 1 and case 2 MUMPS fabricated mirrors can be determined at the point where the snap angles and the static angles meet. Here also a smaller hinge has a higher pull-in voltage. From this it can be concluded that the dimensions chosen when the electrode gap is low should be preferably small for effective switching operations. This, however, limits the design of the micromirror for higher dimensions. Also one of the other disadvantages of using MUMPS for micromirrors is the existence of residual stress which in polysilicon is very high. Hence, larger dimensions result in curving of the mirrors rendering the micromirrors ineffective. The surface also has etch holes and is not polished leading to reduced optical reflectivity. The advantage with the MUMPS process is that the bias voltage required is lower compared to that for the bulk micromachining as the electrode gap is smaller compared to the bulk micromachining process.

2.3.3.2 Results obtained for SOI bulk micromachining process

When compared to MUMPS process, the results obtained through SOI based bulk micromachining are quite promising. Figures 2.18 (a), (b) provide the results of static angles and natural frequency for Case 1 based on SOI bulk micromachining process. Similarly Figures 2.19 (a), 2.19 (b) and 2.19 (c) provide the results on static angles, natural frequency and pull-in voltage for Case 2 of SOI bulk micromachining process. Since a higher electrode gap can be assumed through this process, the static angles or the

tilting angles obtained will be higher. This flexibility in choosing the electrode gap is a major advantage of SOI bulk micromachining process over MUMPS. Figures 2.18 (b) and 2.19 (b) show the natural frequencies for the two cases considered. Here the natural frequency of the mirror is very low because of a longer torsion beam. This will lead to a slow response of the mirror effecting the switching operation. As the electrode gap is higher, it will lead to a higher pull-in voltage. In the case 1 of SOI based bulk micromachining process, it was observed that the pull-in voltage was higher than 250 volts; hence it is not critical to find the pull-in voltage. For case 2 of the same process, the pull-in voltage was found to be 125 volts as determined by Figure 2.19 (c). A higher pull-in voltage would result in providing a longer stable range of operation for the micromirror which will help in getting a better switching effect. The other advantage of using Silicon On Insulator (SOI) wafer is minimal residual stress. This will rule out constraints while designing due to dimensions of micromirrors. Also it is observed from Figure 2.18 (a) and 2.19 (a) that larger dimensions lead to higher scan angle.

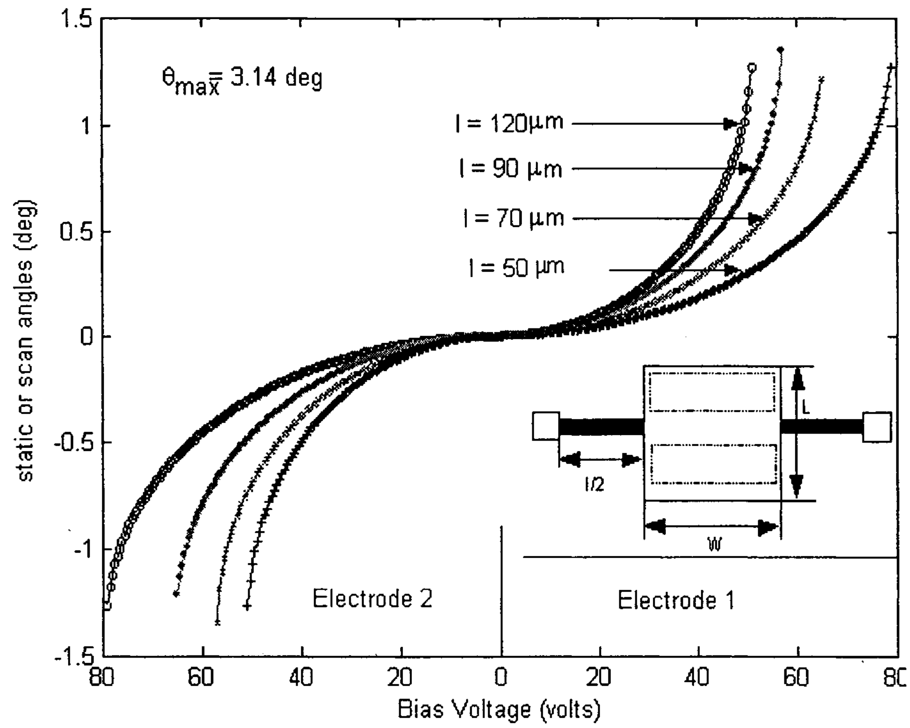

Fig. 2.16 (a) Tilting or scan angles for L = 100μm and W = 100μm of mirror dimensions (Case 1) of MUMPS for different bias voltages

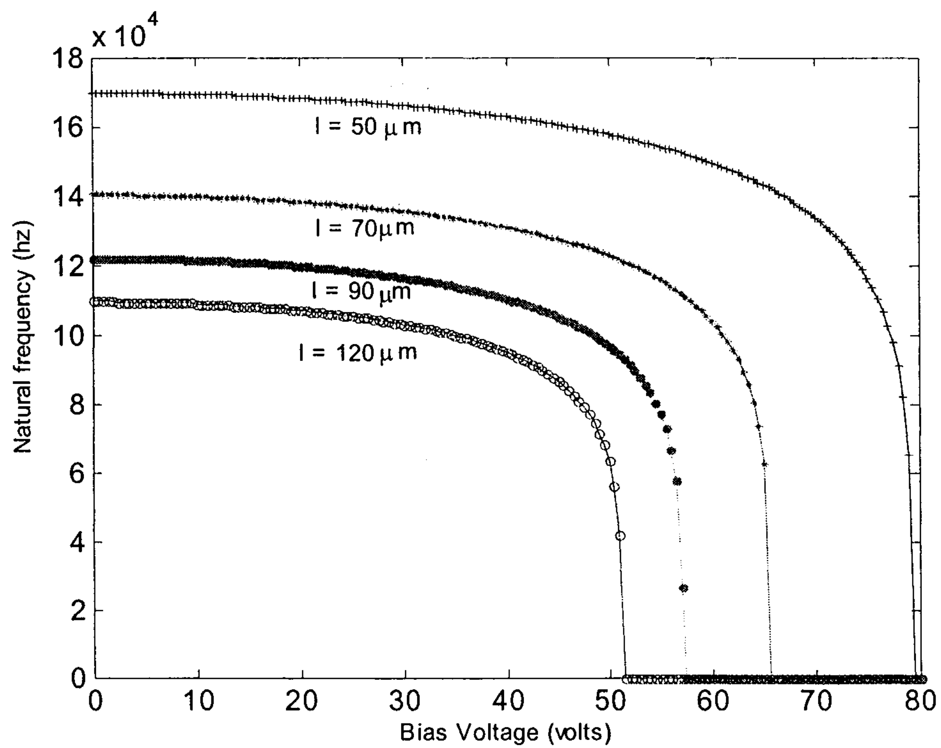

Fig. 2.16 (b) Variation of natural frequency with bias voltage for different hinge lengths for Case 1 of MUMPS

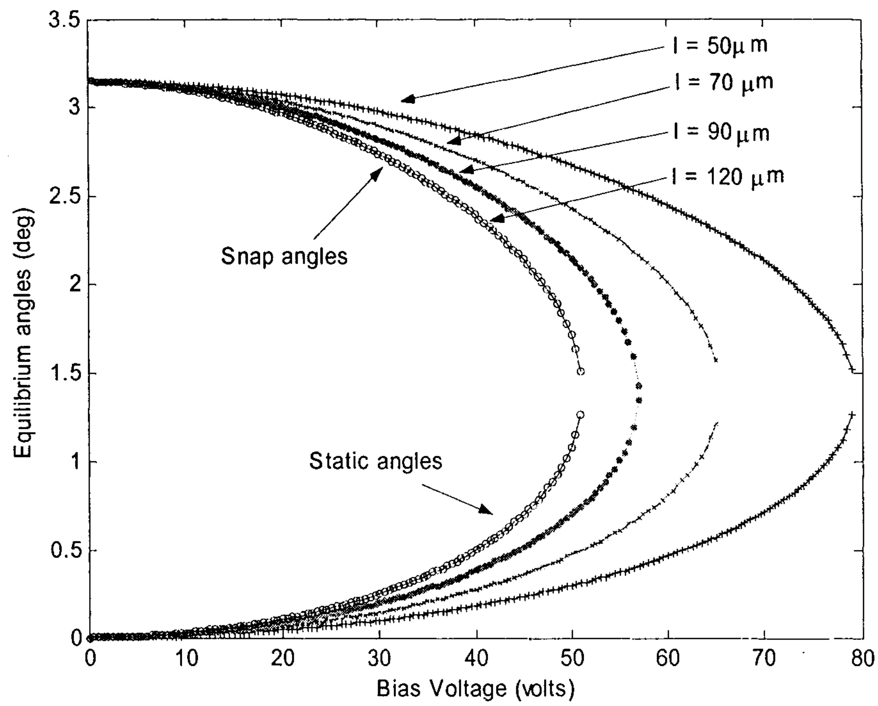

Fig. 2.16 (c) Equilibrium angles determining the pull-in voltage for different hinge lengths for Case 1 of MUMPS

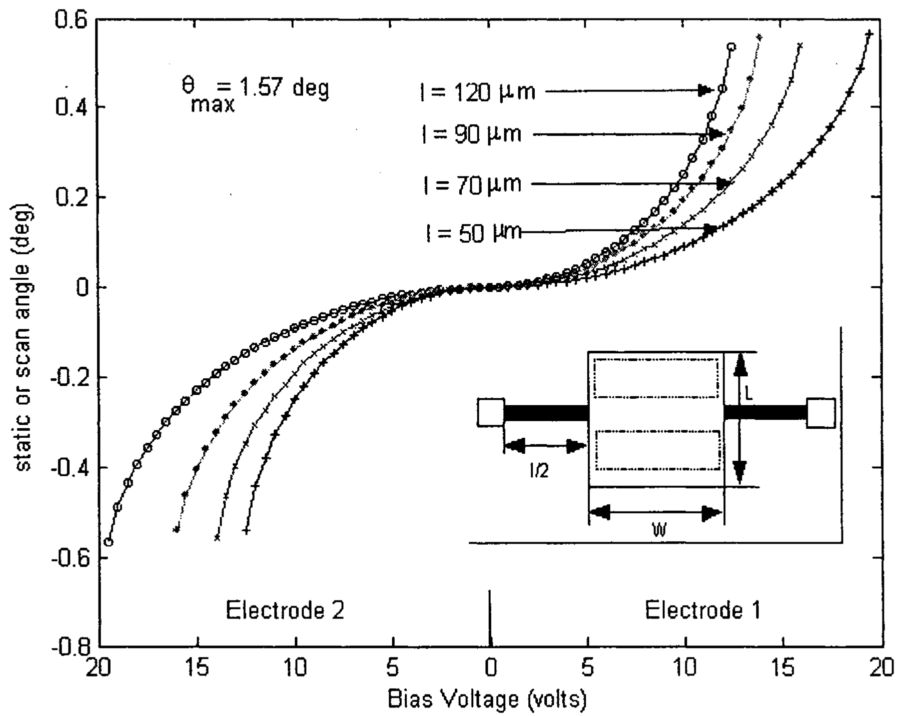

Fig. 2.17 (a) Tilting or scan angles for L = 200μm and W = 200μm of mirror dimensions (Case 2) of MUMPS for different bias voltages

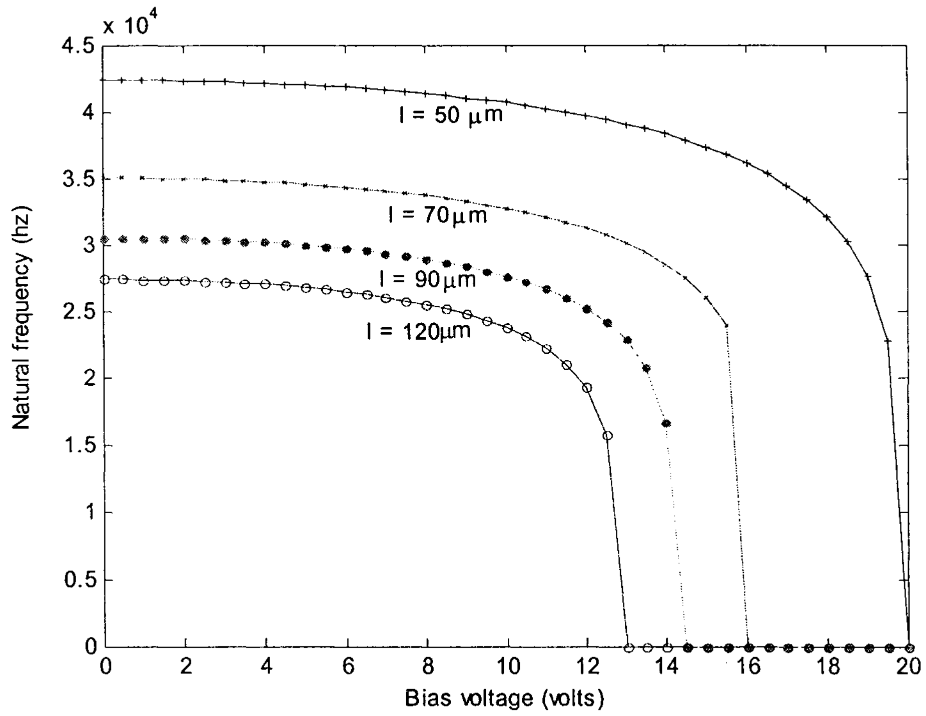

Fig. 2.17 (b) Variation of natural frequency with bias voltage for different hinge lengths for Case 2 of MUMPS

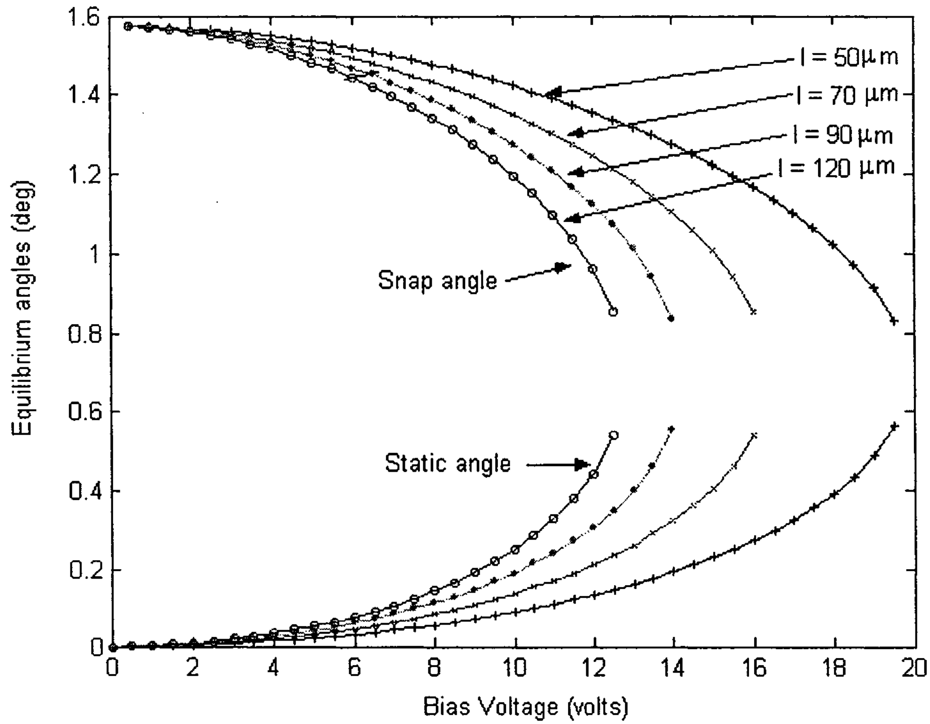

Fig. 2.17 (c) Equilibrium angles determining the pull-in voltage for different hinge lengths for Case 2 of MUMPS

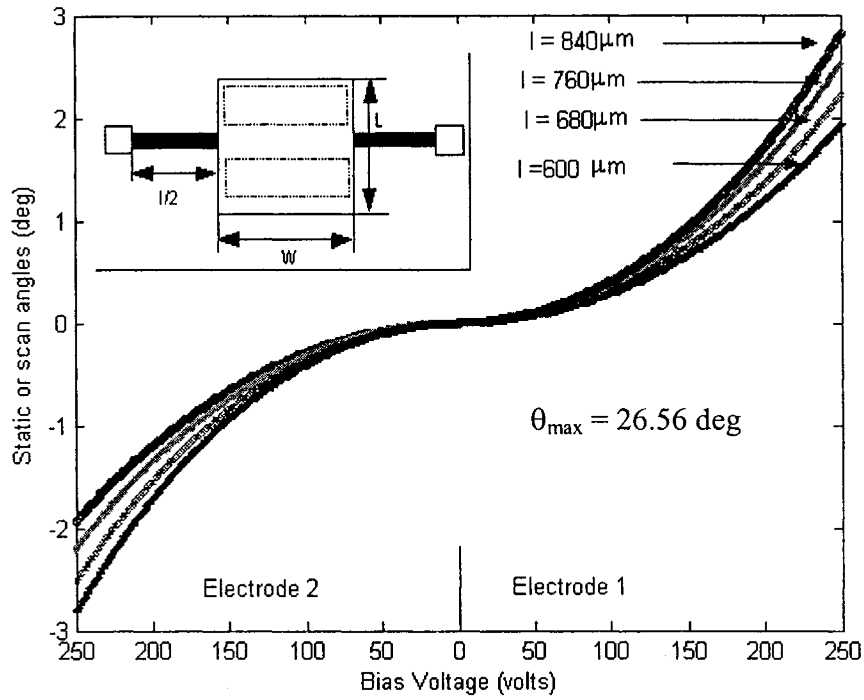

Fig. 2.18 (a) Tilting or scan angles for L = 500μm and W = 500μm of mirror dimensions (Case 1) of SOI based bulk micromachining for different bias voltages

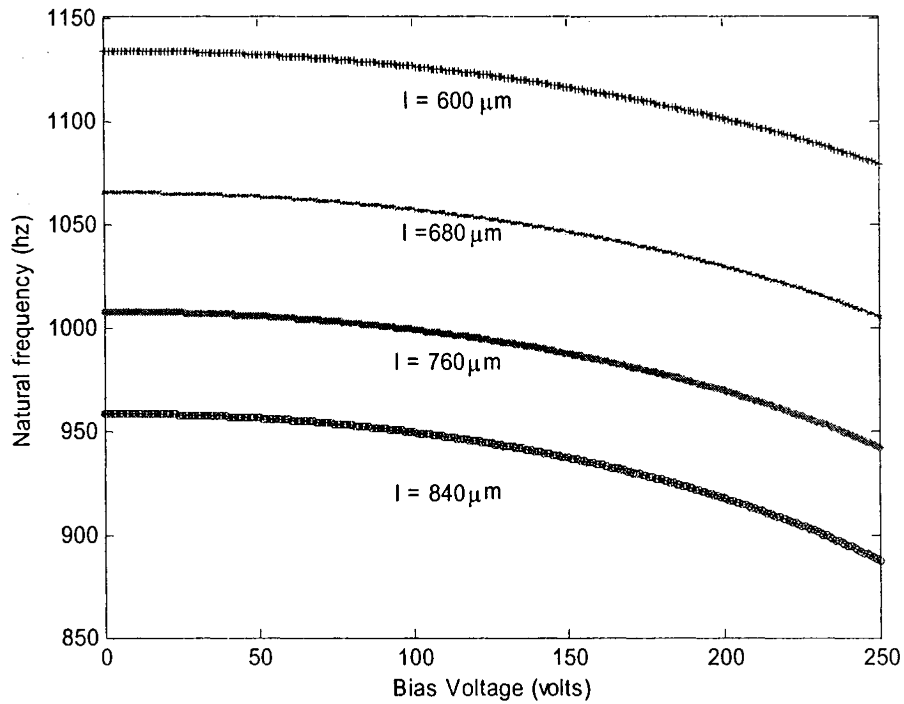

Fig. 2.18 (b) Variation of frequency with bias voltage for different hinge lengths for Case 1 of SOI based bulk micromachining

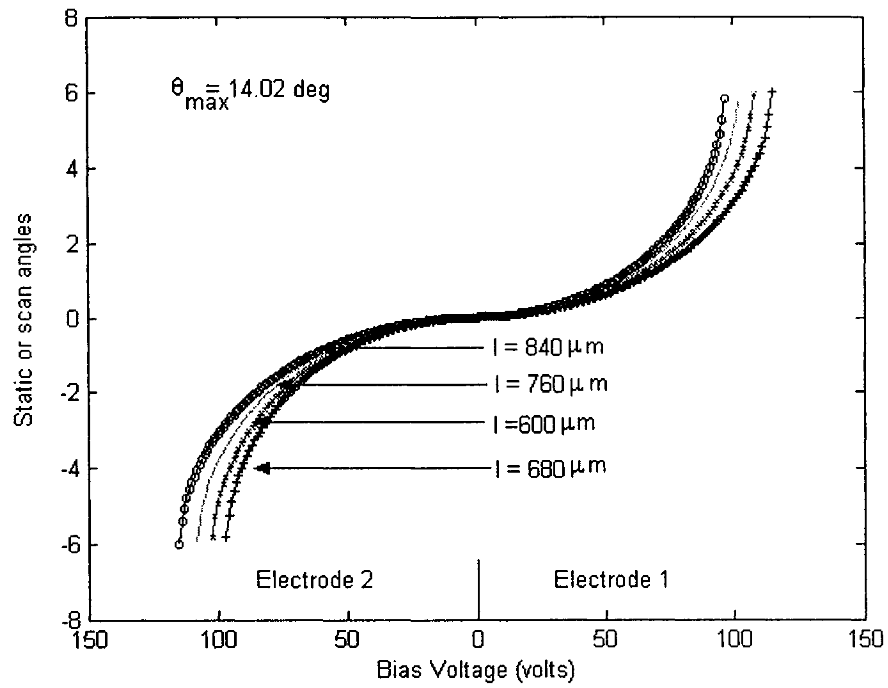

Fig. 2.19 (a) Tilting or scan angles for L = 1000μm and W = 1000μm of mirror dimensions (Case 2) of SOI based bulk micromachining for different bias voltages

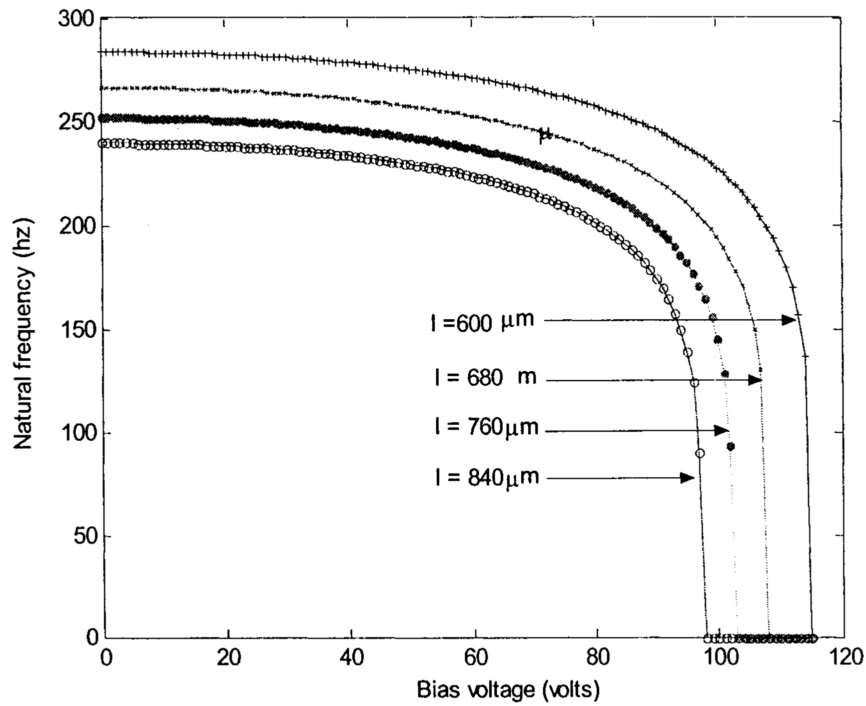

Fig. 2.19 (b) Variation of frequency with bias voltage for different hinge lengths for Case 2 of SOI based bulk micromachining

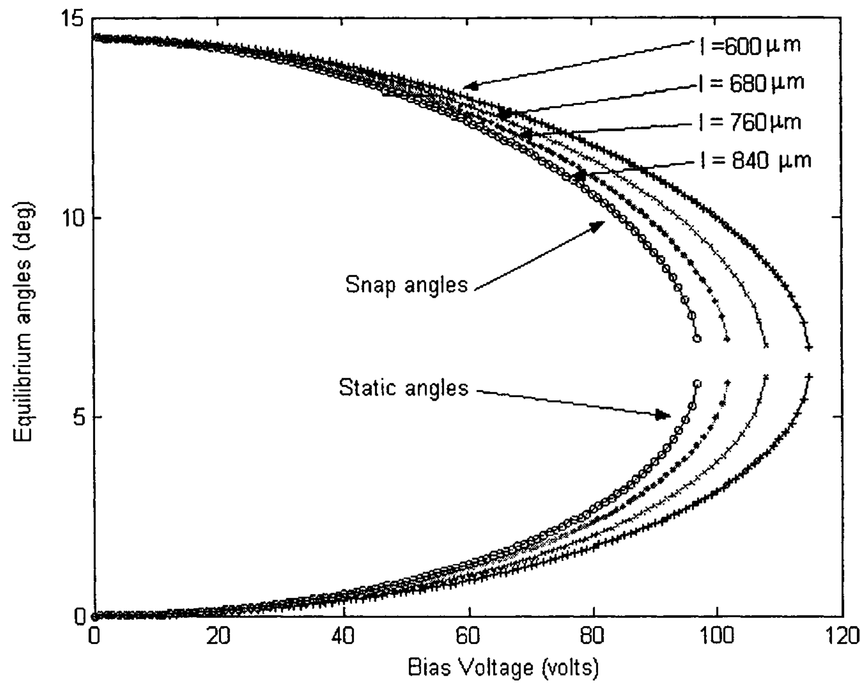

Fig. 2.19 (c) Equilibrium angles determining the pull-in voltage for different hinge lengths for Case 2 of SOI based bulk micromachining

2.4 Conclusions

In this chapter an improved model to study the switching response of torisonal micromirrors is presented. It was demonstrated that the counter electrostatic fields and that due to stopper electrode influence the equilibrium scan angle and natural frequency significantly for a stopper of sufficient height which is quite effective in increasing the tilting capability of the micromirror. The model proposed in this work will be useful in studying the performance of torsional micromirrors subjected to large tilting angles. Also the scanning micromirrors were analyzed for static angles and natural frequency considering two different types of microfabrication technologies. Different designs were considered and analyzed based on MUMPS and SOI technologies. The

limitation with gap between the electrodes in MUMPS becomes the limiting factor in determining the maximum tilt angle. The bulk micromachining of mirrors in SOI technology indicates the possibilities of attaining large tilt angles. The numerical exercise with different design geometries for MUMPS and SOI technologies show the feasibility of obtaining large tilt angles with SOI wafers. The influence of electrostatic field on both static and dynamic behavior of optical MOEMS devices such as micromirrors, scanning mirrors has been studied. If possible a common methodology for modeling the dynamic behavior of electrostatically actuated MEMS devices will be very useful for the design of microsystems.

Chapter – 3

Boundary conditioning of electrostatically operated devices

3.1 Introduction

Electrostatically operated optical MEMS devices find application in many areas including adaptive optics, switching, attenuation, scanning, display, contact type atomic microscope, etc. The presence of electrostatic field in these devices influences static, and dynamic response behavior of these devices. The response of the device can be estimated using the fundamental vibration modes of the system based on the normal mode approach. But, presently the vibration modes of the electrostatically operated devices are estimated based on nodes under no voltage condition. Hence, any attempt to model the influence of electrostatic field on vibrational behavior becomes essential.

This chapter attempts to model the influence of electrostatic field on vibrational behavior of microstructures using the concept of boundary conditioning [59]. Even though the final results depend upon the configuration or geometry of the MEMS structures, this chapter only demonstrates the proposed concept using a simple rectangular type structures that has many applications in adaptive optics, interferometry, etc. The proposed method can be easily extended to other type MEMS devices.

3.1.1 Introduction to boundary conditioning

As seen in the previous paragraphs, the estimation of the dynamic behavior such as the natural frequency and mode shapes of microdevices is important as it determines the performance of microsystem [75]. The dynamic behavior is dependent on the mass and stiffness properties of the system. The stiffness of an elastic system is dependent on the structural geometry, support conditions, fabrication process and operational environment including electrostatic field [59-62, 76-78]. Hence any structural modification such as stiffening, notching, affect the dynamic behavior of elastic systems. The fabrication procedures employed for microsystems lead to different end support conditions that are non-classical in nature and are intermediate between pinned and clamped conditions. External influences such as squeeze film damping, electrostatic field, Lorentz force also affect the dynamic performance of the system. A method to quantify the above effects will be very useful in designing and modeling the dynamic performance of the system. The manipulation of dynamic behavior such as eigenvalues and mode shapes by suitably modifying the structural or environmentally influenced part of the elastic property of the system is defined as the boundary conditioning [59]. Rangsten et al. [79] added notches at the end supports of diaphragm of an electrostatically excited loudspeaker in order to weaken the stiffness of the diaphragm and to have larger deflections. Muthukumaran et al. [59-62] used boundary conditioning concept to quantify the end support conditions by using artificial springs on all edges of microplates for obtaining the dynamic performance. The artificial springs used were translational and rotational springs. The stiffness values of the translational and rotational springs can be adjusted to represent any boundary condition desired or

microfabricated. As the concept of boundary conditioning can model the structural and environmental influence in a unified way, it is used here in modeling the influence of electrostatic field.

3.1.2 Boundary characteristic orthogonal polynomials

Bhat [80] presented a novel way to obtain the natural frequencies of rectangular plates under various boundary conditions using boundary characteristic orthogonal polynomials in the Rayleigh Ritz method. These orthogonal polynomials were generated using Gram-Schmidt process. The first polynomial is chosen so that it satisfies at least the geometrical boundary conditions of the structure for use in the Rayleigh-Ritz method. The example given below elaborates the construction of orthogonal polynomials for a fully clamped (CCCC) plate whose boundary conditions are zero deflections and also zero slopes at boundaries.

For a rectangular plate, the deflection may be assumed as

$W(x, y) = X(x)\,Y(y)$

The boundary conditions corresponding to a fully clamped plate are:

$$X(0) = X'(0) = X(a) = X'(a) = 0 \qquad 3.1$$

Assuming a deflection function in the x direction as

$$X(x) = a_0 + a_1 x + a_2 x^2 + a_3 x^3 + \dots\dots\dots + a_n x^n \qquad 3.2$$

Applying (3.1) in (3.2) the first normalized polynomial is obtained as

$$\phi_0(x) = \left(x^2 - 2x^3 + x^4\right) / \left(\int_a^b X^2(x)\right)^{1/2} dx \qquad 3.3$$

The second orthogonal polynomial is obtained in the interval $a \le x \le b$

$$\phi_1(x) = (x - B_1)\phi_o(x) \tag{3.4}$$

or in general

$$\phi_k(x) = (x - B_k)\phi_{k-1}(x) - C_k\phi_{k-2}(x) \tag{3.5}$$

where

$$B_k = \frac{\int_a^b x f(x)\phi_{k-1}^2(x)dx}{\int_a^b f(x)\phi_{k-1}^2(x)dx} \tag{3.6}$$

$$C_k = \frac{\int_a^b x f(x)\phi_{k-1}(x)\phi_{k-2}(x)dx}{\int_a^b f(x)\phi_{k-2}^2(x)dx} \tag{3.7}$$

The polynomials thus obtained satisfy the orthogonality condition

$$\int_a^b f(x)\phi_k(x)\phi_l(x)dx = \begin{cases} 0 & \text{if } k \ne l \\ a_{kl} & \text{if } k = l \end{cases} \tag{3.8}$$

where f(x) is the weight function. Similar orthogonal polynomials along the y direction may be constructed following the above procedures.

In this chapter the plate type micromirror, boundary conditioned with external electrostatic field, has been analyzed for its dynamic performance using boundary characteristic orthogonal polynomials in the Rayleigh-Ritz method for different end support conditions, namely, clamped (CCCC), simply supported (SSSS) and microfabricated condition (MMMM) that lies between the CCCC and SSSS conditions. A formulation to obtain the static deflection of the micromirrors is presented. Further, the vibration problem is formulated at the static equilibrium condition by including an

elastic foundation stiffness to represent the electrostatic field effects in order to obtain the modeshapes and the eignevalues of the micromirror at the static equilibrium position. The microplate used in the formulation is assumed to represent micromirrors, in general.

3.2 Modeling of micromirrors using artificial springs

Figure 3.1 shows the micromirror supported by translational and rotational springs with stiffness values 'K_T' and 'K_R' per unit length at the end supports as shown. The micromirror is the main electrode which is separated by a gap of 'd' from the substrate that acts as the bottom electrode. For its simplicity, the electrostatic actuation is used to actuate the above mentioned type of devices [13, 31].

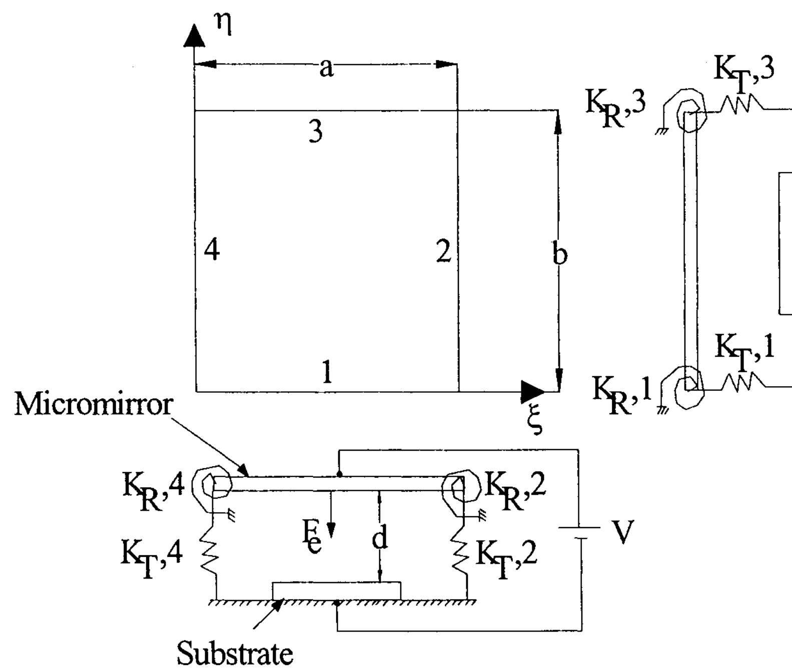

Fig. 3.1 Structural scheme of boundary conditioning

When a bias voltage 'V' is applied between the micromirror and the substrate, electrostatic field is created and it results in attractive electrostatic force that pulls the mirror towards the substrate.

The concept of boundary conditioning is explained by considering a lumped model as shown in Figure 3.2. The model is represented by equivalent mass 'M' supported by two springs as shown. 'K_{struc}' is the stiffness representing the elastic property of the structural part of the system. 'K_{ext}' is the stiffness representing the external influence such as support conditions and environmental influence. In the present work, the environmental influence is the electrostatic field between the mirror and the substrate.

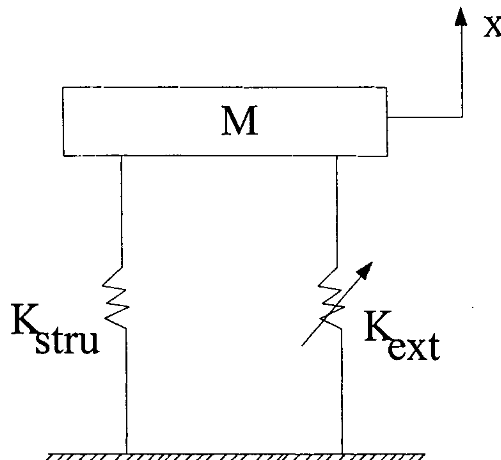

Fig. 3.2 Lumped model of an elastic system with boundary conditioning.

This electrostatic field has a softening effect on the elastic property of the system, affecting the dynamic behavior of the micromirror. In order to apply the concept of boundary conditioning to represent the electrostatic effect, quantification of the softening effect in terms of distributed springs with stiffness per unit area of 'K_e' is introduced. As

the deflection increases due to increase in voltage, the value of the stiffness 'K_e' will indicate more weakening. Hence, the electrostatic field is assumed to result in non-uniform distributed spring with stiffness per unit area of $K_e(x, y)$. It is known that a constant value of the stiffness $K_e(x, y)$ would result in different natural frequencies but same modeshapes when compared to the micromirror without elastic foundation. As the deflection of the micromirror due to electrostatic force results in non-uniform spacing between the electrodes, it results in softening elastic foundation with non-uniform variation of $K_e(x, y)$ as shown in Figure 3.3.

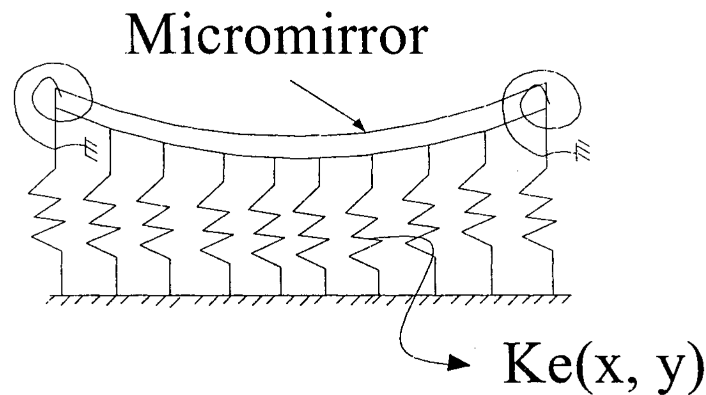

Fig. 3.3 Electrostatic field modeled as springs

Thus the present quantification of the electrostatic influence in terms of weakening spring stiffness values will enable the application of boundary conditioning concept to model the dynamic behavior of microsystem under the influence of electrostatic field. The rotational and translational stiffness values can be changed suitably to quantify the boundary conditions such as SSSS, CCCC and MMMM. The formulation to estimate the static deflections of the micromirror is shown below. At the

static deflection position the electrostatic potential energy is obtained by considering the elastic foundation stiffness 'K_e' which is a function of the static deflection of the plate.

3.2.1 Static behavior

The micromirror can be considered as a rectangular plate. The flexural deflection of the micromirror is assumed as

$$W_s(x,y) = \sum_m \sum_n A^s_{mn} \phi_m(x) \varphi_n(y) \qquad 3.9$$

where, $x = \frac{\xi}{a}$, $y = \frac{\eta}{b}$

ξ and η are physical coordinates the of the plate,

'a' and 'b' are dimensions of the plate with $\alpha = \frac{a}{b}$,

A^s_{mn} are the deflection coefficients of each term describing the mirror static deflection in Equation 3.9. Further

$\phi_m(x)$ and $\varphi_n(y)$ are boundary characteristic orthogonal polynomials in respective directions.

As explained in Chapter 2, the micromirror attains a static equilibrium condition when the mechanical force is equal to the electrostatic force. This position is obtained using the equation,

$$\frac{\partial U_{net}(A^s_{mn})}{\partial A^s_{mn}} = 0 \qquad 3.10$$

where, U_{net} is the total energy given by,

$$U_{net} = U_{max,p} + \sum_{s=1}^{4} U_{T,s} + \sum_{s=1}^{4} U_{R,s} + U_e \qquad 3.11$$

where, $U_{max,p}$ is the strain energy of the micromirror as a rectangular plate

$$U_{max,p} = \frac{D\ a\ b}{2a^4} \int_0^1\int_0^1 \left[W_s''^2 + \alpha^4\ \ddot{W}_s^{\,2} + 2\upsilon \cdot \alpha^2 \cdot W_s'' \ddot{W}_s + 2(1-\upsilon)\alpha^2\ \dot{W}_s'^{\,2} \right] dxdy \qquad 3.11a$$

$U_{T,s}$ is the strain energy of the translational springs along the side 's' and $U_{R,s}$ is the strain energy of the rotational springs along the side 's', as given by

$$U_{T,s} = \frac{1}{2} K_{T,s} \int_0^{l_s} W_{s,s}^2 dl_s \qquad 3.11b$$

$$U_{R,s} = \frac{1}{2} K_{R,s} \int_0^{l_s} W_{s,s}'^2 dl_s \qquad 3.11c$$

where, 'l_s' is the length of the side's', $K_{T,s}$ is the translational stiffness per unit length along the side 's' per unit length. $K_{R,s}$ is the rotational stiffness per unit length along the side 's'. $W_{s,s}$ is the static deflection along side 's'. $W_{s,s}'$ is the slope along the side 's'.

U_e is the strain energy due to the electrostatic field between the main electrode and the bottom electrode and is defined as,

$$U_e = -\frac{\varepsilon_o \varepsilon_r ab V^2}{2} \int_0^1\int_0^1 \frac{dx\,dy}{(d - W_s(x,y))} \qquad 3.12$$

where, ε_o and ε_r are the permittivity of free space and relative permittivity of the dielectric medium, respectively. Relative permittivity is assumed as one in this case.

Equation 3.12 can be expanded using Taylor's series as below

$$U_e = -\frac{\varepsilon_o \varepsilon_r abV^2}{2d} \int_0^1\int_0^1 \left[1 + \frac{W_s(x,y)}{d} + \left(\frac{W_s(x,y)}{d}\right)^2 + ... \right] dx \ dy \qquad 3.12a$$

Substitution of deflection equation 3.9 in energy expression 3.11 and optimization with respect to A^s_{mn} in equation 3.10 result in the following equation:

$$\sum_m \sum_n \left[C_{mnij} + C^I_{mnij} + \beta_1^* \cdot E^{00}_{mi} F^{00}_{nj} \right] A^s_{mn} = \beta^* \int_0^1\int_0^1 \phi_i(x) \ \varphi_j(y) \, dx \, dy \qquad 3.13$$

where

$$C_{mnij} = E^{22}_{mi} F^{00}_{nj} + \alpha^4 E^{00}_{mi} F^{22}_{nj} + \upsilon \cdot \alpha^2 \left(E^{02}_{mi} F^{20}_{nj} + E^{20}_{mi} F^{02}_{nj} \right) + 2 \cdot (1-\upsilon) \alpha^2 E^{11}_{mi} F^{11}_{nj} \qquad 3.13a$$

$$C^I_{mnij} = K^*_{T,1} \alpha \ E^{00}_{mi} \varphi_n(0) \varphi_j(0) + K^*_{T,2} \phi_m(1) \phi_i(1) F^{00}_{nj} + K^*_{T,3} \alpha \ E^{00}_{mi} \varphi_n(1) \varphi_j(1) + \qquad 3.13b$$

$$K^*_{T,4} \phi_m(0) \phi_i(0) F^{00}_{nj} + K^*_{R,1} \alpha^3 E^{00}_{mi} \varphi^1_n(0) \varphi^1_j(0) + K^*_{R,2} \phi^1_m(1) \phi^1_i(1) F^{00}_{nj} +$$

$$K^*_{R,3} \alpha^3 E^{00}_{mi} \varphi^1_n(1) \varphi^1_j(1) + K^*_{R,4} \phi^1_m(0) \phi^1_i(0) F^{00}_{nj}$$

$\beta^* = \dfrac{\varepsilon_o \varepsilon_r V^2 a^4}{2Dd^2}$, $\beta_1^* = -\dfrac{\varepsilon_o \varepsilon_r V^2 a^4}{Dd^3}$, 'D' is the flexural rigidity of the plate.

Normalized translational stiffness, $K^*_{T,i} = \dfrac{K_{T,i} a^3}{D}$, Normalized rotational stiffness $K^*_{R,i} = \dfrac{K_{R,i} a}{D}$, $E^{rs}_{mi} = \displaystyle\int_0^1 \left(\frac{d^r \phi_m}{dx^r} \right) \left(\frac{d^s \phi_i}{dx^s} \right) \cdot dx$, $F^{rs}_{nj} = \displaystyle\int_0^1 \left(\frac{d^r \varphi_n}{dy^r} \right) \left(\frac{d^s \varphi_j}{dy^s} \right) \cdot dy$,

$\phi^1_i = \dfrac{d\phi_i}{dx}$, $\varphi^1_j = \dfrac{d\varphi_j}{dy}$

For demonstrating the above modeling, consider a micromirror with the following dimensions:

$a = 600$ μm, $b = 600$ μm, $t = 2$ μm, $d = 15$ μm, $E = 179$Gpa, $\gamma = 0.3$. The static deflection has been estimated by solving the equation 3.13 for different bias voltages V and end support conditions, namely, CCCC, SSSS and MMMM.

For modeling purpose, the condition of $K^*_{T,i} = 0$ and $K^*_{R,i} = 0$ corresponds to free edge condition, $K^*_{R,i} = 0$ and very high values of $K^*_{T,i}$ correspond to simply supported condition while very high values of both $K^*_{T,i}$ and $K^*_{R,i}$ correspond to clamped condition. In this work, three types of end support conditions were quantified using translational and rotational spring stiffness values. For CCCC condition the value of both $K^*_{T,i}$ and $K^*_{R,i}$ were taken as 1×10^{10}. In case of SSSS boundary condition the $K^*_{R,i}$ value is made zero while keeping the value for $K^*_{T,i}$ as 1×10^{10}. For MMMM end support condition which lies between the CCCC and SSSS condition, a value of 1×10^{10} is assumed for $K^*_{T,i}$, and due to the microfabrication limitations, a value of 12 is assumed for $K^*_{R,i}$ as suggested in a previous paper [81]. In the present analysis twelve orthogonal polynomials were used in each direction. The predicted results are given in the following figures.

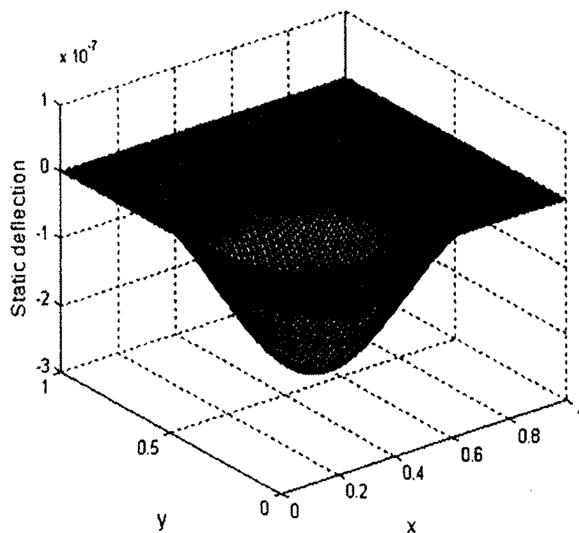

Fig. 3.4 Static deflection in μm of mirror as a square plate for CCCC condition at V=100volts

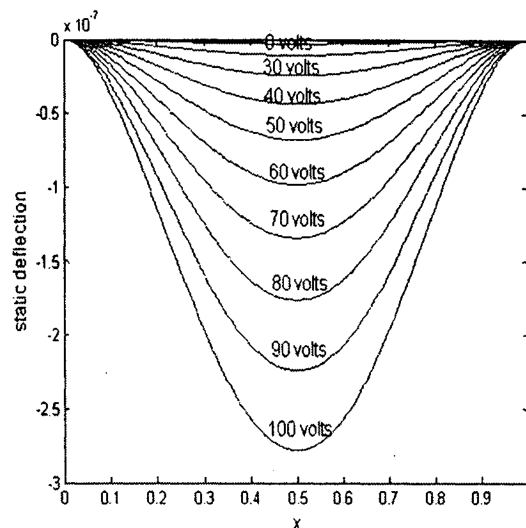

Fig. 3.4a Static deflection in μm of micromirror at y=0.5 for CCCC at different voltages.

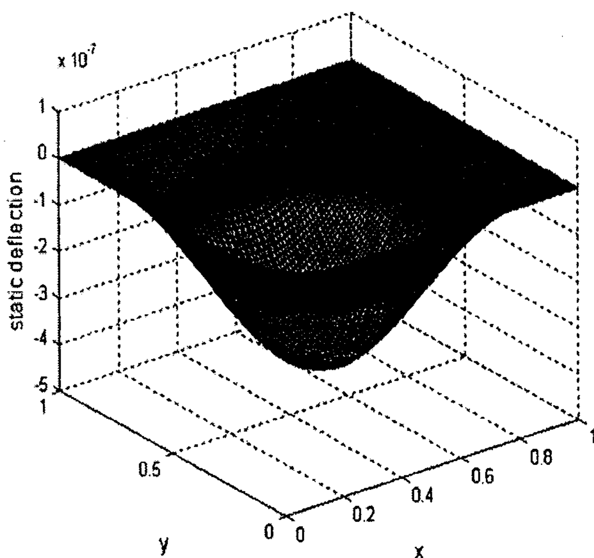

Fig. 3.5 Static deflection in μm of mirror as a square plate for MMMM condition at V=100volts

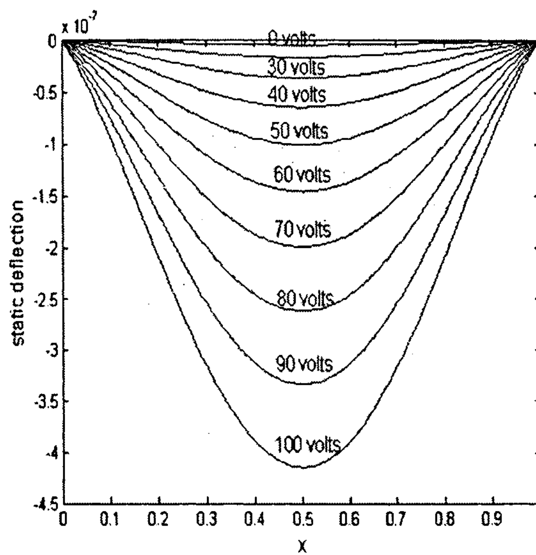

Fig. 3.5a Static deflection in μm of micromirror at y=0.5 for MMMM at different voltages.

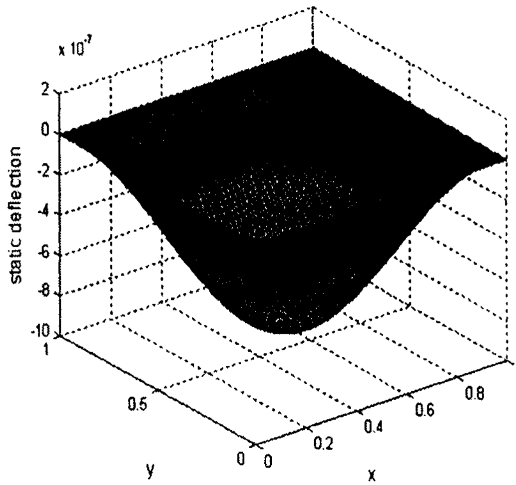

Fig. 3.6 Static deflection of mirror as a square plate for SSSS condition at V=100volts

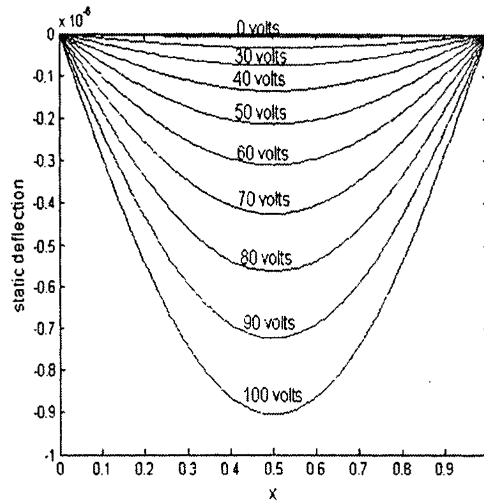

Fig. 3.6a Static deflection of micromirror at y=0.5 for SSSS at different voltages.

Figures 3.4, 3.4a, 3.5, 3.5a, 3.6, 3.6a provide the plot of static deflection of micromirror under CCCC, MMMM and SSSS support conditions. Figures 3.4a, 3.5a and 3.6a are the cross- sectional views of Figures 3.4, 3.5 and 3.6, respectively, which present the maximum static deflection micromirror occurring at y=0.5, for different voltages. It can be seen from these figures that as the voltage is increased, deflection of the micromirror is also increased which will lead to varying elastic foundation stiffness due to the electrostatic field. The electrostatic elastic stiffness value $K_e(x, y)$ is estimated at the static equilibrium condition in order to represent the boundary conditioning.

3.2.2 Dynamic behavior

At the static equilibrium condition, the varying elastic foundation stiffness value '$K_e(x, y)$' is introduced to estimate the dynamic behavior. The deflection function considering the dynamic deflection co-efficients 'D_{mn}' is given by the equation

$$W_d(x, y) = \sum_m \sum_n D_{mn} \phi_m(x) \varphi_n(y) \tag{3.14}$$

'U_{el}', the electrostatic potential energy after considering elastic foundation stiffness 'K_e' is given by equation

$$U_{el} = -\frac{1}{2} \int_0^1 \int_0^1 K_e(x, y) (W_d(x, y))^2 \, dxdy \tag{3.15}$$

where,

$$K_e(x, y) = \frac{d^2 U_e}{dW_s^2} = -\frac{\varepsilon_o \varepsilon_r V^2 ab}{(d - W_s(x, y))^3} \tag{3.15a}$$

The value of $K_e(x, y)$ represents the boundary conditioning due to the electrostatic field. In order to estimate the strain energy, strain energies due to plate bending, end springs and electrostatic springs are needed. The strain energy of the mirror as a plate due to bending is given by equation 3.11a and that due to the springs is given by equations 3.11b and 3.11c. In the above equations W_s is replaced with W_d. Then, the total strain energy becomes,

$$U_{net} = U_{max,p} + \sum_{s=1}^{4} U_{T,s} + \sum_{s=1}^{4} U_{R,s} + U_{el} \tag{3.16}$$

Similarly the kinetic energy of the micromirror is given by the expression

$$T_{max} = \frac{1}{2}\rho hab\omega^2 \int_0^1\int_0^1 W_d^{\,2}(x,y)dxdy \qquad 3.17$$

where, 'ρ' is the mass density of the micromirror, 'ω' is the natural frequency of the micromirror and 'h' is the thickness of the micromirror. From Rayleigh's condition $T_{max} = U_{net}$ the Rayleigh's quotient can be obtained as

$$\omega^2 = \frac{U_{net}}{T^*_{max}} \qquad 3.18$$

where,

$\omega^2 T^*_{max} = T_{max}$

After the substitution of deflection function in equation 3.14 in 3.16 and 3.17, and optimization of Rayleigh's quotient of equation 3.18 with respect to arbitrary constants 'D_{mn}', the eigenvalue problem is formulated as given below:

$$\sum_m\sum_n \left[\left(C_{mnij} + C^I_{mnij} + \beta_2^* G^{00}_{mnij}\right) - \lambda \cdot E^{00}_{mi} F^{00}_{nj}\right] D_{mn} = 0 \qquad 3.19$$

where,

$$G^{00}_{mnij} = \int_0^1\int_0^1 \frac{\phi_m(x)\phi_i(x)\varphi_n(y)\varphi_j(y)}{(d-(W_s(x,y)))^3}dx\,dy \qquad 3.19a$$

$\beta_2^* = -\dfrac{\varepsilon_o \varepsilon_r V^2 a^4}{D}$ and $\lambda = \dfrac{\rho\, h\, a^4 \omega^2}{D}$, C_{mnij} and C'_{mnij} are given by equations 3.13a and 3.13b after substituting $W_d(x,y)$ for $W_s(x,y)$.

The solution of equation 3.19 gives eigenvalues and modeshapes under the influence of electrostatic field. The deflection coefficients D_{mn} obtained from equation 3.19 are substituted in equation 3.14 to get the corresponding modeshapes.

3.2.3 Results and Discussion

Response of an electrostatically operated structure depends also on translational and rotational stiffness values at the supports. The vibrational behavior of a system, such as, modeshapes, natural frequencies and response can be modified by suitably altering the stiffness values of the springs. This was demonstrated effectively earlier [59]. However, in the present work it has been shown that the modeshapes and the frequencies are affected also by the external environment of the system. In this case, it is the electrostatic field around mirror. The electrostatic field is also quantified by equivalent softening springs as shown in the equations earlier. For the present work, the dimensions of the micromirror are 600μm in length and breadth for a constant electrode gap of 15μm. Figure 3.7 shows the variation between 'V' and eigenvalue of the first mode for increasing voltage.

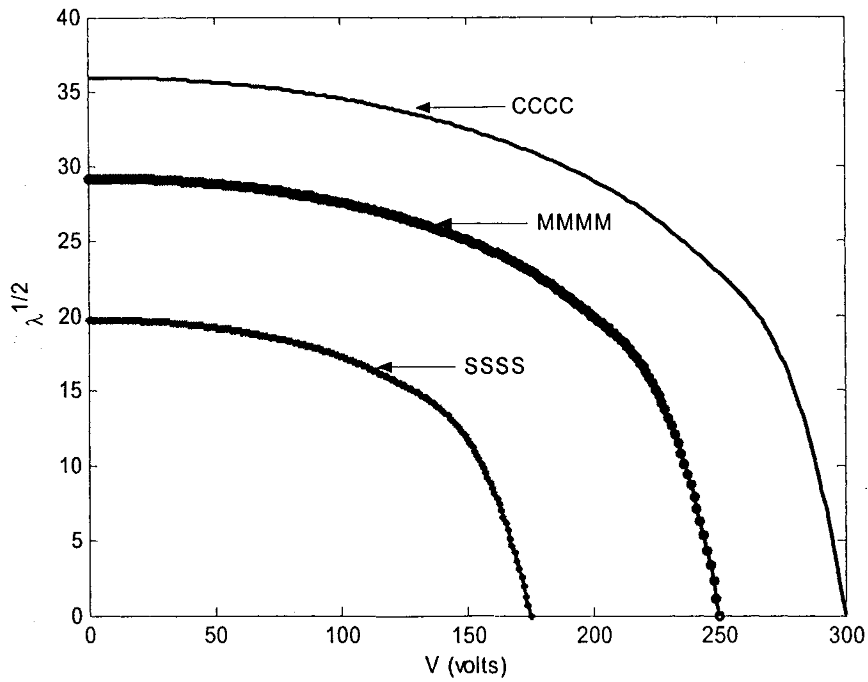

Fig. 3.7 A plot of voltage and frequency parameter for the three end conditions

Eigenvalue for each support condition reaches zero for a certain snap voltage as shown in Figure 3.7. The graph indicates that the snap voltage of the square microplate for MMMM condition lies between the CCCC and SSSS condition. The pull-in of the micromirror roughly occurs when the micromirror reaches 1/3 of the gap between the two electrodes.

Using this snap voltage as a basis, the micromirror has been analysed using a normalized voltage parameter defined as,

$$\sigma = \left(\frac{V}{V_{snap}} \right) \times 100\% \qquad 3.20$$

where, 'V_{snap}' is the pull-in voltage for the corresponding end condition and 'V' is the applied voltage. This normalized parameter is used to study the effect of electrostatic field on the modeshapes and natural frequencies of the micromirror.

Table 3.1 provides the voltages considering different 'σ' values for the end support conditions used in this work. The factor 'σ' is considered in such a way that it represents the range of voltages starting from 0 and ending at a value very close to the snap voltage. Table 3.2 tabulates eigenvalues obtained for the respective support conditions at the respective voltages. The microfabricated condition clearly lie between the CCCC and the SSSS condition. As the voltage is increased the eigenvalue decreases. However there is a maximum change in eigenvalues in the fundamental mode when compared to other modes. Figure 3.8 and Figure 3.8a show the first modeshape and cross sectional view of the first modeshape of a CCCC support conditioned micromirror, respectively. The second and third modeshapes are shown in Figure 3.9 and 3.10 while their sectional views are shown in Figures 3.9a and 3.10a for CCCC condition. The modeshapes shown in Figure 3.8a, 3.9a and 3.10a are normalized with respect to maximum amplitude so that the shapes can be compared for different voltages. The Figure 3.8a shows that fundamental modeshape is largely affected by the electrostatic field while higher modes 2 and 3 show no significant effects. Similarly, Figures 3.11, 3.11a, 3.14, and 3.14a show the first modeshape and cross sectional view of the first normalized modeshape for a mirror with MMMM and SSSS conditions, respectively. It can be seen from Figures 3.11a and 3.14a that the fundamental modeshape changes with change in 'σ' value. Figure 3.12 and Figure 3.13 show the second and the third

modeshapes for MMMM condition and Figures 3.15 and 3.16 show the second and third modeshapes for SSSS condition. The Figures 3.12a and 3.13a show that electrostatic field does not influence significantly the higher modeshape for MMMM condition while Figures 3.15a and 3.16a show similar results for SSSS condition. The modeshapes are normalized with respect to the maximum amplitude for all 'σ' values as seen in these figures. However it can be seen from the above figures that there is a considerable weakening in elastic property of the micromirror due to increase in voltage which influences significantly the modeshapes.

Support condition	V_{snap}	σ				
		0	20%	50%	80%	96%
CCCC	300	0	60	151	241	289
MMMM	250	0	50	125	200	240
SSSS	175	0	35	87	140	168

Table 3.1 Voltages for different 'σ' values

End support conditions		$\sqrt{\lambda}$ (mode)			
CCCC		(1)	(2)	(3)	(4)
V(volts)	0	36.0084	73.4293	73.4293	108.2854
	60	35.4840	73.1223	73.1223	108.1369
	151	32.4094	71.3612	71.3612	107.2838
	241	23.9310	67.3535	67.3535	105.4402
	289	10.0832	63.4656	63.4656	103.7857
MMMM					
V(volts)	0	29.2208	61.3154	61.3154	92.1298
	50	28.8263	61.0787	61.0787	92.0136
	125	26.4558	59.7315	59.7315	89.9328
	200	19.7231	56.5846	56.5846	89.9328
	240	8.5844	53.4495	53.4495	88.6182
SSSS					
V(volts)	0	19.7392	49.3480	49.3480	78.9568
	35	19.4799	49.2108	49.2108	78.8927
	87	17.9407	48.4389	48.4389	78.5376
	140	13.4189	46.3775	46.3775	77.7229
	168	5.7612	44.7013	44.7013	76.9599

Table 3.2 $\sqrt{\lambda}$ values for first four modes

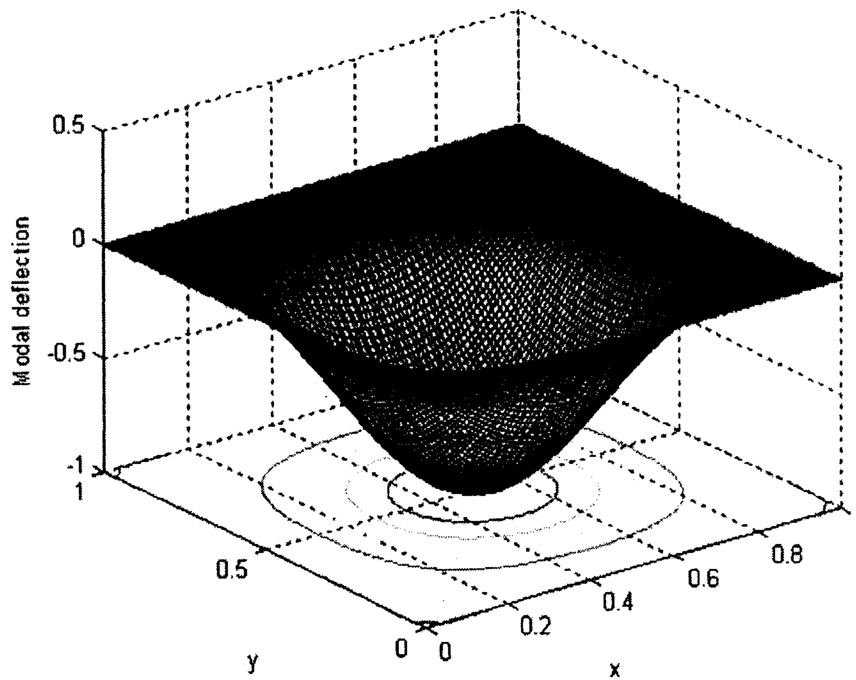

Fig. 3.8 First modeshape for CCCC condition of micromirror

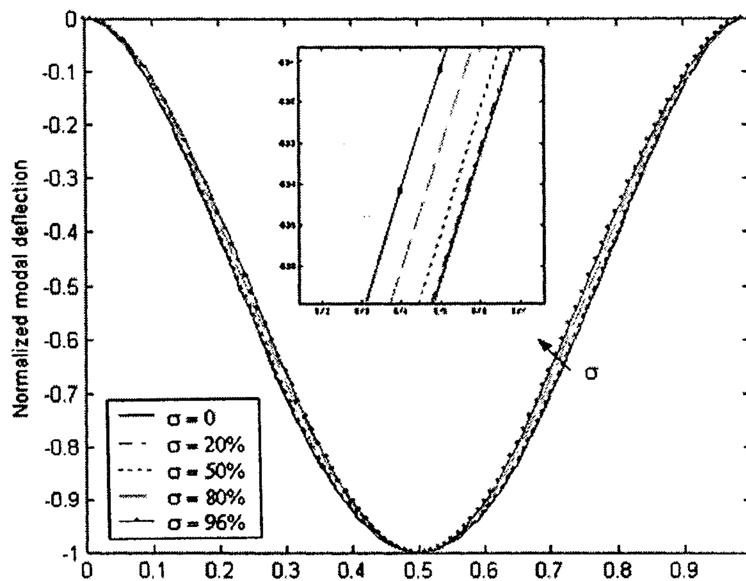

Fig. 3.8a Plot of 1st mode for CCCC condition at y =0.5

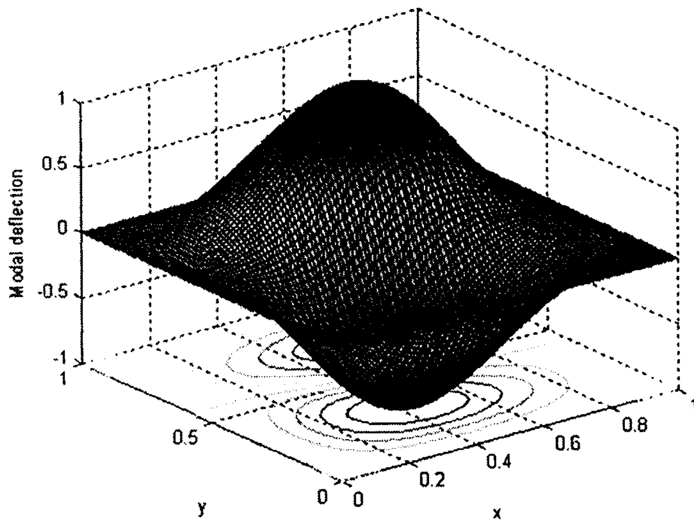

Fig. 3.9 Second modeshape for CCCC condition of micromirror

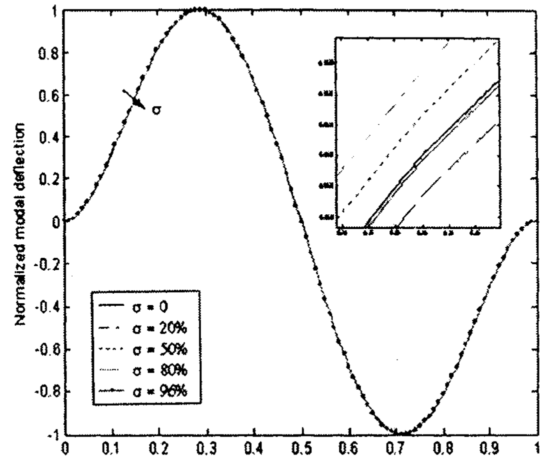

Fig. 3.9a Plot of 2nd mode for CCCC condition at y = 0.5

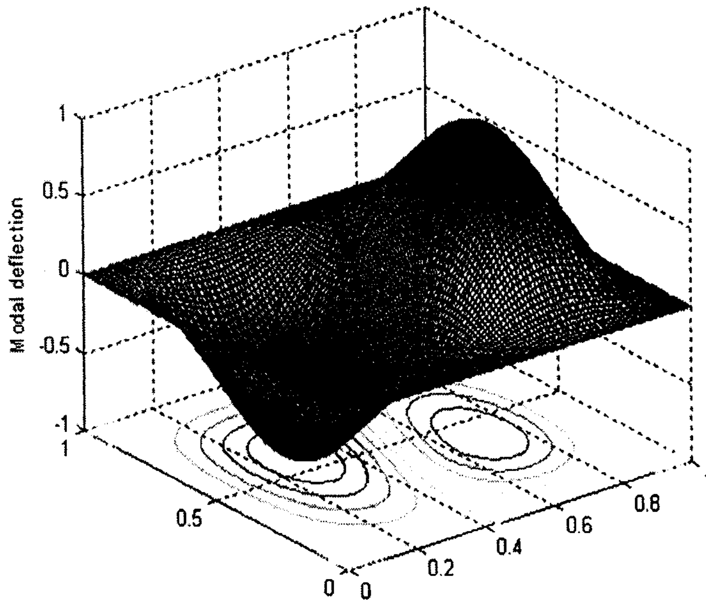

Fig. 3.10 Third modeshape for CCCC condition of micromirror

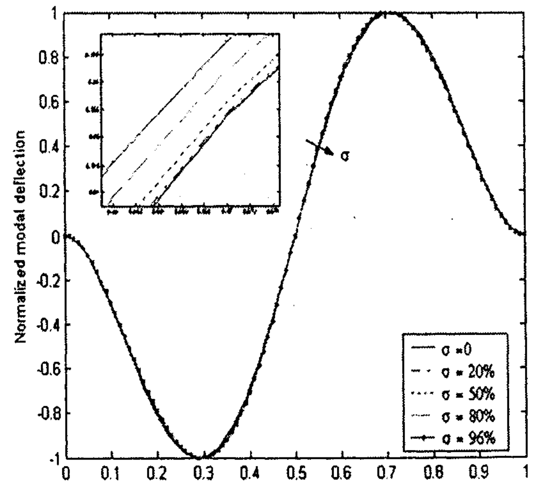

Fig. 3.10a Plot of 3rd mode for CCCC condition at y = 0.5

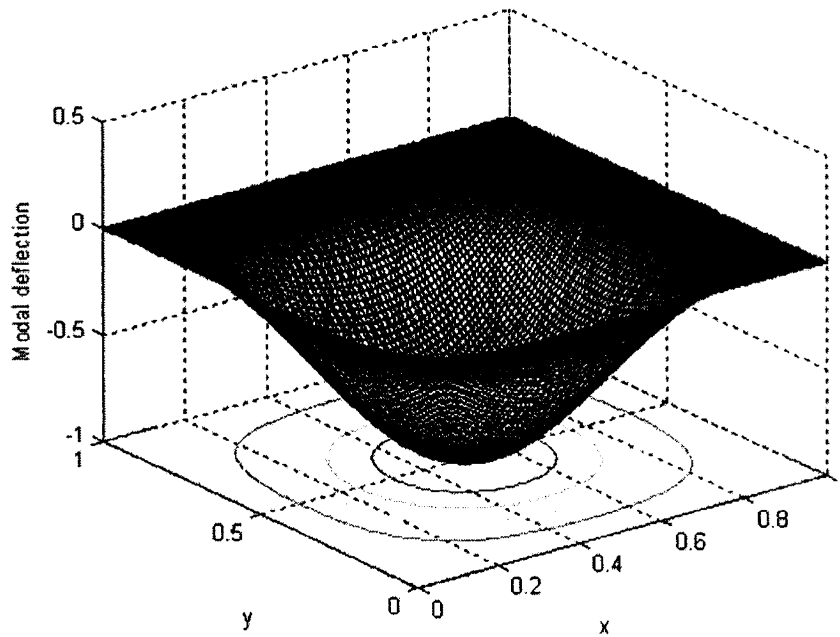

Fig. 3.11 First modeshape for MMMM condition of micromirror

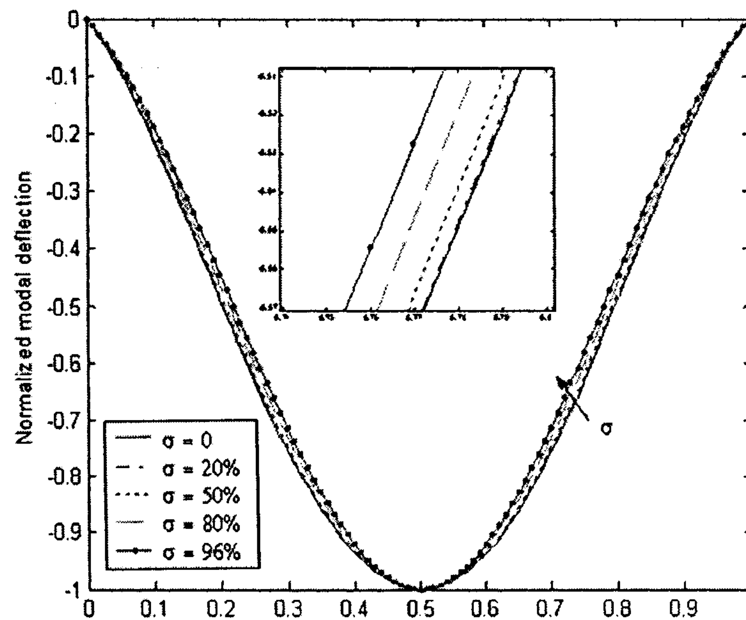

Fig. 3.11a Plot of 1st mode for MMMM condition at y = 0.5

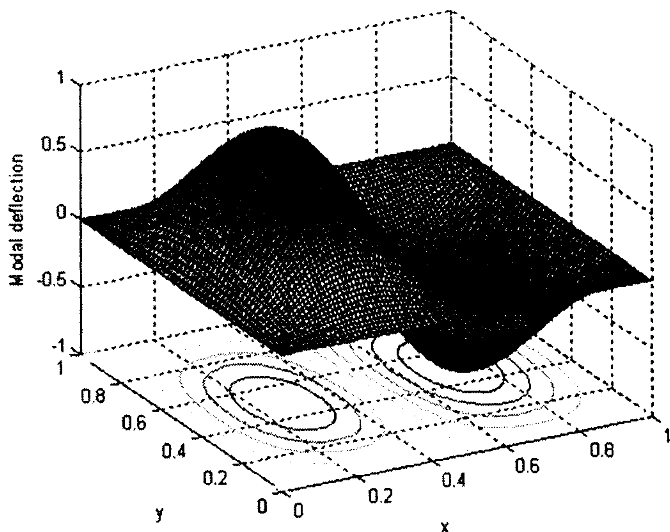

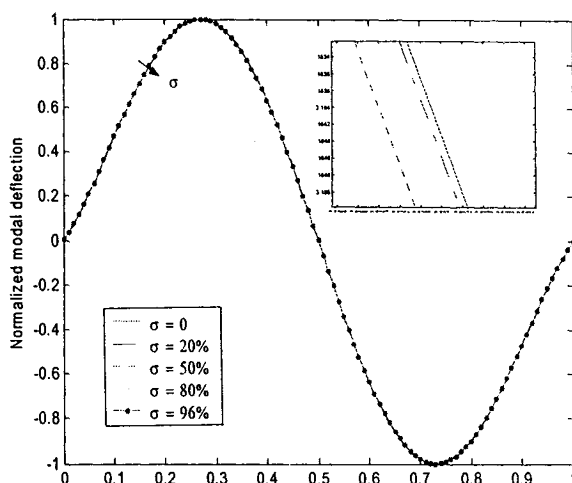

Fig. 3.12 Second modeshape for MMMM condition of micromirror

Fig. 3.12a Plot of 2nd mode for MMMM condition at y = 0.5

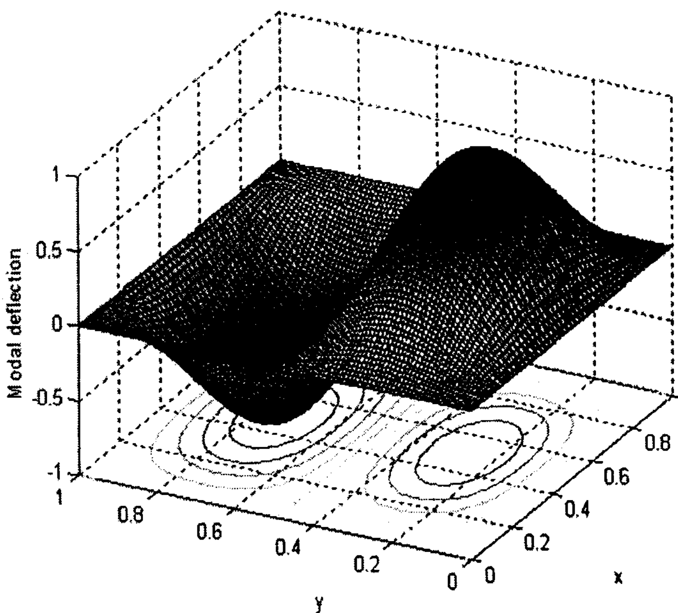

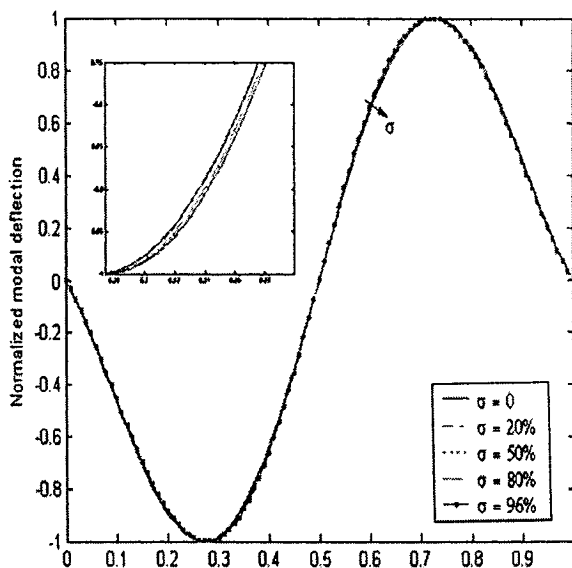

Fig. 3.13 Third modeshape for MMMM condition of micromirror

Fig. 3.13a Plot of 3rd mode for MMMM condition at y = 0.5

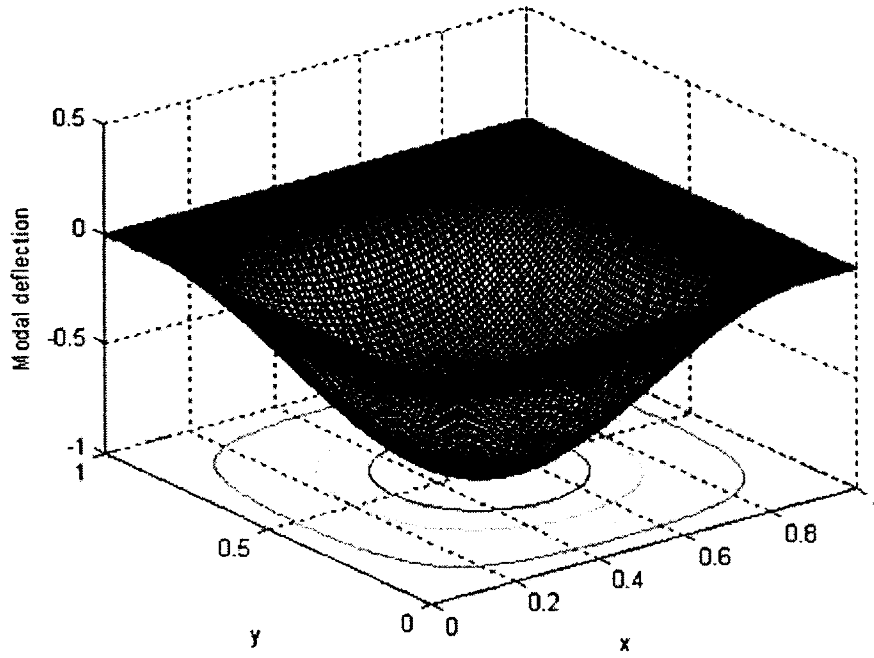

Fig. 3.14 First modeshape for SSSS condition of micromirror

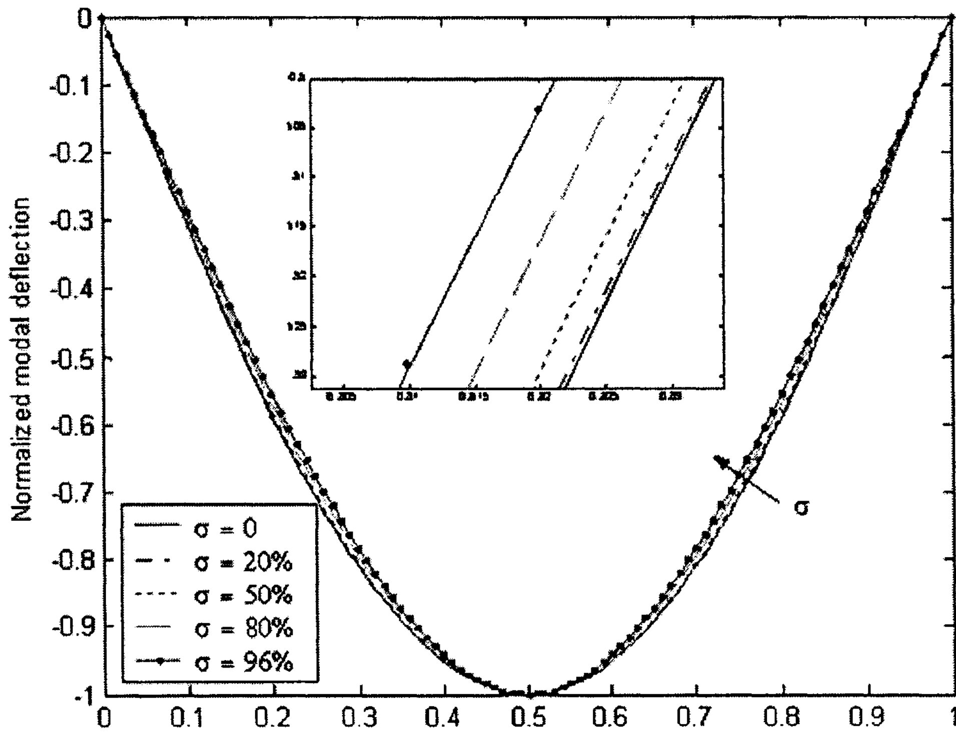

Fig. 3.14a Plot of 1st mode for SSSS condition at y =0.5

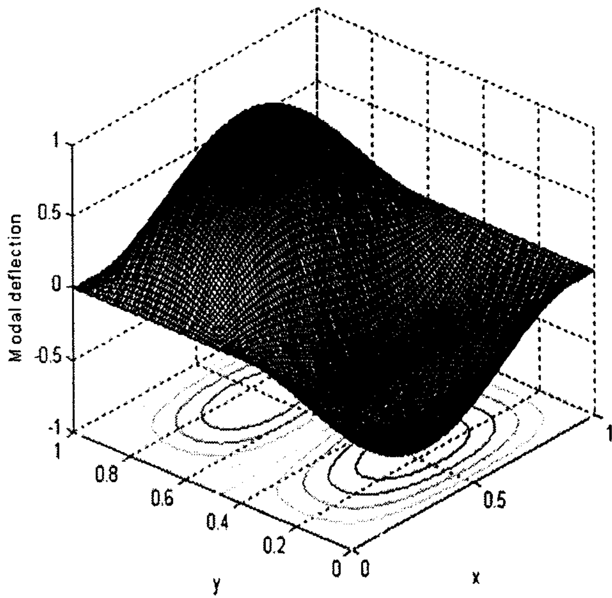

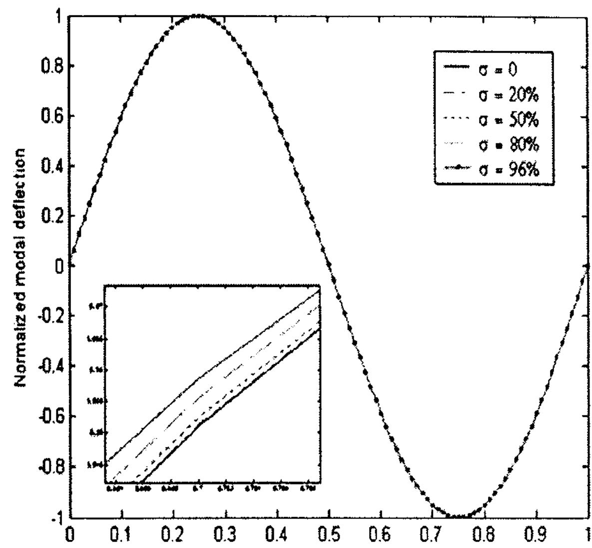

Fig. 3.15 Second modeshape for SSSS condition of micromirror

Fig. 3.15a Plot of 2nd mode for SSSS condition at y =0.5

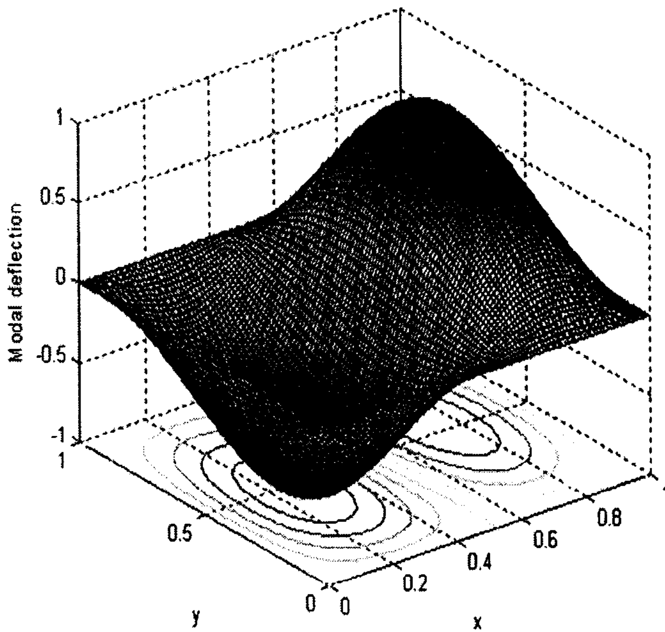

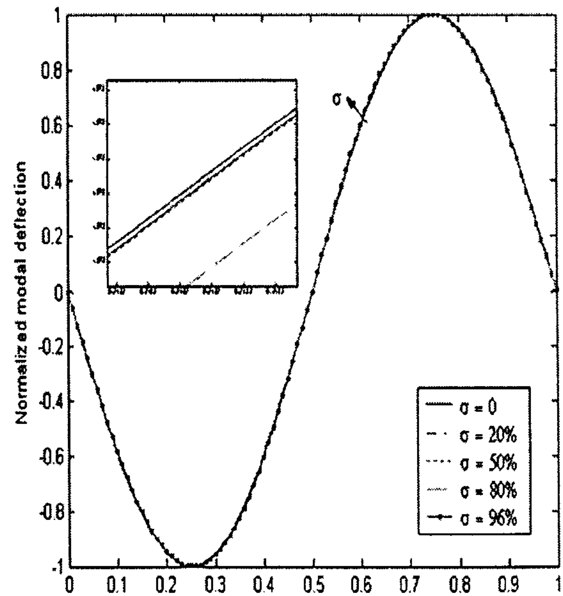

Fig. 3.16 Third modeshape for SSSS condition of micromirror

Fig. 3.16a Plot of 3rd mode for SSSS condition at y =0.5

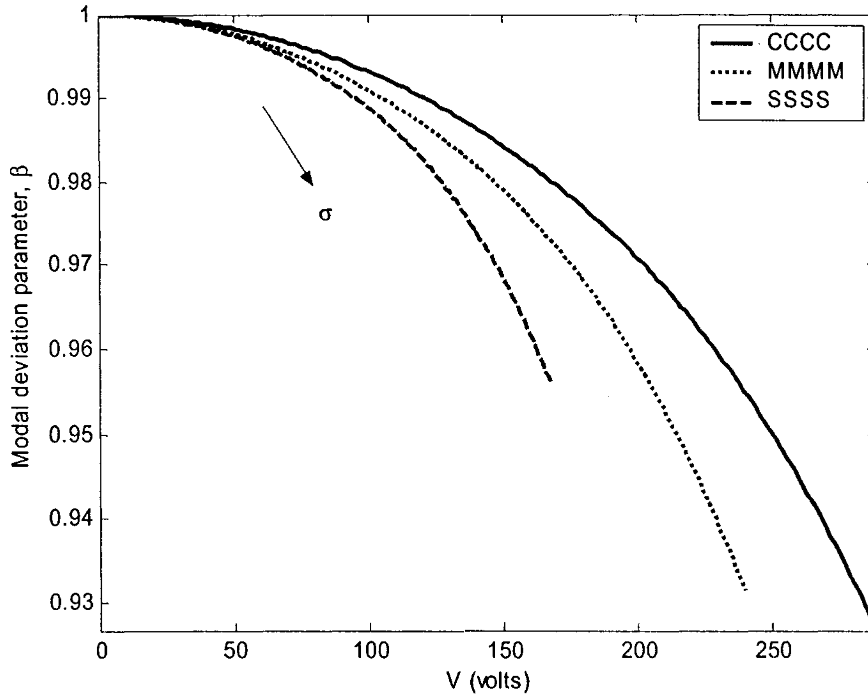

Fig. 3.17 Modal deviation parameter of the first modes for the three end support conditions

It can be seen from Figure 3.8a, 3.11a and 3.14a that the volume under the normalized fundamental modeshape decreases with increase in voltage parameter 'σ'. The variation in modeshape is quantified with a parameter 'β' which is defined as the ratio of volume under the normalized fundamental mode shape under no voltage to volume under normalized fundamental modeshape at a given voltage, V.

The parameter 'β' is considered as a modal deviation parameter. The variation of β against the voltage is shown in Figure 3.17 for CCCC, MMMM and SSSS end conditions. This figure shows that electrostatic field affects significantly the modeshape leading to narrower modeshapes with less volume. This trend is observed for all the three

end support conditions. However, from Figure 3.17, the modal deviation parameter due to the first mode for SSSS condition is much less than that of MMMM (which lies between CCCC and SSSS support conditions) and CCCC end support conditions. This clearly proves that the electrostatic field has a negative effect on the elastic property of the micromirror as it weakens the elastic property of the mirror which would affect the response of the microsystem. However, from the plots in Figures 3.9, 3.9a, 3.10, 3.10a, 3.12, 3.12a, 3.13, 3.13a, 3.15, 3.15a, 3.16, 3.16a of second and third modeshapes for the three end support conditions, it can be observed that the change in the modeshapes is less significant compared to the fundamental modeshape. This may be due to the fact that the fundamental modeshape has maximum deflection at the center whereas the other modeshapes have a node at the center. This shows that the electrostatic field on the micromirror affects the dynamic behavior of the mirror and this effect can be quantified by introducing non –uniform elastic foundation stiffness through the concept of boundary conditioning.

In this chapter the formulation to predict the static and dynamic behavior of micromirror of selected dimension using boundary characteristic orthogonal polynomials in the Rayleigh-Ritz method was shown. The effect of electrostatic field was quantified by non-uniformly varying stiffness value. It was shown that the electrostatic field significantly affects the elastic properties of the micromirror thereby affecting the dynamic behavior of the system. The concept of boundary conditioning has been successfully applied to quantify the influence of electrostatic field on the eigenvalues and modeshapes. As explained in Chapter 1, the micromirrors can be fabricated with various

microfabrication techniques. In Chapter 4, the microfabrication aspects of micromirrors will be discussed considering three different types of microfabrication technologies.

Chapter – 4
Micromachining methods

4.1 Introduction

The earlier chapters detailed the modeling of micromirrors and presented results based on surface and bulk micromachining processes. The theoretical model presented for MUMPS and SOI bulk micromachining processes can be applied to any dimensions of electrostatically operated micromirrors discussed, as in these cases the electrodes are of the length of the mirror and hence the counter electrostatic field does not exist. Hence in order to explore the process of microfabricating mirrors, MUMPS surface micromachining process and MicraGEM SOI bulk micromachining process were considered. Since MicraGEM SOI process provides only a fixed electrode gap, a feasibility study to fabricate a mirror with more electrode gap by backside or the handle side etching of SOI wafer was carried out to release the micromirrors of various sizes and shapes using gas phase XeF_2 dry etching. The process overview and the design layout of the two standardized processes, namely, MUMPS and MicraGEM and a detailed description of controlled pulse etching method using XeF_2 along with the method of mask development and photolithography is presented in this chapter. A discussion on the etch rate and the pressure variation during etching during the etching process is also presented.

4.2 Multi User MEMS Process (MUMPS)

4.2.1 Process overview

MUMPS is a popular surface micromachining technique. This polysilicon based surface micromachining was developed at the Berkeley Sensor and Actuator Centre in the late 80's and is now commercialized by MCNC [51] in North Carolina. The cross sectional view given below in Figure 4.1 shows the layers of materials used in the process flow of MUMPS.

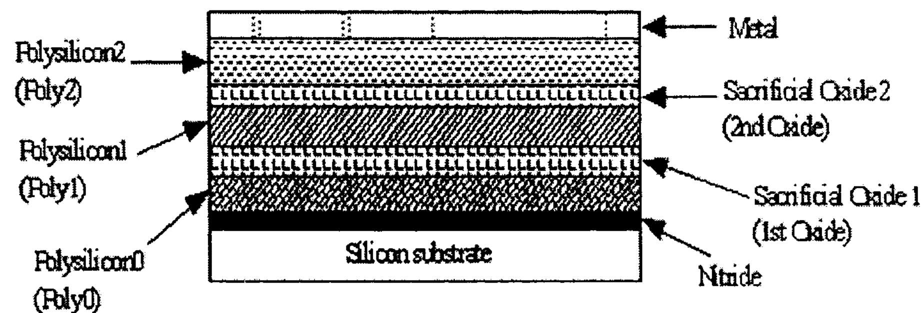

Fig. 4.1 Scheme indicating the sequence, material and grouping of layers in MUMPS [74]

The basic MUMPS process incorporates seven layers for its process flow with polysilicon being the structural layer, Phospho Silicate Glass (PSG) being the sacrificial oxide layer and Silicon Nitride as the insulating layer.

The process begins with n-type (100) 100 mm silicon wafers of 0.5 $\tilde{\Omega}$cm, resistivity. The surfaces of the wafers are first doped with phosphorous in a standard diffusion furnace. This helps reduce or prevent the charge feedthrough to the substrate

from electrostatic devices on the surface. Next, a 500 nm thick low stress silicon nitride layer is deposited using LPCVD (low pressure chemical vapor deposition) on the wafers as an electrical isolation layer. After which the first polysilicon layer (Poly0) is deposited. A 2.0 μm thick PSG sacrificial layer (Oxide1) is then deposited by LPCVD. This layer of PSG is removed at the end of the process to free the first mechanical layer of polysilicon (Poly1). The wafers are re-coated with photoresist and a suitable mask is used and unwanted PSG is removed by Reactive Ion Etching (RIE). Next, the first structural layer of polysilicon (Poly1) is deposited. The thickness of the polysilicon layer is 2.0 μm. A thin masking layer of PSG is deposited over the polysilicon and annealed at 1050° C for 1 hour. The polysilicon is doped with phosphorous from the PSG layers both below and above. Because the polysilicon is deposited as an amorphous film and then annealed at a high temperature, a fine grain size is developed and the polysilicon has very low stress. To pattern the polysilicon, the polysilicon-PSG masking layer is lithographically patterned which are then etched by RIE. The masking oxide is then removed from the front surface of the wafer. After the second layer of polysilicon is patterned, a second PSG layer (Oxide2) is deposited. This PSG layer will be removed at the end of the process to facilitate the release of the second mechanical polysilicon layer (POLY2). The MCNC process provides two layers to pattern the second PSG (Oxide2) layer. The first layer is used to remove the second oxide from the surface of the first polysilicon structural layer which in turn establishes a contact between first structural layer of polysilicon and second structural layer of polysilicon. Another mask layer is used to make contact between polysilicon 2 (Poly2) and the substrate (either Poly0 or the silicon nitride layer). The combined first and second oxide layers exposed by this mask

layer are then etched by RIE. After this, the second structural polysilicon layer (Poly2) is deposited using the same process as in depositing the first polysilicon structural layer. The second polysilicon layer is lithographically patterned with another mask and the pattern is transferred using RIE. Finally a 1.0 μm thick aluminum layer (Metal) is deposited by Lift-off method. This provides for electrical connections. Table 2.2 provided the thickness of each layer in the MUMPS microfabrication method.

4.2.2 Design layout

In the present work the design layout consists of rectangular and circular micromirrors of various dimensions as shown in Figure 4.2. Various types of micromirrors were designed to explore the feasibility of MUMPS process to fabricate the mirrors. As seen in the layout, the design consists of one dimensional torsional micromirrors and a two dimensional torsional micromirror. Figure 4.2 shows the design layout designed using the L-Edit layout editor of MEMSPRO [82] and the solid modeling of the mirror is shown in Figure 4.3. Figure 4.4 (a) shows the Scanning Electron Microscope (SEM) picture of the packaged fabricated dice. The chip shown in Figure 4.4 (a) is 64 pin packaged device. Electrical connections are provided by bonding the wires to the contact pads. A close-up view of the dice shows the SEM of the micromirror in Figure 4.4 (b). The top layer is the metal layer and the bottom layer is the Poly0 layer. Contact pads shown in the layout are provided for electrical connections and these are made of the layers used in the design.

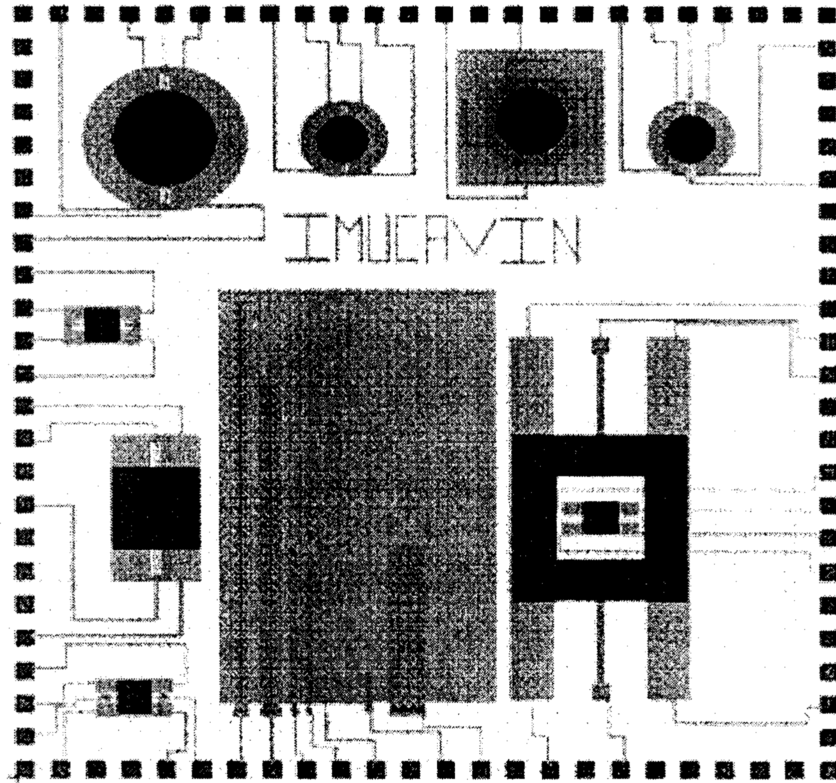

Fig. 4.2 Layout of design using L-Edit

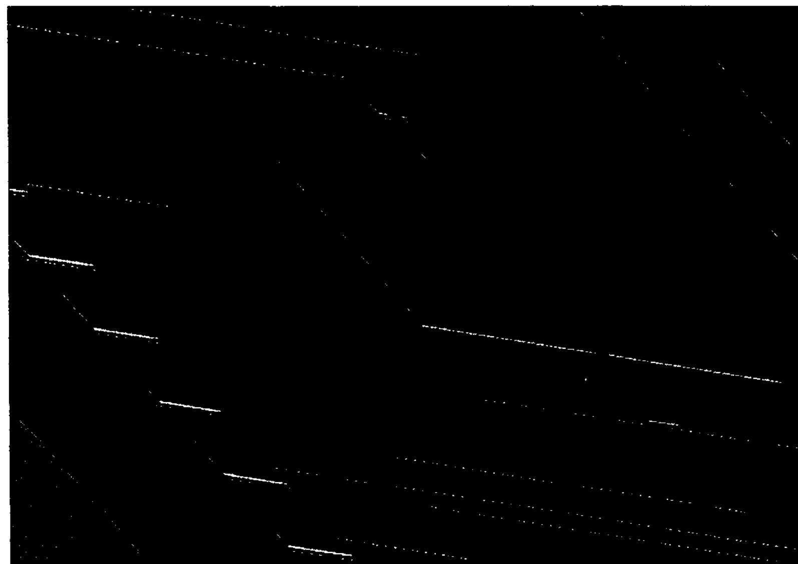

Fig. 4.3 Three-dimensional view of a micromirror present in Figure 4.2.

Etch holes on the micromirrors are provided in order to increase the sacrificial undercutting rate thereby decreasing the amount of time required to release the structure completely. However due to the presence of etch holes on the micromirrors, there may be diffraction and absorption of the light signal which can lead to loss of optical signal. In the present design, since the main focus is on MOEMS devices, with larger dielectric gap between the mirror and the substrate, only two poly layers namely POLY0 and POLY2 are used, thereby eliminating POLY1 layer in between which leads to a final dielectric gap of 2.75μm, as the sacrificial oxide layers in between POLY0 and POLY2 are also removed. Hence the micromirror is made out of structural layer POLY2 and the fixed electrode is made of structural layer POLY0. The torsion beam of the micromirror is attached to an anchor also made out of POLY2 and it is firmly attached to the substrate, but is electrically isolated from the electrodes made of POLY0 as shown in Figure 4.4 (c). A layer of metal (Al, Au) is deposited on top of the devices in order to increase optical reflectivity. However the intrinsic stress in the metal layers may lead to unwanted warping and distortion. As an example, SEM picture of the micromirror shown in Figure 4.4 (d) demonstrates the presence of residual stress as the mirror has curved due to stress. Figure 4.4 (e) and (f) show the other MUMPS fabricated mirror present on the chip.

Due to the factors of poor reflectivity, residual stress, etch holes and small gap, a SOI wafer based bulk micromachining process was considered, as the residual stresses involved in an SOI wafer is very low. The new technology called the MicraGEM SOI technology of Micralyne [52] uses SOI wafers which are bulk micromachined to release the devices. Since bulk micromachining is involved, the

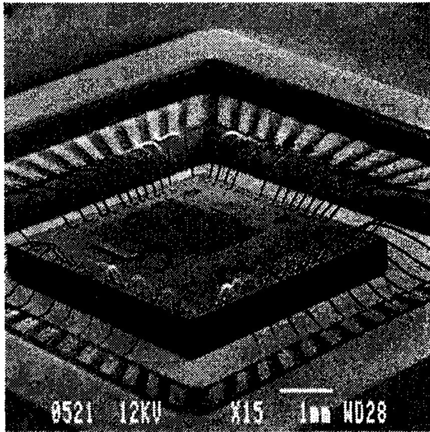

(a)

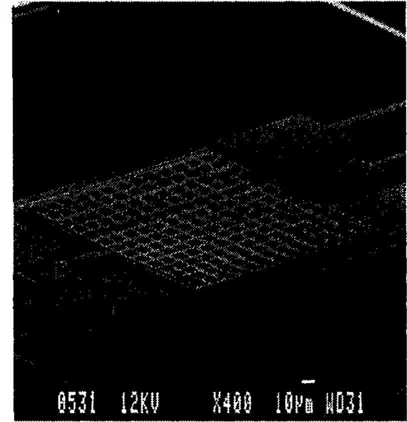

(b)

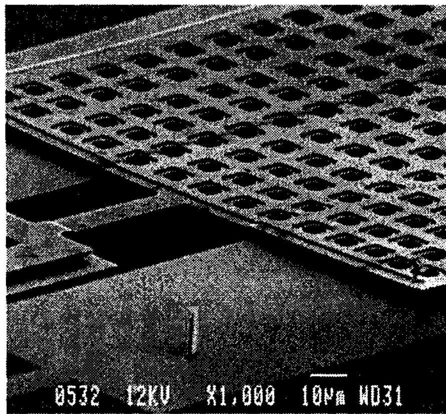

(c)

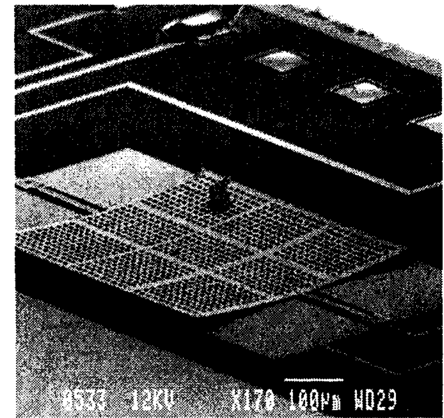

(d)

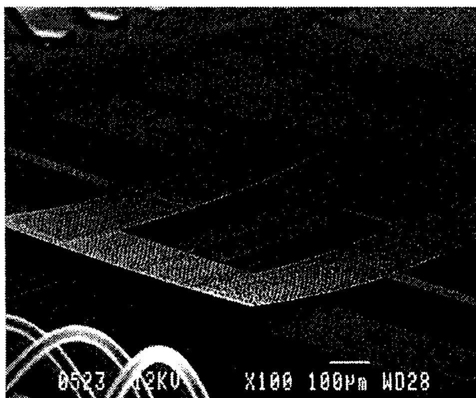

(e)

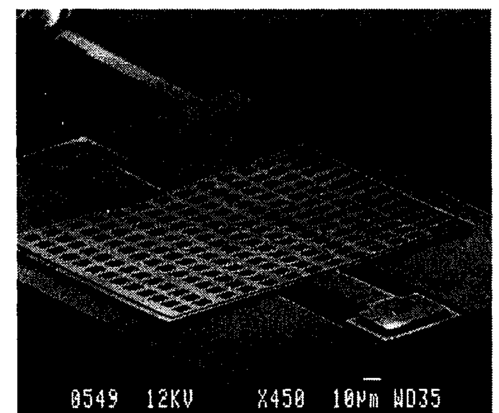

(f)

Fig. 4.4 SEM pictures of MUMPS fabricated devices

etch holes are not a requirement and hence this fabrication process would be ideal for MOEMS applications. The following section elaborates on the MicraGEM SOI technology.

4.3 MicraGEM SOI micromachining Process

4.3.1 Process overview

MicraGEM SOI process is a very new microfabrication procedure introduced by Micralyne [52] and made available to Canadian Universities through CMC. This process, unlike MUMPS, is a bulk micromachining process using Silicon On Insulator (SOI) wafers. Figure 4.5 shows the steps followed in the MicraGEM process.

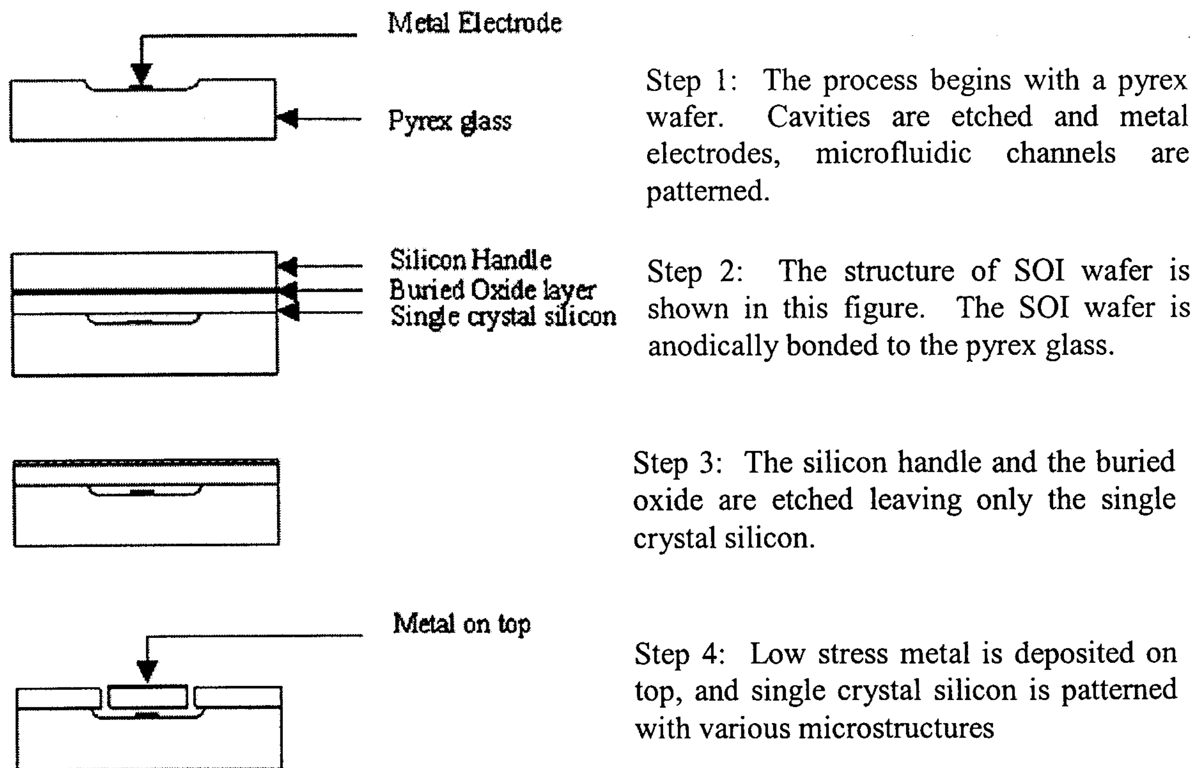

Fig. 4.5 Steps involved in MicraGEM SOI process [83]

4.3.2 Design layout

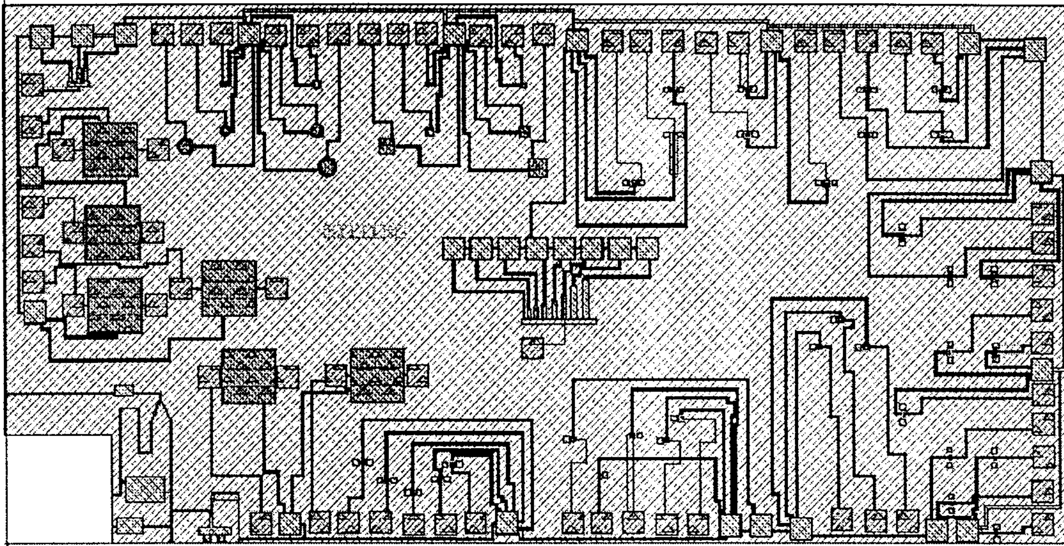

Fig. 4.6 Design layout

Figure 4.6 shows the design layout made in the present work for fabrication using MicraGEM SOI process. The design layout is generated using Virtuoso® layout editor of Cadence® [84] software. The layout consists of micromirrors of various dimensions, capacitive transducers, cantilevers, microfluidic channels. The micromirrors fabricated through this process are later tested for deflection angles for various voltages and natural frequencies and were compared with the theoretical results. The microfluidic channels are incorporated in the layout to explore the flexibility of this new fabrication procedure. In the present layout 84 contact pads have been used as the CMC [53] provides 84 pin package for the present microfabrication process. Figure 4.7 (a) shows the SEM of the fabricated packaged device.

This fabrication procedure was available with two options. The first option provided a gap of 10μm between the single crystal silicon device layer and the electrodes. The second option provided a gap of 2μm between the above mentioned layers. In the present work the second option is explored.

The metal as electrode is a combination of titanium, platinum and gold and is deposited using lift-off technique on the 525μm thick pyrex substrate. This provides for a good electrical conductivity as compared to MUMPS as in the MUMPS process the electrodes are made of polysilicon. The thickness of the metal layer is such that, the metal layer exists well within the pyrex etch. A 525μm thick SOI wafer is anodically bonded to the pyrex substrate. The buried oxide and the handle layer of the SOI wafer are completely etched out as explained earlier, leaving only the device layer or the single crystal silicon layer. This layer is then patterned to obtain the desired microstructures. As it has been proved that the SOI wafer has a very low residual stress, the MicraGEM SOI process has clear advantages over MUMPS in this regard. Hence there is no curling of microstructures as shown in Figure 4.7 (b). Chrome or gold layer is deposited on top of the single crystal silicon. The main advantage of this is that it gives enhanced reflectivity. Since this metal layer is patterned and etched to expose the underneath silicon, there are no etch holes present on top of the metal layer as compared to the MUMPS process. This can be observed in the accompanying SEM pictures in Figures 4.7 (c), 4.7 (d) and 4.7 (f). Finally the structures are patterned and released using Deep Reactive Ion Etching (DRIE).

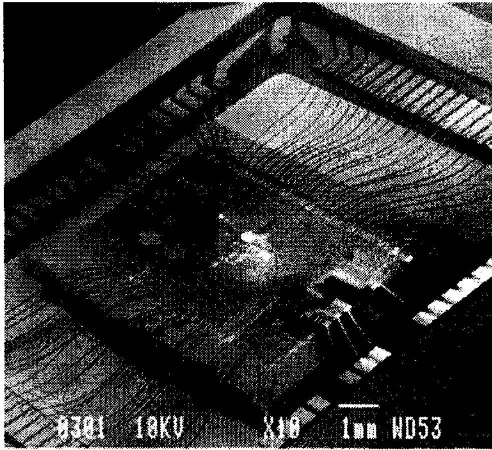

(a)

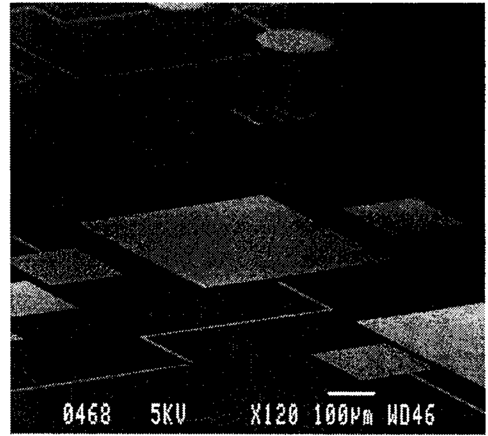

(b)

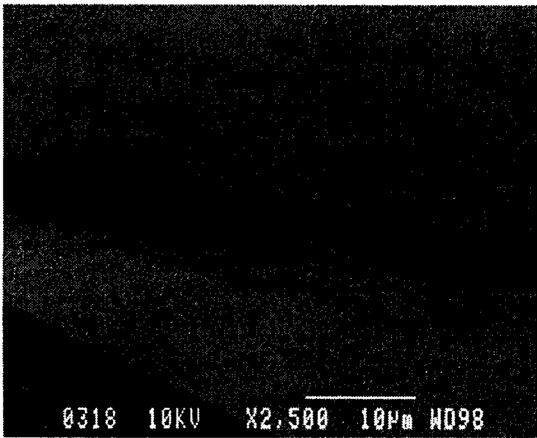

(c)

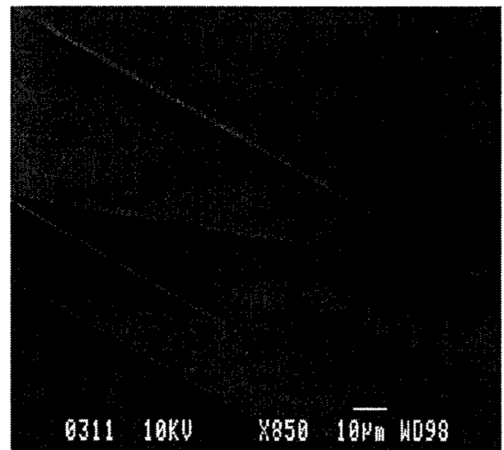

(d)

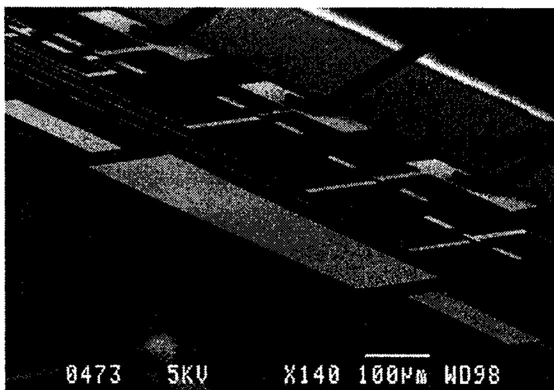

(e)

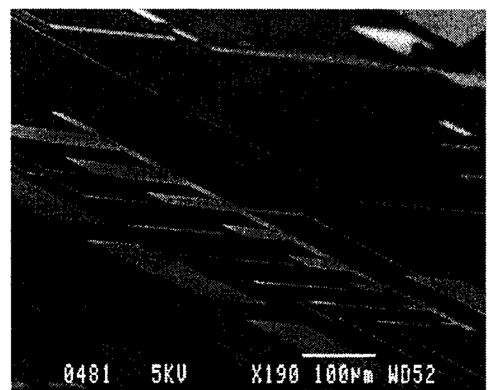

(f)

Fig. 4.7 SEM pictures of the devices fabricated through MicraGEM SOI process

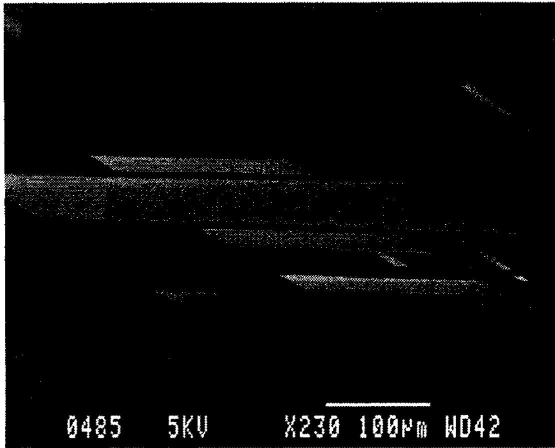

(g)

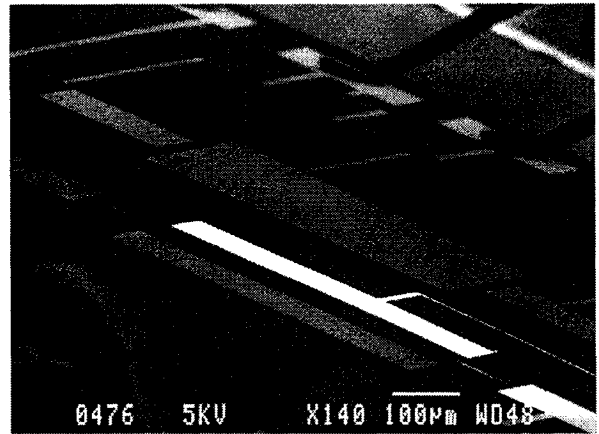

(h)

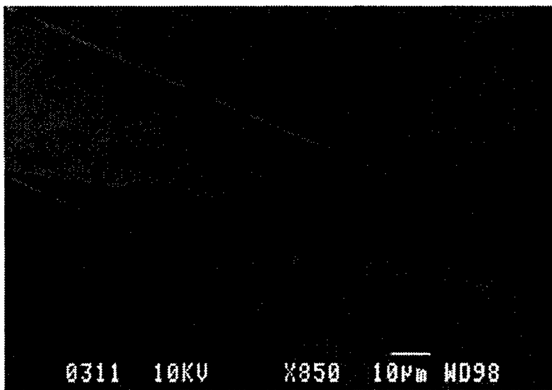

(i)

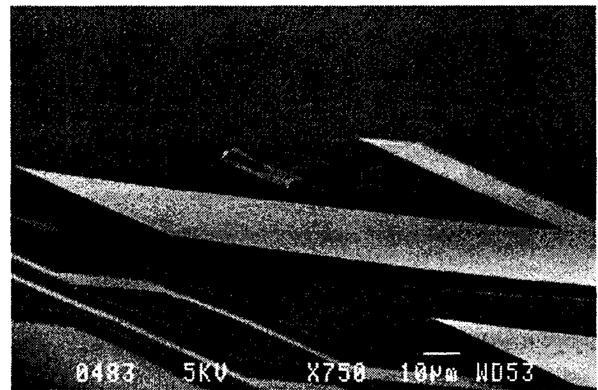

(j)

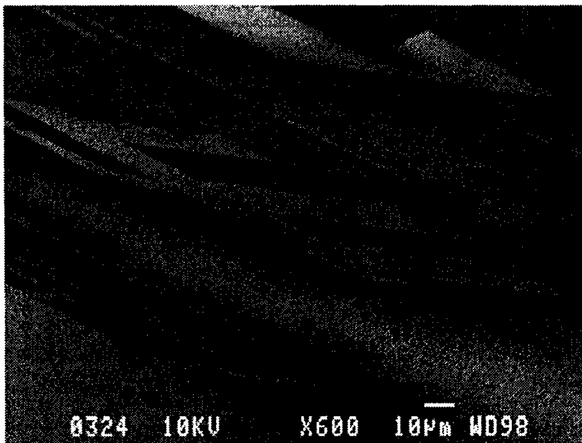

(k)

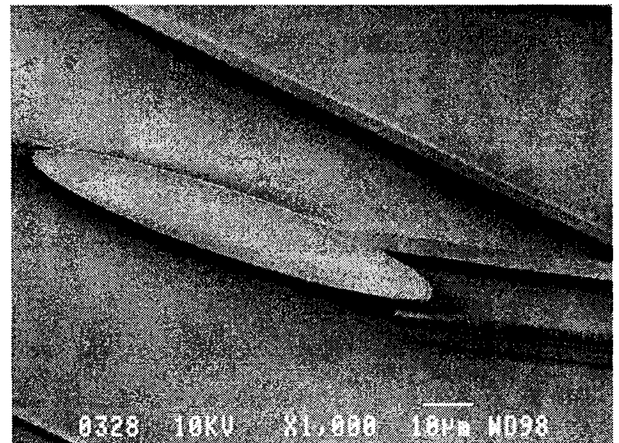

(l)

Fig. 4.7 SEM pictures of the devices fabricated through MicraGEM SOI process

The MicraGEM SOI process is well suited for MOEMS applications as it uses SOI wafers which have low residual stress and high optical reflectivity. Also the chrome or the gold deposition on top of this layer increases the reflectivity and hence it is ideal for fabrication of micromirrors. As there are no etch holes present on top of the metal layers, it will not lead to any noise as compared to MUMPS process. However it allows only a fixed electrode gap of 10μm or 2μm which applies certain restrictions on the design for electrostatically actuated devices such as micromirrors. To overcome this limitation, a feasibility study on the bulk micromachining etching using XeF_2 dry isotropic etchant is presented in the following section.

4.4 Feasibility study of bulk micromachining of SOI wafers using double side XeF_2 etching

4.4.1 Introduction

Chapter 1 dealt with bulk micromachining, and the types of etchants used for micromachining. It also briefly explained the structure of Silicon On Insulator wafers, and the different fabrication procedures involved. In the present work, fabrication of different micromirrors of various dimensions has been attempted using dry, isotropic Xenon difluoride (XeF_2) etchant.

Many studies on the etching of silicon with XeF_2 as an etchant have been carried out previously [85-86, 88]. XeF_2 is a dry, isotropic white crystal at room temperature

and pressure and it sublimates at approximately 4 torr at $25^{\circ}C$. The etching is carried out with gas phase XeF_2. The main advantages of using XeF_2 are its high selectivity to aluminum, photoresist and silicon dioxide. The gas phase XeF_2 etching also minimizes adhesion and stiction problems and its higher isotropic etch rate allows large structures released quickly.

Two different types of etching methods are generally used for XeF_2 etching [86]. In the first method called the pulse etching method, the sample to be etched is alternately exposed to XeF_2 vapor and nitrogen gas. The other method called constant pressure etching consists of etching at a constant pressure for a designated amount of time, which is easier and more convenient for longer etching times.

Silicon On Insulator (SOI) wafers are used increasingly for many optical applications due to its flat and polished surface, stress-free nature, and compatibility for fabricating high thickness structures. MicroElectroMechanicalSystems (MEMS) engineers are using this variation of the conventional silicon wafer to fabricate micromirrors, and scanning mirrors for optical communication. For MOEMS (Micro Opto Electro Mechanical Systems) SOI wafers are ideal as they do not have the drawbacks of conventional wafers such as increased stress level, decreased microfabrication possibilities, small thickness, limitation in the use of voltages [87].

In the present work pulse-etching method is proposed due to its better control and etching uniformity. The process flow involves mask preparation, photolithography and etching.

4.4.2 Process flow

4.4.2.1 Mask preparation

Every microfabrication process involves mask preparation as this is the most important step which determines the shape and the dimension of the microstructure desired. In the previously explained fabrication procedures the masks were prepared according to the design guidelines set for the mentioned fabrication procedures. Hence previously MemsPro and Cadence were used to design the masks. For the present bulk micromachining, as there is a flexibility in the design in considering various parameters such as geometry, electrode gap, structural thickness, etc, different masks were prepared to suit the etch rate of xenon difluoride and the limitations imposed by the etch facility. The masks were designed using AutoCad drawing tool. All the masks used are light field masks. Figure 4.8 shows some of the masks designed for the present bulk micromachining. The dimensions of the micromirrors considered for this fabrication flow varies from 1mm x 1mm to 6mm x 8mm in length and breadth of the micromirror, respectively. The torsion beam width is from a minimum of 50μm to a maximum of 500μm. The types of mirrors explored are both scanning mirrors and 90° torsional micromirrors.

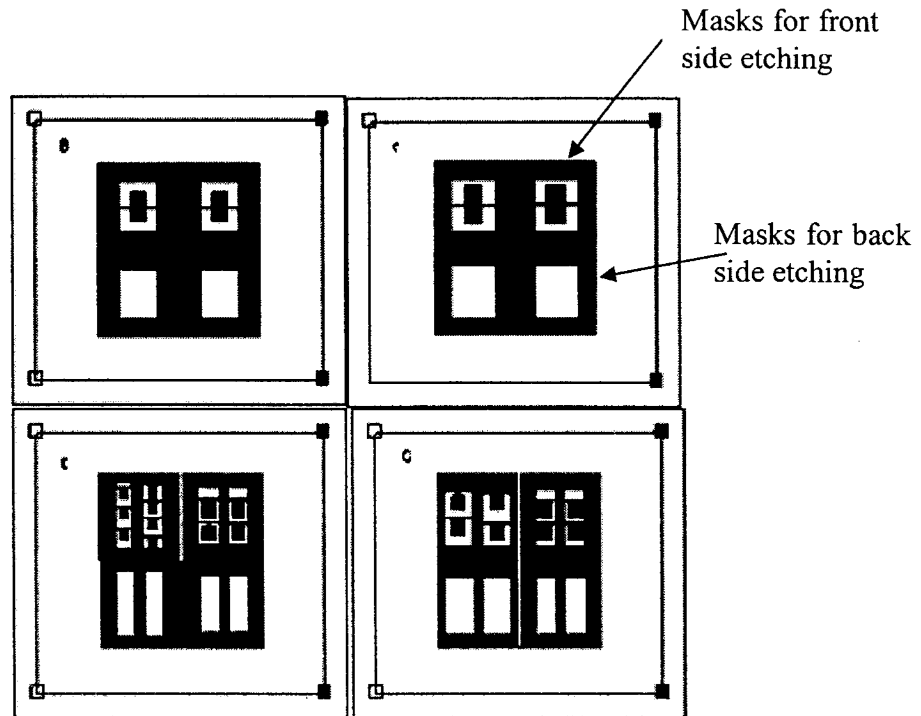

Fig. 4.8 Sample masks of micromirrors

As there were limitations associated with the mask aligner and the dimensions of the diced SOI wafers, the masks were designed considering those parameters also. Hence, in Figure 4.8 each micromirror can be exactly patterned on a single diced SOI wafer of dimension 15mm x 15mm. The figure also shows the pattern used for back side etching. These back side etching patterns match the dimensions of the openings used to release the micromirror. The masks are printed on a photosensitive film sheet to be used in the photolithography.

4.4.2.2 Photolithography

Fabrication of MEMS devices starts with the process of photolithography. Photolithography is the process of transferring a pattern from a mask to the substrate. The goal is to expose parts of the wafer to the subsequent processing step while protecting the rest of the wafer. This is done through a sequence of steps: application of photoresist, selective UV exposure through the mask, and development of the patterned layer which removes exposed photoresist from the desired regions. Photoresist is a liquid polymer that can be spread out onto a substrate, exposed with a desired pattern, When negative phototoresist is exposed to UV rays, the part of photoresist which is not exposed to the UV light is removed. A positive photoresist exactly works the opposite way as that of a negative photoresist. In the present work positive photoresist is used. The basic steps involved in the photolithographic process are wafer cleaning, pre-baking, photoresist application, spin coating, soft baking, exposure, development and hard baking.

Steps in photolithography

1. In the wafer cleaning method the SOI wafers are cleaned with acetone solution to remove possible dust particles, abrasive particles, photoresist residue from previous photolithography and films from other sources such as solvent residue.

2. In prebaking, the wafer is heated to about $90^{\circ}C$ for 30 minutes in a baking oven. The prebaking of wafers removes water and remains of acetone content present on the wafer.
3. The next step in photolithography is photoresist application. The method of photoresist is applied on a SOI wafer using 'Spin coating' technique. In spin coating, the SOI wafer is held on vacuum chuck, photoresist is applied on the wafer and the wafer is subjected to high speed spinning. Spin coating of SOI wafers produces a thin uniform layer of photoresist on the wafer surface. In this work a positive photoresist was used for spin coating, a thickness of 2~4 microns was obtained with a spin coating for 120 seconds at 2500rpm.
4. After spin coating, the wafer with the photoresist is soft baked which increases the photosensitivity of the photoresist.
5. The softbaked photoresist is then exposed to UV radiation and developed. This leaves the pattern on the SOI surface.

The photograph in Figure 4.9 shows the mask aligner and the spin coater. On the right of the photograph is the spin processor and on the left is the mask aligner. After developing, the wafer is hard baked. This is the last step in the photolithographic process. This step is necessary in order to harden the photoresist and improve adhesion of the photoresist to the wafer surface. Figure 4.10 shows the SEM of one of the patterned micromirror using photolithography.

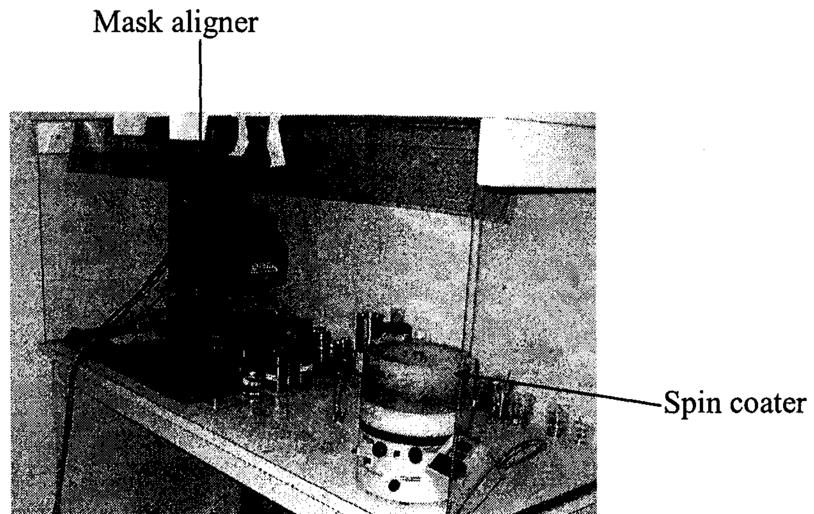

Fig. 4.9 Photolithography setup showing the mask aligner and the spin processor

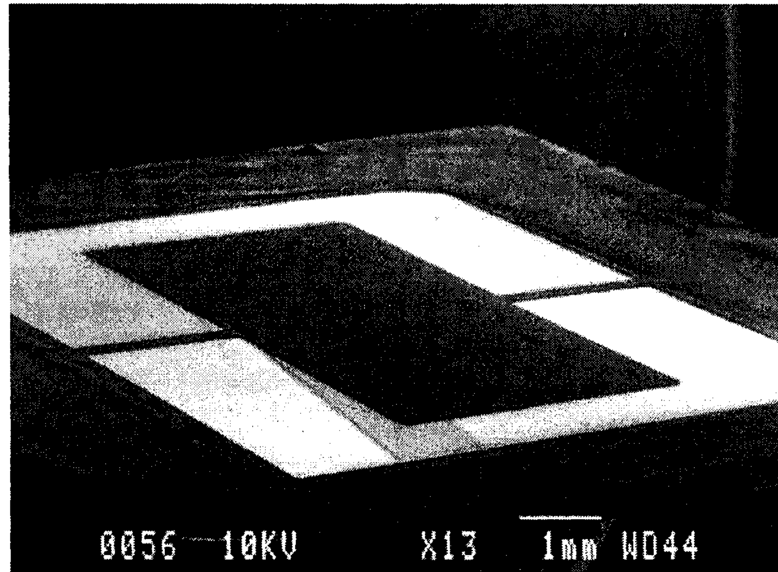

Fig. 4.10 SEM picture of the patterned micromirror on the SOI wafer.

As the XeF_2 does not etch the photoresist, the photoresist is used as an etch stop. Hence, wherever the etching is not desired, the photoresist is painted on that part to

protect it from etching. After patterning, the wafer is subjected to etching using XeF_2. The following section details the process.

4.4.2.3 Dry etching using isotropic XeF_2 etchant

In the present work a <100> p-type SOI wafer with handle thickness of 400μm, buried oxide (BOX) thickness of 1μm and single crystal silicon thickness of 5μm has been used. The 100mm diameter wafer of SOI is diced into 15mm x 15mm dices. A customized holder was designed for the purpose to handle the diced wafers in the etching chamber.

4.4.2.3.1 Etching method

As mentioned earlier XeF_2 is a dry, solid white crystal at room temperature which sublimates at approximately 4 torr at $25^0 C$. Some of the advantages of using XeF_2 are its high selectivity to aluminum, photoresist, gold, silicon nitride and lower adhesion and stiction due to the gas phase of XeF_2. The basic reaction underlying XeF_2 etching process is given as

$$2XeF_2 + Si \rightarrow 2Xe + SiF_4$$

The etching mechanism involves the following steps [85]: (1) non-dissociative adsorption of the gas at the solid surface (2) dissociation of the adsorbed gas (3) reaction between adsorbed atoms and the solid surface to form adsorbed product molecule e.g., SiF_4

(4) desorption of the product molecule into the gas phase and (5) the removal of non-reactive residue from the surface. Figure 4.11 shows the schematic of the experimental setup for XeF_2 etching.

The setup consists of an etch chamber connected at one end to the vacuum pump through a liquid nitrogen trap and an on-off valve. The chamber is also connected to the stainless steel container of XeF_2 crystals through a supply valve, and to nitrogen gas supply through a purge valve. A capacitance manometer and a pressure gauge are also connected to the etch chamber. The chamber has a feed-through for loading the specimen chips into the chamber. The materials used for building the etching system include stainless steel, aluminum, Viton O-rings, glass, Inconel alloy and a standard mechanical vacuum pump [59]. Figure 4.12 shows the photograph of the pulse etching setup in fumehood during operation.

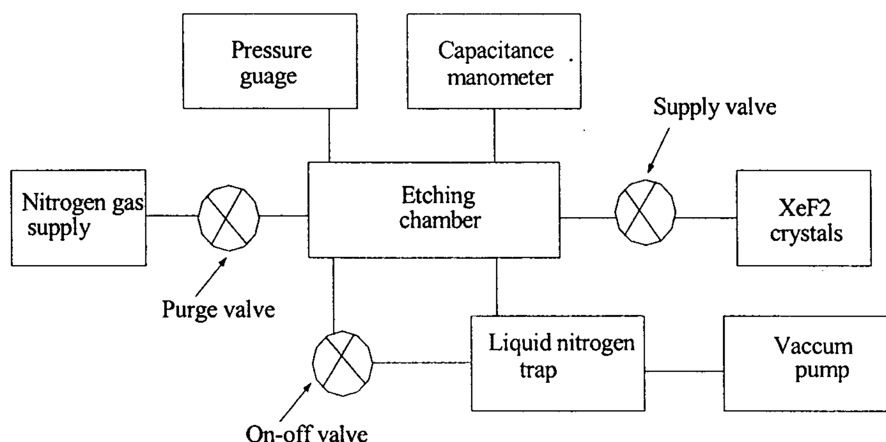

Fig. 4.11 Schematic of XeF_2 setup.

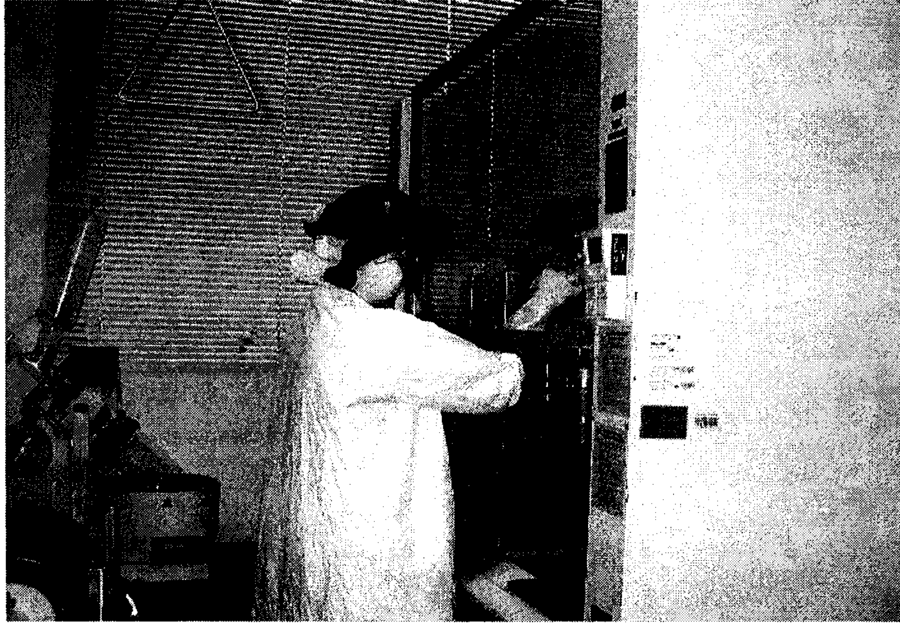

Fig. 4.12 Photograph of the XeF_2 pulse etching setup in fume hood during operation

4.4.2.3.2 Microfabrication results and discussion

The process flow used for double side XeF_2 etching is outlined in Figure 4.13. The SOI wafer is patterned on both sides with photoresist. The device layer on top is patterned with micromirror and the handle layer on bottom is patterned for back side etch pattern as shown in Figure 4.13 (a) using photolithography.

(b) Initial etching for about 5 pulses is carried out to realize the micromirror on the device side. As the thickness of the device side is only 5μm, it was observed that 5 pulses are sufficient to etch away 5μm of silicon depth. Simultaneously the handle side will also be etched by about 5μm depth as shown in Figure 4.13 (b).

(c) The handle layer of the SOI is about 400μm thick, and due to varying etch rate of XeF_2 which depends on the etch window as studied in a previous work [89], it is estimated that for the present openings on the back side, the etch rate is about 1.5 μm/min. Hence about 260 pulses are required to etch away this handle thickness. In order to avoid the under etching on the device side, the device side is completely coated with photoresist and the back side is etched as shown in Figure 4.13 (c).

(d) After step (c), the releasing of micromirror can be carried out by etching the buried oxide layer using 49% concentrated HF solution, as this solution etches only oxide leaving the silicon un-etched as shown in Figure 4.13 (d).

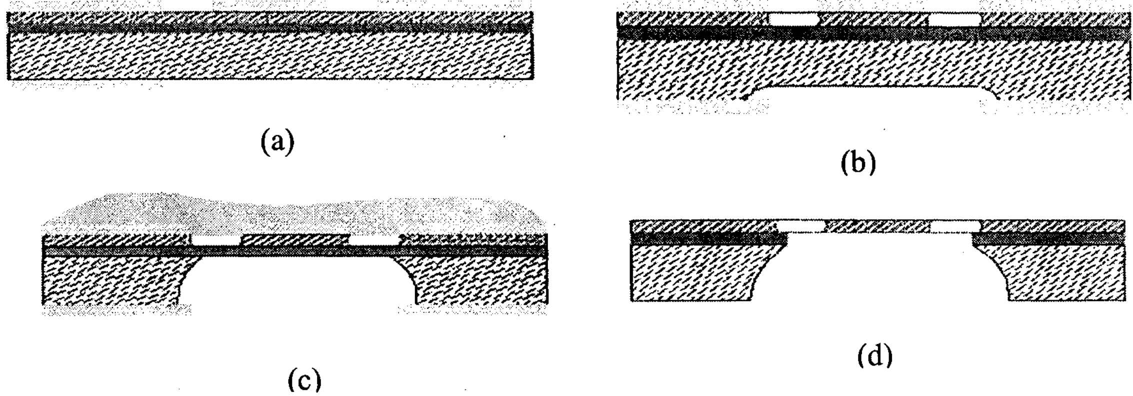

Fig. 4.13 Process flow adopted for XeF_2 bulk micromachining

The following graphs in Figure 4.14 are the variations of pressure in the etch chamber during the actual etching process. Each graph in Figure 4.14 indicates a sudden rise in pressure of XeF_2 in the etching chamber. During this time the inlet valve of the XeF_2 is opened for the entry of XeF_2 into the etching chamber. As a result there is a steady increase in the pressure. This pressure is brought to a predetermined level before closing the inlet valve of XeF_2. This predetermined level was determined based on many

factors. In Figure 4.14 (a) it can be observed that the starting etching pressure is slightly above 2 torr. It was observed during etching that as the etching pressure was maintained above 2 torr, the XeF_2 etching was very rapid and very difficult to control which usually resulted in damaging the photoresist coat on the silicon surface which was not to be etched. This resulted in etching to be stopped after 20 pulses for a recoat of photoresist. It was also observed during this process that silicon under the photoresist was also attacked. Hence in Figure 4.14 (b), the initial pressure was brought down to around 1.6 torr. The pressure of 1.6 torr was not sufficient to etch the silicon with the dimensions presented earlier. It can be observed in this figure that the final pressure did not cross more than 1.8 torr. It was found that 1.8 torr of initial pressure of XeF_2 as shown in Figure 4.14 (c) in the etching chamber resulted in etch rate of 2μ/min as calculated by the optical microscope picture presented in Figure 4.15. Figure 4.15 (a) shows the top surface of the corner of the device covered with photoresist. Figure 4.15 (b) shows the etch surface at the same corner. By measuring the etch depth underneath the photoresist, the under etch can be calculated for each pulse or for a minute by noting the number of pulses required to achieve the measured etch depth. In Figure 4.14, it can be seen that after the inlet valve to the etching chamber for XeF_2 is closed, the pressure attains a steady state. This steady state indicates the etching of silicon which is maintained for 60 seconds called 1 pulse. During this process XeF_2 is present in the etching chamber. Once a pulse is completed, the valve of nitrogen gas is opened to purge the etching chamber with nitrogen. The new pulse is started by creating vacuum in the chamber. Once the vacuum is created the inlet valve of XeF_2 is opened to release the gas into the chamber and the cycle is repeated.

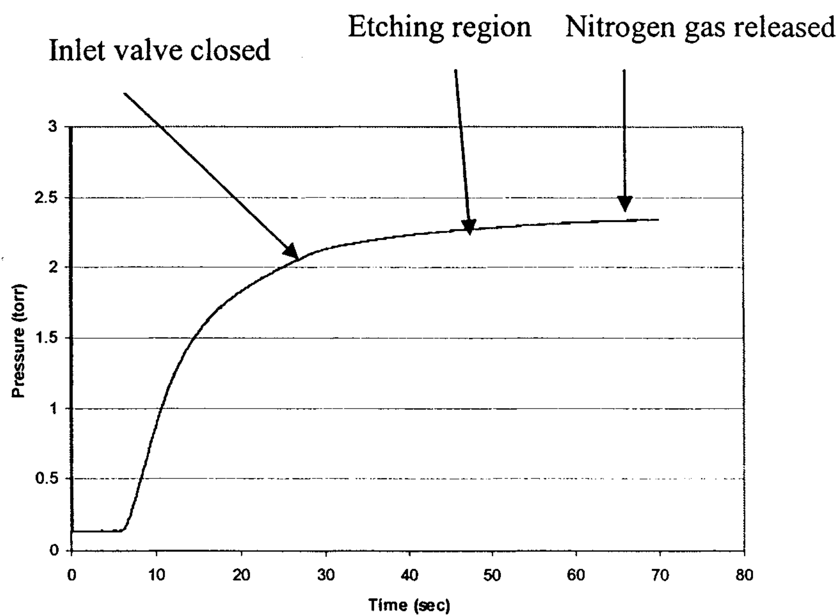

Fig. 4.14(a) A particular pulse showing the maximum initial pressure of XeF_2 in the chamber as 2 torr

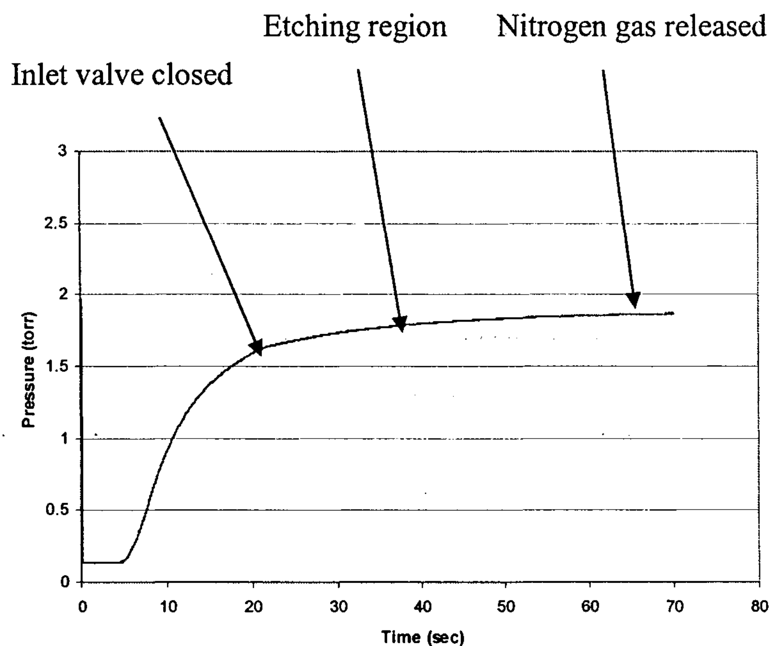

Fig. 4.14(b) A particular pulse showing the maximum initial pressure of XeF_2 in the chamber as 1.6 torr

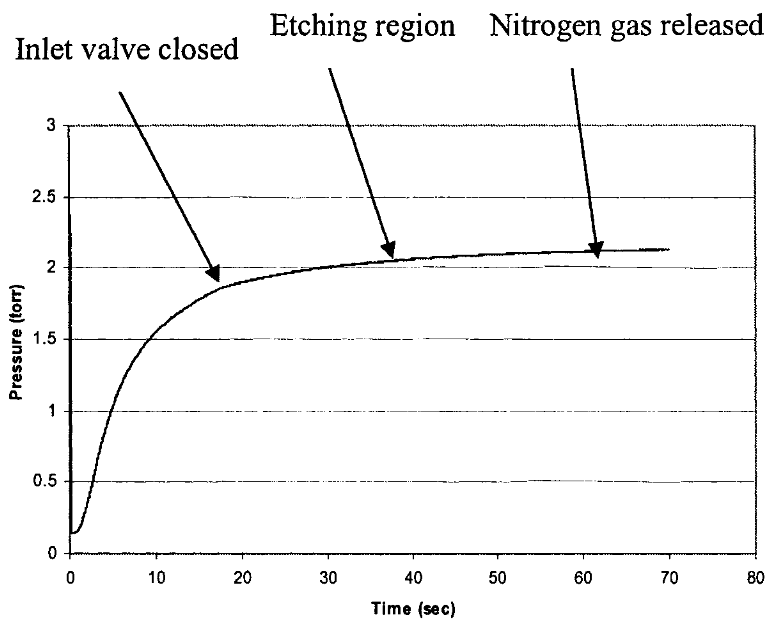

Fig. 4.14(c) A particular pulse showing the maximum initial pressure of XeF_2 in the chamber as 1.8 torr

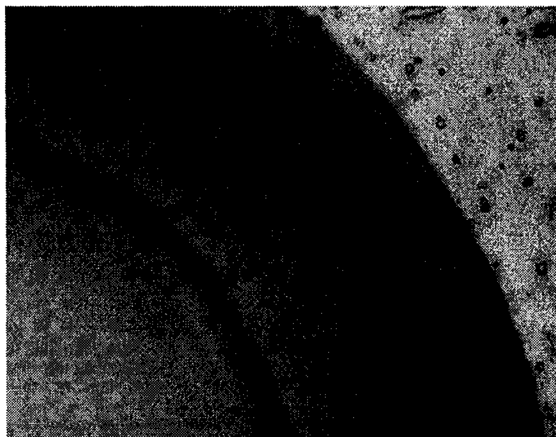

(a) Top surface

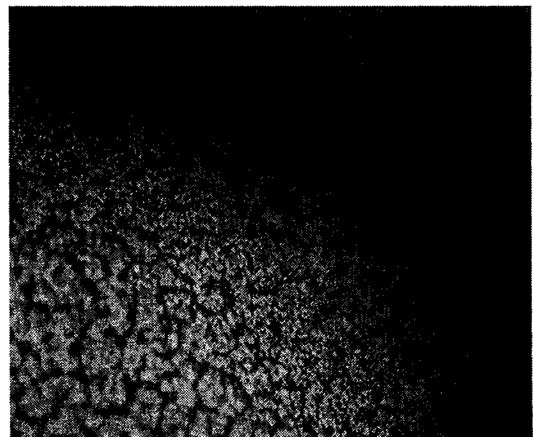

(b) Bottom surface

Fig. 4.15 Optical microscope pictures of etched specimen for etchrate measurement

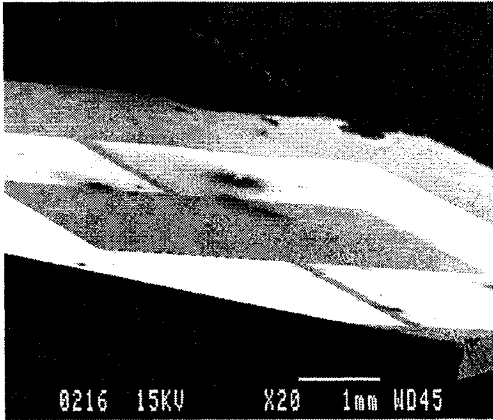

(a)

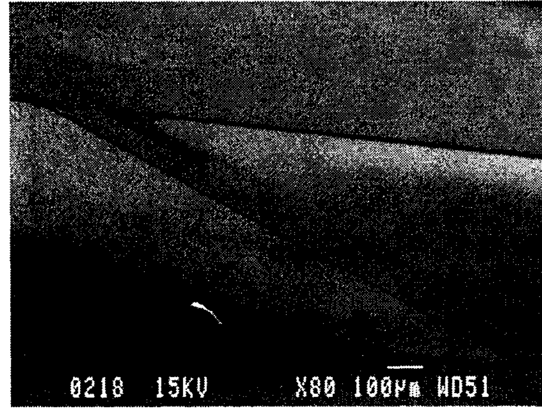

(b)

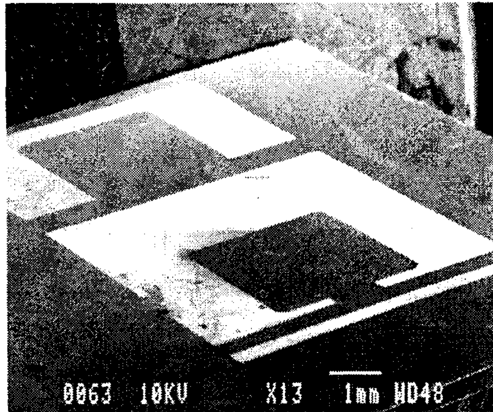

(c)

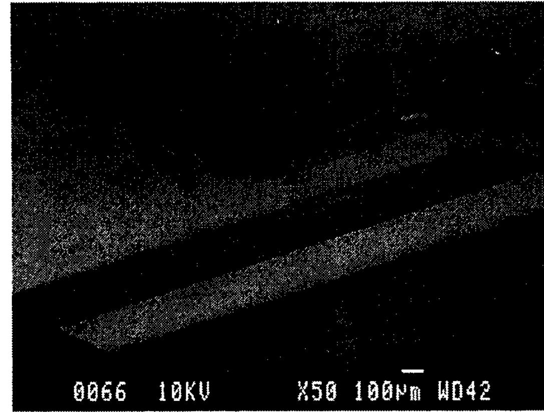

(d)

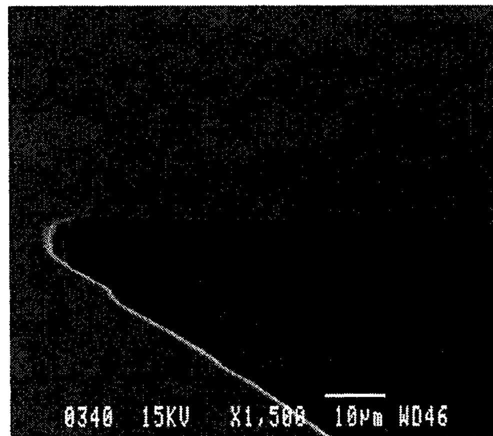

(e)

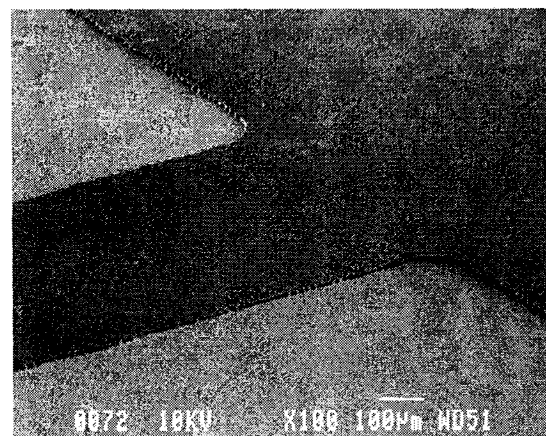

(f)

Fig. 4.16 SEM pictures of micromirrors on the device side of the SOI wafer

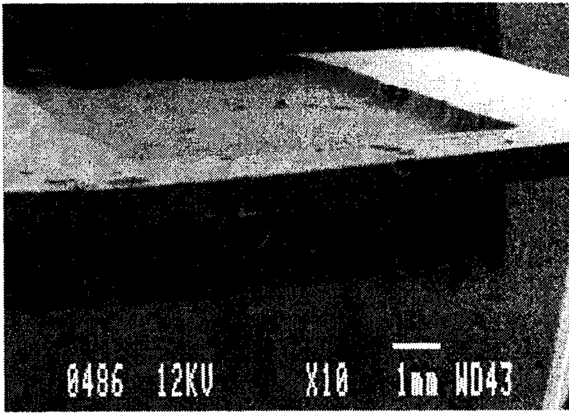

(a) after 180 pulses

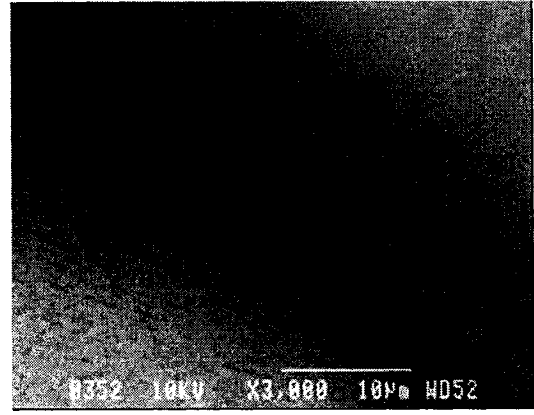

(b) after 75 pulses

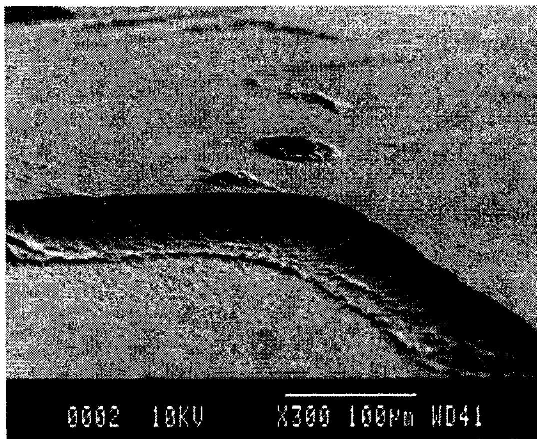

(c) after 110 pulses

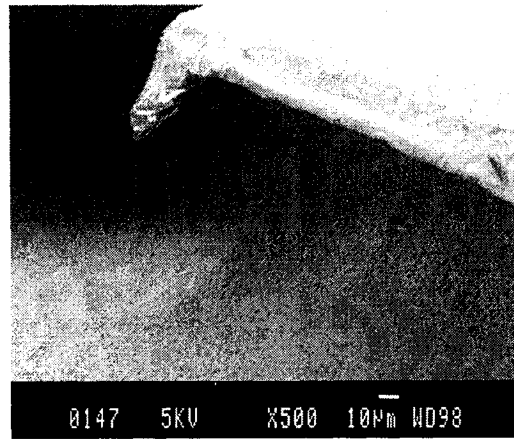

(d) after 130 pulses

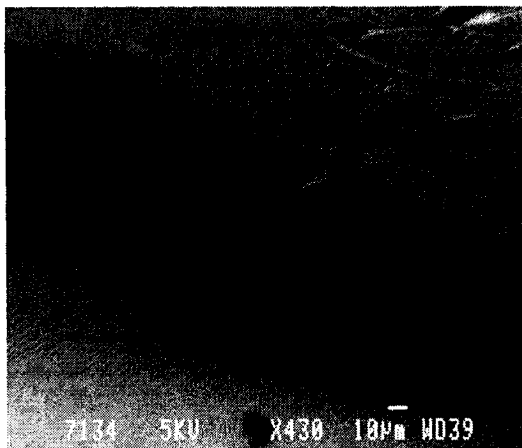

(e) after 150 pulses

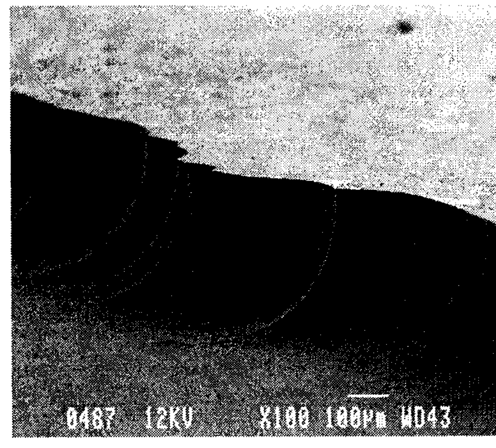

(f) after 180 pulses

Fig. 4.17 SEM pictures of etched handle side or backside of SOI wafer

The results of the feasibility study are presented in SEM pictures shown in Figures 4.16 which shows the micromirrors realized on the device side of the SOI wafer. Figure 4.16 (a) and (c) show the scanning micromirror and the 90° torsional micromirror etched on the device side of the SOI wafer. Figure 4.16 (b) shows a close-up view of the torsion beam of the scanning mirror. Figure 4.16 (d) shows the close up view of Figure 4.16 (c). From these figures, buried oxide layer of SOI wafer can be observed, as the surface is smooth without any visible roughness which can be observed in Figure 4.16 (e). In these figures the torsion beams of the micromirrors are firmly held by the supporting structures and the etching is uniform over the surface of the device layer of the SOI wafer. After this step as explained earlier, the top side is completely coated with photoresist. Further etching is carried out which etches only the handle layer or the back side of the SOI wafer.

The results of the back side etching are presented in Figure 4.17. Figure 4.17 (a) clearly shows the isotropic nature of XeF_2 etchant as the surface is uniformly etched. The SEM etch results presented are taken after completion of certain pulses. Figure 4.17 (b) shows the etch depth obtained after 75 pulses of etching. Figure 4.17 (c) is the etch depth obtained after 110 pulses of etching. Figure 4.17 (d) ,(e) and (f) are obtained after 130 and 150 and 180 pulses of etching, respectively. In these figures it can be observed that the etching is uniform throughout and a constant etch rate of ~ 2μm/min was maintained. The back side or the handle side of the SOI wafer was subjected to a maximum etching of about 180 pulses. Figures 4.17 (b), (d) and (e) all have photoresist which could be seen hanging in the pictures. This is due to the fact that the etching is isotropic resulting in

etching underneath the photoresist. From this the etch depth obtained can be clearly measured. A maximum etch depth of 310μm was reached during this feasibility study. Since the SOI wafers taken for etching had a handle or back side thickness of 400μm, an additional 90μm needs to be etched to complete the release of the mirror. Since after 180 pulses as seen from the figures the structure is safe with minimum damage, the releasing of the mirror can be achieved with additional 60 pulses.

From this feasibility study it can be concluded that the method proposed for etching Silicon On Insulator (SOI) wafers, using XeF_2 dry isotropic etchant can be used to fabricate the micromirrors. The method adds more flexibility to the design and fabrication of micromirrors compared to other industrial microfabrication procedures discussed earlier. The limitations posed through this long etch process due to the technical difficulties associated with the etch set up renders the present work to be stopped after 80% of back side etching.

In Chapter 4, based on the theoretical modeling, the possibilities of microfabricating the mirrors with surface and bulk micromachining procedures have been explored. It was shown that the controlled pulse etching using XeF_2 of SOI wafers offers more flexibility compared to the standardized processes such as MUMPS and MicraGEM. The various limitations and advantages of each microfabrication procedure were mentioned. As the theoretical modeling can be applied to any dimension of the mirrors discussed, one such mirror from the MicraGEM SOI fabricated chip is taken to validate the theoretical results through experimentation. The microfabrication technologies that were used to fabricate

the mirrors demonstrate the feasibility of fabricating mirrors through surface micromachining (MUMPS), hybrid SOI machining (MicraGEM), and double side bulk XeF_2 machining. Depending upon the requirement, one could select any of the above fabrication methods. In the following chapter the complete testing method used to test the mirror for static and dynamic performance will be explained with the results.

Chapter – 5
Testing

5.1 Introduction

The testing of micromirrors were carried out in order to validate the theoretical model. The testing method discussed in this chapter can be applied to any dimension of the micromirror. Chapter 1 briefly dealt with the testing of microstructures. In the present work the micromirrors fabricated through MicraGEM SOI process have been tested for static and dynamic behavior. The testing of microsystems is important as it determines the suitability of the microsystems for real applications. In this case, the testing of micromirrors for static angles reinforces the understanding on electrostatic actuation of micromirrors presented throughout this work and also helps to determine the workability of the specific device. The testing of the dynamic behavior of micromachined components is important as it determines the performance characterization of these devices. Due to the smaller dimensions of micromirrors they pose great difficulty in testing with regard to test facilities that are simple and less expensive. One of the methods to test the dynamic characteristics is the testing using Laser Doppler velocimetry as it allows non-contact testing of microsystems thereby allowing to test for frequencies without damaging the sensitive devices. The principle used for this type of testing is the Doppler effect. When the electromagnetic radiation is emitted by a moving object moving toward the observer its frequency increases and when

the object is moving away from the observer, its frequency decreases. This frequency shift is the Doppler effect.

In the present work a Laser Doppler Velocimeter is used to measure the natural frequencies of the micromirror. A laser source is used to measure the static angles of the MicraGEM fabricated micromirror for different predetermined voltages which are within the pull-in or the snap voltage.

5.2 Static testing

As explained in Chapter 2, the micromirrors when actuated by a bias voltage tilt. This property of the micromirror is used in optical switching applications. The static angle and the snap angle concepts used for switching were explained in Chapter 2. In the present section, the micromirrors are tested for static angles for different voltages.

Photograph in Figure 5.1 (a) shows the testing setup used. The 84 PGA packaged MicraGEM device consisting of micromirrors is held by a holder placed on micro-positioners. A He-Ne laser source which has a nominal beam diameter at the output as 1mm is used to get a laser spot on the micromirror device. Figure 5.1 (b) is the close-up view of Figure 5.1 (a) at the indicated region which shows the laser spot on the device. Figure 5.2 shows a microscopic view of laser spot on the micromirror. A diverging-converging lens configuration was used in order to reduce the beam diameter and focus the laser beam onto the structure. Different laser spot sizes may be obtained

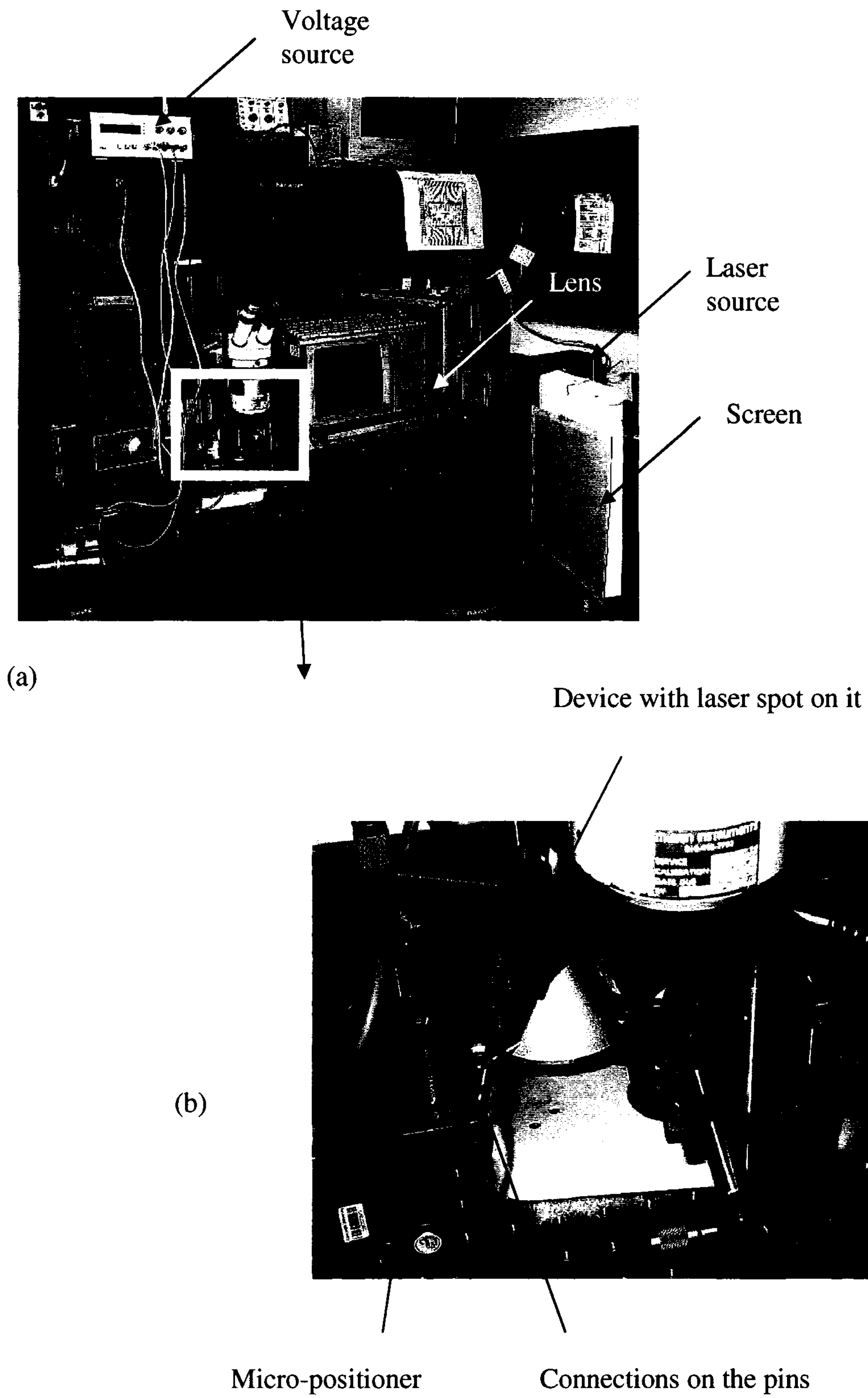

Fig. 5.1 Testing setup to measure the static angle

Fig. 5.2 Microscopic view of the laser spot on a micromirror

by varying the distance between the lenses in order to test devices of different dimensions. The micro-positioners can also be used to fine tune the lens separation. This combination of lens and micro-positioners can be used to get any desired laser spot size. The reflected laser spot falling on the micromirror is made to fall on a white background as shown in the Figure 5.1 (a). The bias voltage is applied through a voltage source through the pins of the packaged device. Figure 5.1 (b) shows the pins connected to the probes which are connected to the voltage source. When a predetermined voltage is applied to the micromirror, the micromirror deflects and the spot falling on the white screen changes its position. By measuring the distance between the spot position at 0 volts and new spot position and also the distance between the device and the screen, the static angle 'θ' of the micromirror for the particular voltage is obtained.

5.2.1 Static angle results and discussion

For the testing of the mirrors, the exact dimensions of the device were taken from the SEM of the MicraGEM SOI microfabricated device. Figure 5.3 shows some of the close-up views of the beam and the micromirror fabricated through the MicraGEM SOI process. The micromirror dimensions on the device are 100μm beam length, 4μm beam width with a plate of dimension 500μm x 500μm. The thickness of the silicon from the SEM pictures shown in Figure 5.4 was found to be 1.9μm. However, the theoretical thickness of silicon specified in the MicraGEM process is 2.075μm which includes the 750 Å of metal coating on top of the silicon. Hence the theoretical prediction was carried out for three thickness values of 1.8μm, 1.9μm and 2.075μm. The actual dielectric gap of 2.2μm determined from SEM measurements has been used for all theoretical predictions. It was found from the theoretical prediction that the pull-in of the device occurs at 1.2 volts. Figure 5.4 gives a comparison of experimentally measured values of static angles and theoretically predicted variation of static angles for three different thicknesses. From the figure it is confirmed that the static angle values are in good agreement with the experimental values.

After 1.2 volts, due to pull-in, the theoretical calculation shows that the mirror snaps reaching the maximum allowed angle. The angle obtained experimentally at 1.2 volts closely matches with that obtained theoretically. The angles obtained after the pull-in voltage has increased steadily due to the fact that the mirror after pull-in enters a bending mode. Due to this, the centre of the mirror at the deflected end gets pulled towards the

electrode, while the edge touches the substrate; hence there is an increase in static angle with increase in voltage. These experimentally calculated angles have been listed along with the theoretically calculated angles in Table 5.1.

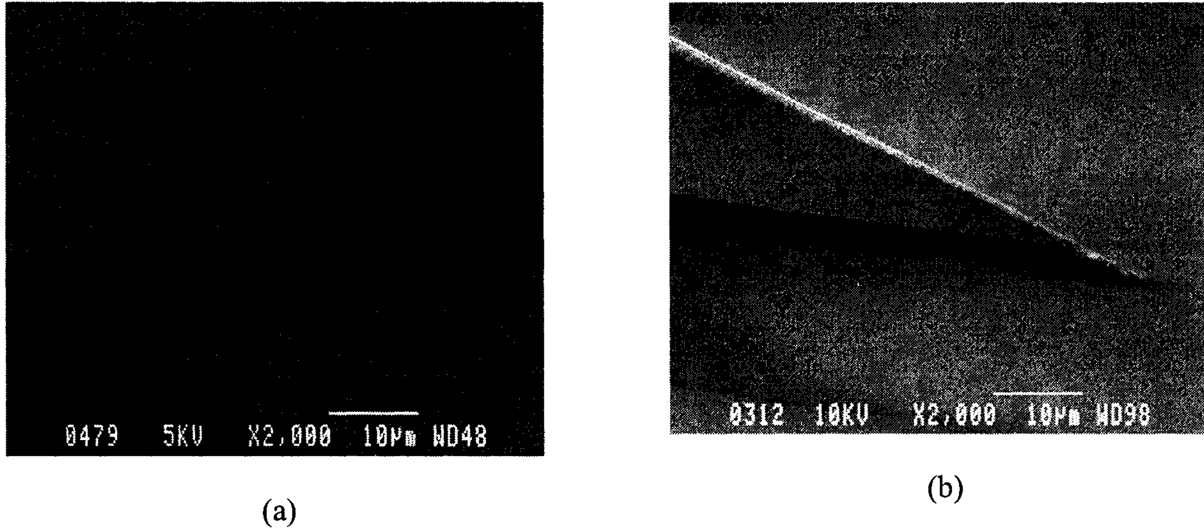

Fig. 5.3 SEM micrograph of close-up of micromirror and the torsion beam

It was observed experimentally that after 2.25 volts, there was no significant change in the position of the laser spot on the screen. Hence the static angle at 3 volts is same as the angle at 2.25volts. The experimental values were tabulated for 5 different readings which were achieved by moving the screen to different positions keeping the device at a constant place, and the average static angles were obtained. The SEM pictures in Figure 5.5 shows the micromirror snapped due to the application of voltages beyond pull-in voltage.

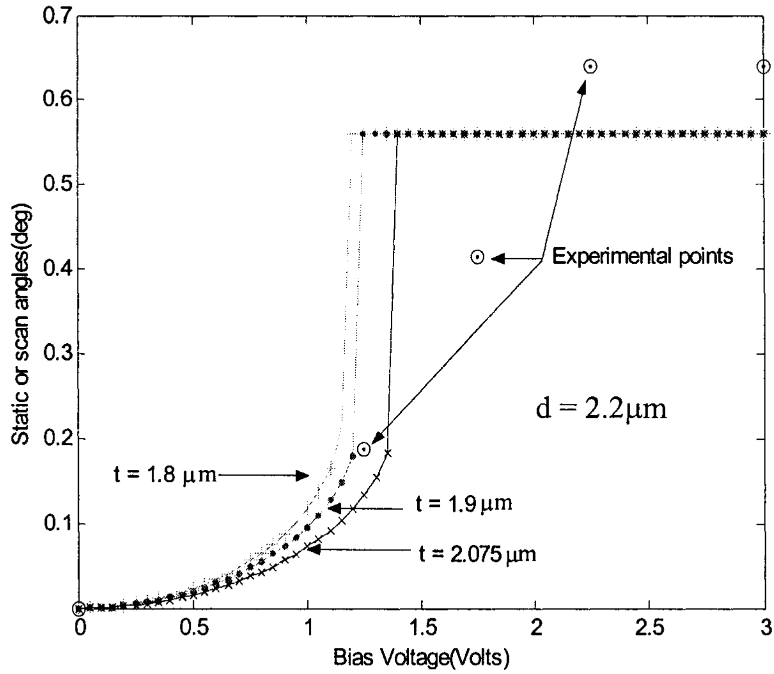

Fig. 5.4 Comparison of experimental and theoretical static angles for different voltages

Bias voltage (volts)	Experimental prediction (in deg)						Theoretical prediction
	Readings						
	1	2	3	4	5	Average	
0	0	0	0	0	0	0	0
1.2	0.1827	0.2122	0.1760	0.18046	0.1876	0.1868	0.17852
1.75	0.36538	0.4244	0.418	0.4511	0.4118	0.414	0.5602
2.25	0.5846	0.63651	0.61598	0.6766	0.6852	0.6397	0.5602
3	0.5846	0.6351	0.61598	0.6766	0.6852	0.6397	0.5602

Table 5.1 Tabulation of experimental and predicted scan angles with t = 1.9μm and d = 2.2μm

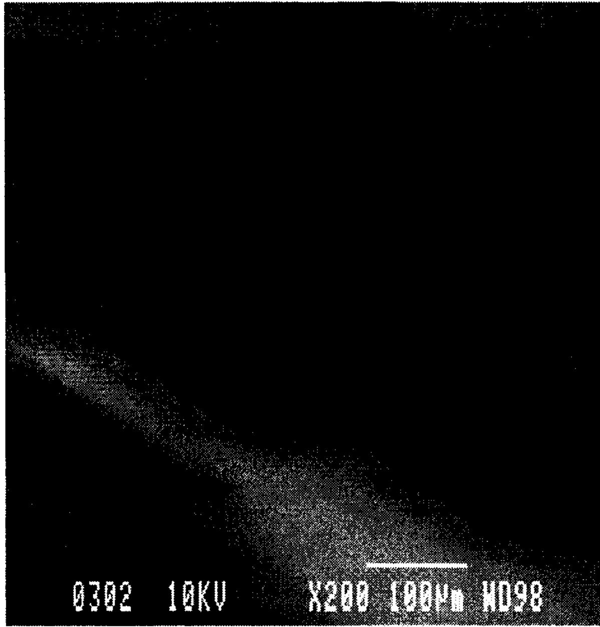

(a)

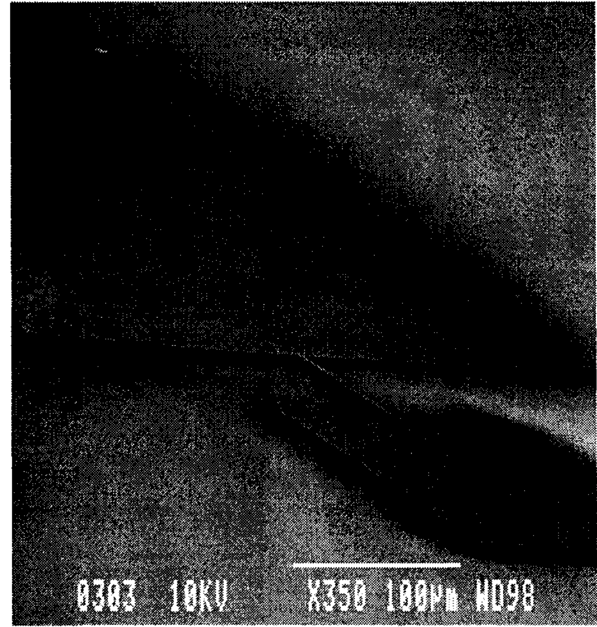

(b)

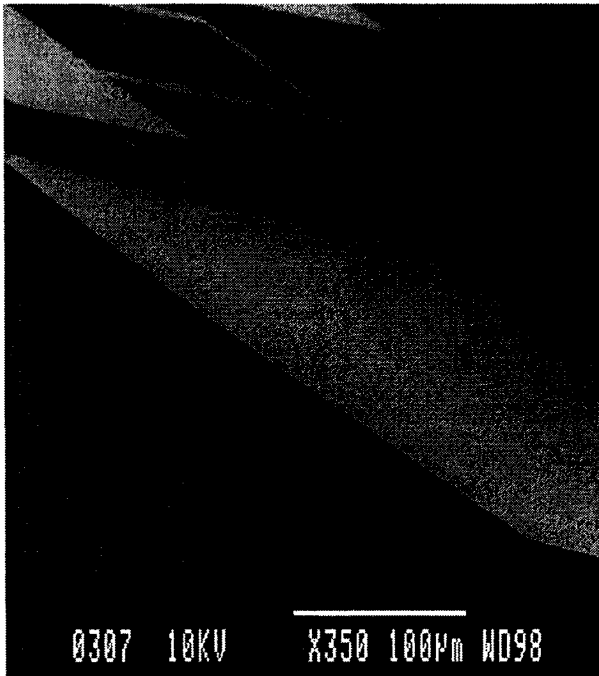

(c)

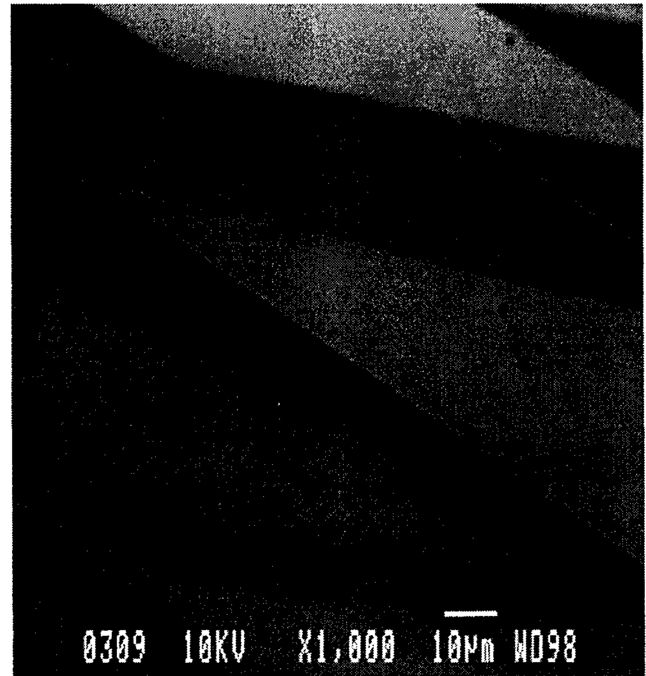

(d)

Fig. 5.5 SEM pictures of snapped micromirror fabricated through MicraGEM SOI process

It can be concluded from the above results that the experimentally obtained values have good agreement with the theoretically obtained values.

5.3 Dynamic testing

As mentioned earlier, for dynamic testing, a Laser Doppler velocimeter (LDV) is used to obtain the natural frequencies of the micromirror. Figure 5.6 shows a schematic of the set-up used [89]. This schematic can be compared to Figure 5.1 (a). The micromirror device is mounted on an oscillating device. The test setup consists of a signal detection system consisting of an oscilloscope for the time-domain reference, and a spectrum analyzer for the frequency domain. When a coherent laser beam is projected on to the surface of the micromirror as shown in Figure 5.6, the light reflected back from the surface undergoes a shift in frequency which will be proportional to the vibrational velocity of the surface due to the Doppler effect. LDV measures this frequency shift and produces a real-time velocity signal, which is characteristic of the surface vibratory motions [89]. All the other components used in the set-up is same as that used to measure the static characteristics of the micromirror.

The test setup consists of Bruel and Kjaer LDV with (HeNe) laser. This laser supply has an integrated Bragg cell. However, to measure the natural frequency, a loose dice of the MicraGEM fabricated device containing the mirrors is attached to a flat acoustic speaker as shown in Figure 5.6. Signal response measurements from the speaker indicated that the Bragg cell had a threshold detection ability of 25khz. Hence the

micromirror is selected in such a way that the theoretical value of natural frequency of the micromirror lies inside the threshold frequency.

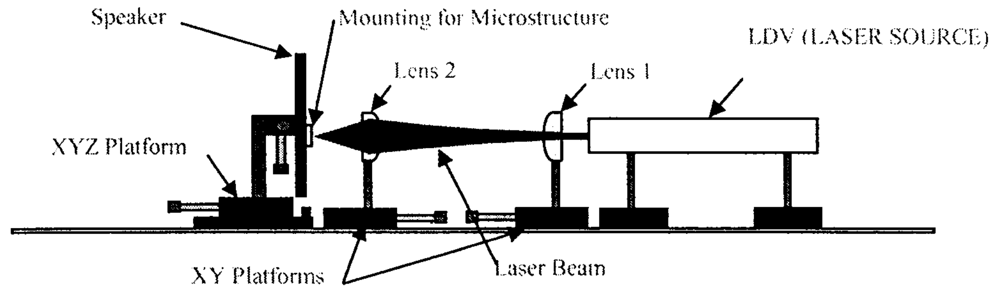

Fig. 5.6 Schematic of the LDV setup for dynamic measurement [89]

5.3.1 Results

Table 5.2 gives the experimentally obtained values of natural frequency for the mirror with dimensions discussed earlier. Figure 5.7 shows the theoretical variation of natural frequency of mirror. The maximum natural frequency of the mirror at 0 volts is found to be 4.09 kHz for a thickness of 2.075μm. The Table 5.2 gives comparision of these values with the experimentally obtained value of natural frequency of the mirror.

	Experimental Values (kHz)	Theoretical Values (kHz)		
		t = 1.8μm	t = 1.9μm	t = 2.075μm
	4.22	3.65	3.81	4.09

Table 5.2 Tabulation of experimental and predicted natural frequencies with gap 2.2μm.

From Figure 5.7 it can also be observed clearly that the pull-in voltage is 1.2 volts. The frequency response of the micromirror has been experimentally obtained and shown in Figure 5.8. This clearly shows the first resonance at 4.22kHz. In order to obtain the final response of the structure, the base response has been subtracted from the response of the entire device. The natural frequency of the micromirror depends on the thickness and as observed theoretically, the frequency increases with increase in thickness as the stiffness increases. Due to microfabrication, it is always observed that the dimensions of the structure may not be same as the theoretical dimensions. Hence the experimental values

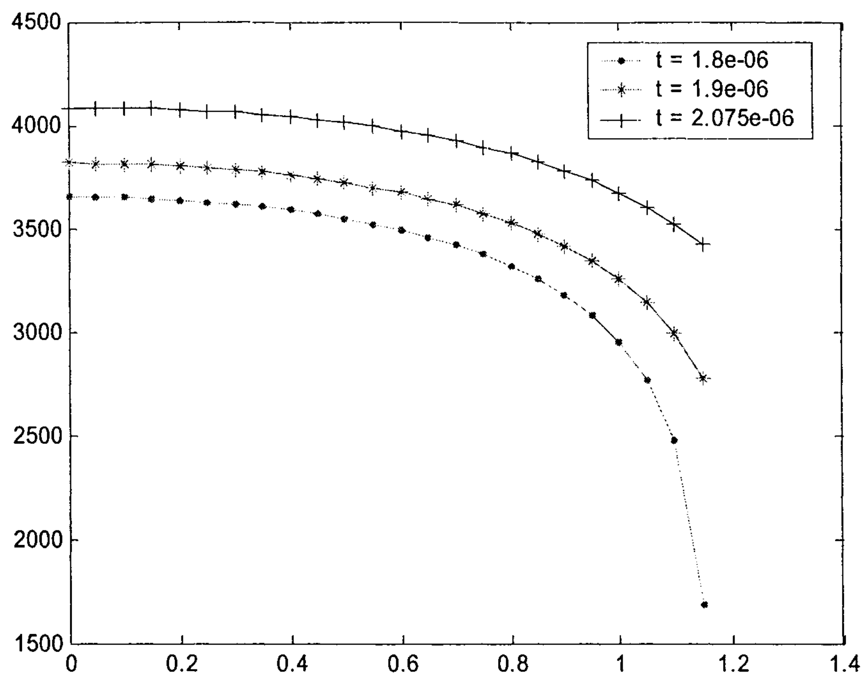

Fig. 5.7 Theoretical variation of natural frequency at different bias voltage

are observed to vary slightly compared to the theoretical values. In this case, the frequency obtained experimentally in Table 5.2 is close to theoretically predicted value.

Thus the testing confirms the validations of the proposed synthesis of electrostatically actuated micromirrors using the concept of boundary conditioning.

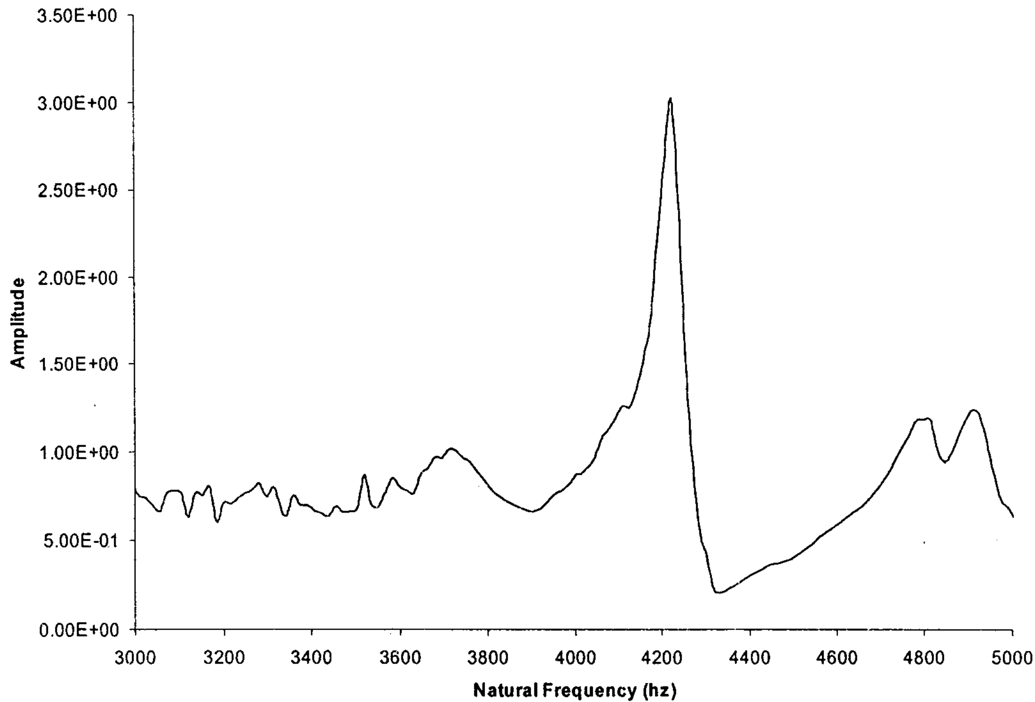

Fig. 5.8 Experimental frequency curve showing resonance at 4.22 kHz

In the present chapter, the static and dynamic testing of the micromirrors fabricated through MicraGEM process have been carried out. The results obtained were validated with the theoretical results and are in good agreement. This determines the performance characterization and usefulness of the micromirrors fabricated through the above mentioned procedure.

Chapter – 6

Conclusions and recommendations for future work

6.1 Conclusions

Electrostatic effects on the dynamics of torsional micromirrors have been modeled and analyzed. The influence of boundary conditioning due to the external effect of electrostatic field has been investigated. The micromirrors were fabricated using the MUMPS surface micromachining process and MicraGEM SOI hybrid micromachining process. Also the fabrication of micromirrors was explored using the double sided pulse etching using XeF_2. A particular MicraGEM fabricated scanning mirror was tested for static angles and natural frequency using a Laser Doppler Velocimeter to validate the theoretical and experimental results.

The 90° torsional micromirror was modeled to include the counter electrostatic field effects in addition to the main electrostatic field. The effect of counter electrostatic field was found to decrease the effective tilting ability of the micromirror as the effect gives rise to a third equilibrium position which was demonstrated in the present work. In order to retain the tilting ability of the mirror, a stopper electrode was introduced whose effect adds onto the main electrostatic field thereby giving the micromirror the desired tilt for optical switching applications.

A conceptual design of one dimensional scanning mirror was carried out considering the design parameters suitable for MUMPS surface micromachining fabrication procedure and SOI bulk micromachining fabrication procedure. The flexibility of using design parameters such as the size of the mirror and the dielectric gap which can be much higher than the maximum dielectric gap allowed in MUMPS was exhibited.

Boundary conditioning of micromirrors using artificial springs was analyzed using boundary characteristic orthogonal polynomials in the Rayleigh-Ritz method. To quantify the end support conditions, translational and rotational springs were used at the supports. The microfabricated end condition was shown to be in between a fully clamped (CCCC) condition and simply supported (SSSS) condition. A comparative study of these support conditions were carried out in order to obtain the eigenvalues and modeshapes for these support conditions. The influence of electrostatic field on the modeshapes has been quantified using modal deviation parameter through artificial elastic foundation. The influence of electrostatic field on the design synthesis has been well modeled.

Microfabrication of different type and dimensions of the mirrors were carried out using MUMPS surface micromachining process and a newly introduced bulk micromachining process called the MicraGEM SOI process. XeF_2 controlled pulse etching method was used for bulk micromachining of SOI wafers with patterns of micromirror. The double side etching on SOI wafer using XeF_2 demonstrated the

feasibility of fabricating SOI based micromirrors that will provide vast design possibilities.

The natural frequency of a particular micromirror fabricated through MicraGEM process and the static angles at different bias voltages were validated with the theoretical result and were found to be in good agreement. An LDV (Laser Doppler Velocimeter) was effectively used to obtain the natural frequency of the mirror actuated by a speaker.

Conclusions based on the results from the present study were outlined at the respective chapters. From a global point of view the conclusions drawn from the present work can be summarized in the following way:

1. The effect of counter electrostatic field reduces the effective tilting angle of the micromirror. A stopper electrode of significant height can nullify this effect. As the stopper height is increased the static angles of the micromirror also increases. The transient response of the micromirror showed that the settling time taken by the mirror to reach the steady state is very small, thereby making it suitable for optical switching applications.
2. The designing of micromirror using SOI bulk micromachining process offers more flexibility over MUMPS with regard to dielectric gap and mirror dimensions. The static angles hence obtained for SOI bulk micromachined fabricated mirrors are more than that of MUMPS fabricated mirrors.

3. Boundary conditioning of external effect of electrostatic field for different end support conditions showed that the elastic properties of the mirror changes with increase in voltage. This is significant in the first mode for the end support conditions discussed, as the peak in the first mode occurs at the centre where the electrostatic field effect is maximum due to the mirror proximity with the fixed electrode.
4. Controlled double side pulse etching using XeF_2 dry isotropic etchant is a good option for bulk micromachining of SOI wafers.
5. A validation of theoretical and experimental results for static angle and natural frequency for different bias voltage were found to be in close agreement.

6.2 Recommendations for future work

MEMS is a multidisciplinary filed with numerous possibilities in various applications. Integration of a MEMS device with electronic circuitry poses a serious challenge to the MEMS industry and universities alike. A systematic approach in research considering the above mentioned aspect is vital.

The present work has focused on the modeling of electrostatic effects on micromirrors and microfabrication. Further work can be carried out on the following.

1. The scope of the present modeling and microfabrication can be extended to other electrostatically actuated MEMS devices such as capacitive and pressure transducers,
2. Finite element modeling of the device with the electrostatic field effects can be carried out using coupled solvers of the FEM package ANSYS.
3. Fringe field effects can be included with the modeling.
4. Boundary conditioning for other external effects like squeeze film damping and Lorentz force can be used to model MEMS devices.
5. Experimental testing of dynamic behavior including the modeshapes under electrostatic field can be studied.

References

[1] K.J. Rebello, "Applications of MEMS in surgery", Proceedings of IEEE, Vol. 92, No. 1, January 2001, pp. 43-55

[2] M. Washizu, O. Kurusawa, S. Suzuki, T. Yamamoto, "Molecular minipulation of DNA using electrostatic effects", Technical Digest of the 14th Sensor Symposium, Tokyo, Japan, 1996, pp. 253-258.

[3] V.A. Aksyuk, F. Pardo, C.A. Bolle, S. Arney, C.R. Giles, D.J. Bishop, "Lucent microstar™ micromirror array technology for large optical crossconnects", MOEMS and Miniaturized Systems, Proceedings of SPIE, Vol. 4178, 2000, pp. 320-324.

[4] R. Wechsung, N. Uenal, J.C. Eloy, H. Wicht, "Market analysis for microsystems 1996-2002", Nexus Task Force Report, Berlin, 2000.

[5] D.E. Ricken, W. Gressner Eds., "Advanced microsystems for automotive applications", Springer-Verlag Heidelberg, New York, 1999.

[6] IBC Ed., "Microtechnologies and miniaturization: Tool, techniques and novel applications for the pharmaceutical industry", UK Conferences Ltd., London, 1997.

[7] P. Turner., "MEMS and Microstructure technology (MST): An applications and market evaluation", 2nd edition, Executive White Paper, Venture Development Corporation, Massachusetts, August 2002.

[8] R.R.A. Syms, "MOEMS tuning element for littrow external cavity laser", Journal of Microelectromechanical Systems, Vol. 12, No. 6, 2003, pp. 921-928.

[9] H. Fujita, "MEMS/MOEMS application to optical communication", Reliability, Testing and Characterization of MEMS/MOEMS, SPIE, Vol. 4588, San Francisco, 2001, pp 11-17.

[10] G.T.A. Kovacs Ed., "Micromachined transducers source handbook", WCB/McGraw Hill, 1998.

[11] M.H. Kiang, O. Solgaard, R.S. Muller, K.Y. Lau, "Surface micromachined electrostatic-comb driven scanning micromirrors for barcode scanners", IEEE MEMS Workshop, San Diego, CA, February 1996, pp. 192-197.

[12] M.H. Kiang, O. Solgaard, R.S. Muller, K.Y. Lau, "Electrostatic combdrive actuated micromirrors for laser-beam scanning and positioning", Journal of microelectromechanical systems, Vol. 7, No.1, 1998, pp. 27-37.

[13] P.M.H. Hagelin, O. Solgaard, "Optical raster-scanning displays based on surface-micromachined polysilicon mirrors", IEEE Sel. Topics Quantam Electronics, Vol. 5, No.1, 1999, pp. 67-74

[14] K.S.J. Pister, M.W. Judy, S.R. Burgett, R.S. Fearing, "Microfabricated hinges", Sensors and Actuators A, Vol. 33, 1992, pp. 249-256.

[15] OE reports 178, "Television discovers digital micromirrors", OE Magazine, SPIE – The International Society for Optical Engineering, October, 1998.

[16] L.J. Hornbeck, "From cathode rays to digital micromirrors: A history of electronic projection display technology", TI Technical Journal, July-September 1998, pp. 7-46.

[17] M.A. Mignardi, "From ICs to DMD^{TM}s", TI Technical Journal, July-September 1998, pp. 56-63.

[18] Z.F. Wang, W. Cao, X.C. Shan, J.F. Xu, S.P. Lim, W. Noell, N.F. De Rooij, "Development of 1 x 4 MEMS based optical switch", Sensors and Actuators A, Vol. 114, 2004, pp. 80-87.

[19] F. Rosenburger, D.L. DeVoe, J. Sirkis, T. Rossmanith, "Micomachined active mirrors for fabry-perot interferometers", Proceedings of Society of Experimental Mechanics: Mechanics and Measurement Symposium, Orlando Fl, 2000, pp. 1-6.

[20] D.S. Greywall, P.A. Busch, F. Pardo, D.W. Carr, G. Bogart, H.T. Soh, "Crystalline silicon tilting mirrors for optical cross-connect switches", Journal of Microelectromechanical Systems, Vol. 12, No. 5, 2003, pp. 708-712.

[21] H. Schenk, P. Durr, D. Kunze, H. Lakner, H. Kuck, "A resonantly excited 2D-micro-scanning-mirror with large deflection", Sensors and Actuators A, Vol. 89, 2001, pp. 104-111.

[22] L.-A. Liew, A. Tuantranont, V.M. Bright, "Modeling of thermal actuation in a bulk-micromachined CMOS micromirror", Microelectronics Journal, Vol. 31, 2000, pp. 791-801.

[23] J. Graffe, M. Suhonen, H. Sipola, T. Sillanpaa, "Scanning microelectromechanical mirror for fine-pointing units of intersatellite optical links", Symposium on Design, Test, Integration and Packaging of MEMS/MOEMS, Proceedings of SPIE, Vol. 4019, 2000, pp. 372-378.

[24] Y.W. Yi, C. Liu, "Magnetic actuation of hinged microstructures", Journal of Microelectromechanical Systems, Vol. 8, No. 1, 1999, pp. 10-17.

[25] J. Zou, J. Chen, C. Liu, J.E. Schutt-Aine, "Plastic deformation magnetic assembly (PDMA) of out-of-plane microstructures: technology and application", Journal of Microelectromechanical Systems, Vol. 10, No. 2, 2001, pp. 302-309.

[26] N.D. Mankame, G.K. Ananthasuresh, "Comprehensive thermal modeling and characterization of an electro-thermal-compliant microactuator", Journal of Micromechanics and Microengineering, Vol. 11, 2001, pp. 1-11.

[27] W. Reithmuller, W. Benecke, "Thermally excited silicon microactuators", IEEE Transactions Electron Devices, Vol. 35, 1988, pp. 758-762.

[28] A.K. Jain, H. Qu, S. Todd, " Electrothermal SCS micromirror with large-vertical-displacement actuations", Solid-State Sensor, Actuator and Microsystems Workshop, Hilton Head Island, South Carolina, June, 2004, pp. 228-231.

[29] J. Hseih, W. Fang, "A novel microelectrostatic torsional actuator", Sensors and Actuators A, Vol. 79, 2000, pp. 64-70.

[30] L. Latorre, J. Kim, J. Lee, P.P. DeGuzman, H.J. Lee, P. Nouet, C.J. Kim, "Electrostatic actuation of microscale liquid-metal droplets", Journal of Microelectromechanical Systems, Vol. 11, No. 4, pp. 302-308.

[31] V. Vleck, "Material science for engineers", Addison-Wesley, New York, 1985.

[32] G.K. Celler, S. Cristoloveanu, "Frontiers of silicon-on-insulator", Journal of Applied Physics, Vol. 93, No. 9, pp. 4955-4978.

[33] K. Izumi, M. Doken, H. Ariyoshi, "CMOS devices fabricated on buried SiO_2 layers formed by oxygen implantation into silicon", Electron Letter, Vol. 14, 1978, pp. 593-597.

[34] J.B. Lasky, "Wafer bonding for silicon-on-insulator technologies", Applied Physics Letter, Vol. 48, 1986, pp. 78-80.

[35] M. Bruel, "Silicon-on-insulator material technology", Electron Letter, Vol. 31, 1995, pp. 1201-1208.

[36] Y.-W. Yi, Y. Kondoh, K. Ihara, M. Saitoh, "A micro active probe device compatible with SOI-CMOS technologies", Journal of Microelectromechanical Systems, Vol. 6, No. 3, 1997, pp. 242-248.

[37] V. Milanovic, "Multilevel beam SOI-MEMS fabrications and applications", Journal of Microelectromechanical Systems, Vol. 13, No. 1, 2004, pp. 19-30.

[38] K.R. Williams, "Etch rates for micromachining processing", Journal of Microelectromechanical Systems, Vol. 5, No. 4, 1996, pp. 256-269.

[39] U. Kohler, A.K. Guber, W. Bier, M. Heckele, "Fabrication of microlenses by plasmaless isotropic etching combined with plastic moulding", Sensors and Actuators A, Vol. 53, 1996, pp. 361-363.

[40] J.S. Park, H.D. Park, S.G. Kang, "Fabrication and properties of PZT micro cantilevers using isotropic silicon dry etching process by XeF_2 gas for release process", Sensors and Actuators A, 2004 (article in press, available online at www.sciencedirect.com).

[41] C. Strandman, L. Rosengren, H.G.A. Elderstig, Y. Backlund, "Fabrication of 45° mirrors together with well defined V-grooves using wet anisotropic etching of silicon", Journal of Microelelectromechanical Systems, Vol. 4, No. 4, 1995, pp. 213-219.

[42] Bell-Northern Research Limited, German Patent no. 2345273, 1972.

[43] D. Cristea, M. Kusko, C. Tibeica, R. Muller, E. Manea, D. Syvridis, "Design and experiments for tunable optical sensor fabrication using <1 1 1> - oriented silicon micromachining", Sensors and Actuators A, Vol. 113, 2004, pp. 312-318.

[44] N.H. Tea, V. Milanovic, C.A. Zincke, J.S. Suehle, M. Gaitan, M.E. Zaghloul, J. Geist, "Hybrid postprocessing etching for CMOS-compatible MEMS", Journal of Microelectromechanical Systems, Vol. 6, No. 4, 1997, pp. 363-372.

[45] L. Li, T. Abe, M. Esashi, "Fabrication of miniaturized bi-convex quartz crystal microbalance using reactive ion etching and melting photoresist", Sensors and Actuators A, 2004 (article in press, available online at www.sciencedirect.com).

[46] C.M. Waits, B. Morgan, M. Kastantin, R. Ghodssi, "Microfabrication of 3D silicon MEMS structures using gray scale lithography and deep reactive ion etching", Sensors and Actuators A, 2004 (article in press, available online at www.sciencedirect.com).

[47] A.A. Ayon, R.L. Bayt, K.S. Breuer, "Deep reactive ion etching: a promising technology for micro-and nanosatellites", Smart Materials and Structures, Vol. 10, 2001, pp. 1135-1144.

[48] W. Ehrfeld, D. Munchmeyer, "Three-dimensional Micro fabrication using synchrotron radiation", Nuclear Instruments and Methods in Physics Research, Vol. A303, 1991, pp. 523-531.

[49] P. Muralt, M. Kohli, T. Maeder, A. Kholkin, K. Brooks, N. Setter, R. Luthier, "Fabrication and characterization of PZT thin film vibrators for micromotors", Sensors and Actuators A, Vol. 48, 1995, pp. 157-165.

[50] S. Sassen, W. Kupke, K. Bauer, "Anodic bonding of evaporated glass structured with lift-off technology for hermetical sealing", Sensors and Actuators A, Vol. 83, 2000, pp. 150-155.

[51] MCNC Center for Microelectronics systems technologies, Research triangle park, NC 27709-2889.

[52] Micralyne Inc, 1911-94 street Edmonton, Alberta, Canada T6N 1E6.

[53] Canadian Microelectronics Corporation, Carruthers Hall, Kingston, Ontario, Canada K7L 3N6.

[54] M. Faucher, "Mitel 1.5μm process review", MITEL Semiconductor, 1994.

[55] N.C. MacDonald, "SCREAM microelectromechanical systems", Microelectronics Engineering, Vol. 32, 1996, pp. 49-73.

[56] J. Jochum, "SCREAM applications: Flow visualization with microfluidic channels", REU project, Cornell Nanofabrication Facility.

[57] More technical information can be obtained at www.mdl.sandia.gov/micromachine.

[58] M.S. Rodgers, J.J. Sniegowski, "5-level polysilicon surface micromachine technology: application to complex mechanical systems", Solid State Sensor and Actuator Workshop, Hilton Head Island, South Carolina, June 1996, pp. 144-149.

[59] P. Muthukumaran, Boundary conditioning concept applied to the synthesis of microsystems using fuzzy logic approach, Doctoral Thesis, Concordia University, Montreal, Canada, March 2000.

[60] P. Muthukumaran, R.B. Bhat, I. Stiharu, "Boundary conditioning technique for structural tuning", Journal of Sound and Vibration, Vol. 220, No. 5, 1999, pp. 547-557.

[61] P. Muthukumaran, R.B. Bhat, I. Stiharu, "Localization of structural vibration and acoustic radiation through boundary conditioning", Transactions CSME, Vol. 22, No. 4B, 1998, pp. 519-532.

[62] P. Muthukumaran, I. Stiharu, R.B. Bhat "Vibration of micromachined condenser microphone plate diaphragms in electrostatic fields", CANCAM 97, 16th Canadian Congress of Applied Mechanics, Quebec, Canada, June 1997, pp. 87-88.

[63] L. Rosengren, J. Soderkviskt, L. Smith, "Micromachined sensor structures with linear capacitive response", Sensors and Actuators A, Vol. 31, 1992, pp. 200-205.

[64] J. Mehner, S. Kurth, D. Billep, C. Kaufmann, K. Kehr, W. Dotzel, "Simulation of gas damping in microstructures with non-trivial geometries", Proceedings 11th Annual Workshop on Microelectromechanical Systems, Heidelberg, Germany, January 1998, pp. 172-177.

[65] Y He, J Marchetti, C Gallegos, F Marseeh, "Accurate fully coupled natural frequency shift of MEMS actuators due to voltage bias and other external forces", IEEE International MEMS'99 Conference, Orlando, FL , January 1999, pp. 17-21.

[66] Y. Ando, T. Ikehara, S. Matsumoto, "Design, fabrication and testing of new comb actuators realizing three dimensional continuous motion", Sensors and Actuators A, Vol. 97-98, 2002, pp. 579-586.

[67] X.Q. Li, L. Qian, "An interactive correlating-filtering approach to remove distortion errors in interferometric optical testing", Sensors and Actuators A, Vol. 112, 2004, pp. 262-266.

[68] S. Kweon, H. Lee, H. Shin, "Modeling and dynamic simulation of electrostatically driven micromirrors", Modeling and Simulation of Microsystems, 2001, pp. 334-337.

[69] D. Lee, U. Krishnamoorthy, K. Yu, O. Solgaard, "Single crystalline silicon micromirrors actuated by self-aligned vertical electrostatic combdrives with piston-motion and rotation capability", Sensors and Actuators (A), 2004 (article in press, available online at www.sciencedirect.)

[70] Z. Hao, B. Wingfield, M. Whitley, J. Brooks, J. A. Hammer, "A design methodology for a bulk-micromachined two-dimensional electrostatic torsion micromirror", Journal of Microelectromechanical Systems, Vol. 12, No. 5, 2003, pp. 692-701.

[71] O. Degani, E. Socher, A. Lipson, D. J. Setter, S. Kaldo, Y. Nemirovsky, "Pull-In study of an electrostatic torsion microactuator", Journal of Microelectromechanical Systems, Vol. 7, No. 4, 1998, pp. 373-379.

[72] H. Toshiyoshi, H. Fujita, "Electrostatic micro torsion mirrors for an optical switch matrix", Journal of Microelectromechanical Systems, Vol. 7, No. 4, 1996, pp.231-237.

[73] S. Kweon, H. Lee, H. Shin, "Modeling and dynamic simulation of electrostatically driven micromirrors", Proceedings of Modeling and Simulation of Microsystems, 2001, pp. 334-337.

[74] D.A. Koester, R. Mahadevan, B. Hardy, K. W. Markus, "MUMPS^{TM} design handbook", Cronos Integrated Microsystems, Rev 6.0.

[75] L.S. Huang, S.S. Lee, E. Motamedi, C.M. Wu, C.J. Kim, "Optical coupling analysis and vibration characterization for packaging of 2x2 MEMS vertical torsion mirror switches", SPIE Conference on Microelectronic Structures and MEMS for Optical Processing, Vol. 3513, 1998, pp. 135-143.

[76] R.B. Bhat, G. Mundkur, " Plate characteristic functions to study sound transmission loss through panels", Second International Congress on Recent Developments in Air and Structure-Borne Sound and Vibration, March 4-6, 1992, pp. 461-468.

[77] P.G. Young, S.M. Dickinson, " On the free flexural vibration of rectangular plates with the straight or curved internal line supports", Journal of Sound and Vibration, Vol. 162, No. 1, 1993, pp. 1643-1647.

[78] A. Achong, "The steel pan as a system of non-linear mode-localized oscillators Part1: theory, simulations, experiments and bifurcation", Journal of Sound and Vibration, Vol. 197, No. 4, pp. 471-487.

[79] P. Rangsten, L. Smith, L. Rosengren, L, B. Hok, "Electrostatically excited diaphragm driven as a loudspeaker", Proceedings of 8th International Conference on Solid-State Sensors and Actuators, Transducers'95, Stockholm, Sweden, June 25-29, 1995, pp. 430-433.

[80] R.B. Bhat, "Natural Frequencies of Rectangular Plates Using Characteristic Orthogonal Polynomials in Rayleigh-Ritz Method", Journal of Sound and Vibration, Vol.102, No. 4, 1985, pp. 493-499

[81] G. Rinaldi, P. Muthukumaran, I. Stiharu, "An improved method for predicting microfabrication influence in atomic force microscopy performances", International Journal of Nanotechnology, Vol. 1, No. 3, 2004, pp. 292-306.

[82] MEMSPro V3.0, Tanner Research Inc, 2650 East Foothill Boulevard, Pasadena, CA 91107.

[83] Report by Canadian Microelectronic Corporation, "Introduction to MicraGEM: A silicon-on-insulator based micromachining process", Report ICI-138 V2.0, December, 2003.

[84] Cadence Design Systems Inc, 2655 Seely Avenue, San Jose, CA 95132.

[85] H.F. Winters, J.W. Coburn, "The etching of silicon with XeF_2 vapor", Appl. Physics Letter, Vol. 34, No. 1, 1979, pp 70-73.

[86] F.I. Chang, "Gas Phase Silicon Micromachining with Xenon Difluoride", Proc. SPIE, Vol. 2641, 1995, pp. 117-128.

[87] S. Renard, "Industrial MEMS on SOI", Journal of Micromechanics and Microengineering, Vol. 10, 2000, pp 245-249.

[88] P. Muthukumaran, I. Stiharu, R.B. Bhat, "Gas phase Xenon difluoride etching of microsystems fabricated through Mitel 1.5 μm CMOS Process", Canadian Journal of Electrical and Computer Engineering, Vol. 25, No. 1, Jan. 2000, pp. 35- 41.

[89] G. Rinaldi, P. Muthukumaran, I. Stiharu, "Experimental investigation on the dynamics of MEMS structures", Proc. of SPIE, Vol. 5455, Strasbourg, France, 2004, pp. 66-73.